Applications of Stability Theory to Ecological Problems

Ayawoa Dagbovie

Submitted for the degree of
Doctor of Philosophy

Heriot-Watt University

Department of Mathematics,
School of Mathematical and Computer Sciences.

October 2013

The copyright in this thesis is owned by the author. Any quotation from the thesis or use of any of the information contained in it must acknowledge this thesis as the source of the quotation or information.

Abstract

The goal of ecology is to investigate the interactions among organisms and their environment. However, ecological systems often exhibit complex dynamics. The application of mathematics to ecological problems has made tremendous progress over the years and many mathematical methods and tools have been developed for the exploration, whether analytical or numerical, of these dynamics. Mathematicians often study ecological systems by modelling them with partial differential equations (PDEs). Calculating the stability of solutions to these PDE systems is a classical question. This thesis first explores the concept of stability in the context of predator-prey invasions. Many ecological systems exhibit multi-year cycles. In such systems, invasions have a complicated spatiotemporal structure. In particular, it is common for unstable steady states to exist as long-term transients behind the invasion front, a phenomenon known as dynamical stabilisation. We combine absolute stability theory and computation to predict how the width of the stabilised region depends on parameter values. We develop our calculations in the context of a model for a cyclic predator-prey system, in which the invasion front and spatiotemporal oscillations of predators and prey are separated by a region in which the coexistence steady state is dynamically stabilised. Vegetation pattern formation in water-limited environments is another topic where stability theory plays a key role; indeed in mathematical models, these patterns are often the results of the dynamics that arise from perturbations to an unstable homogeneous steady state. Vegetation patterns are widespread in semi-deserts and aerial photographs of arid and semi-arid ecosystems have shown several kilometers square of these patterns. On hillsides in particular, vegetation is organised into banded spatial patterns. We first choose a domain in parameter space and calculate the boundary of the region in parameter space where pattern solutions exist. Finally we conclude with investigating how changes in the mean annual rainfall affect the properties of pattern solutions. Our work also highlights the importance of research on the calculation of the absolute spectrum for non-constant solutions.

I would like to dedicate this thesis to my loving mum Antoinette,
my beautiful sister Victoire and my little tiny niece Merveille.
Rest in peace, Dad.

Preface

Understanding the natural world has always been a quest for human beings. Even back in pre-literate societies, people closely observed the behaviour of animals and the properties of plants for survival purposes. Then natural phenomena such as eclipses started to be viewed as attributes of a natural world when they were earlier considered as the work of angry gods.

Today this interest in the dynamics of the physical world has not died. Ecology is a field in natural sciences that has always used mathematical methods in exploring organisms in their environment; as early as in 1798, Malthus (1766-1834) published an essay on population growth. My PhD work fits in the area of mathematical ecology and concerns two ecological phenomena: the invasion of a population of prey by its predator and self-organisation into patterns of vegetation in semi-deserts. More specifically, I am interested in the stability of solutions to the corresponding ecological systems. This thesis is organised into four parts: Part I is an introduction to the thesis and starts with a discussion on the concept of stability of homogeneous steady state solutions to spatiotemporal systems. Parts II deals with absolute and convective instabilities of homogeneous steady states. Parts III and IV concern periodic travelling wave solutions; the first explores their spectral stability while the second investigates their absolute and convective instabilities.

It is my pleasure to express here my gratitude to CANPDE/Maxwell Institute for Mathematical Sciences who made this work possible through their research grant. I am particularly grateful to my supervisor Jonathan Sherratt for his constant support and guidance throughout my PhD journey. Last but not least, I am particularly thankful to Bernd Schroers and Wolfgang Staubach for the wonderful impact they made on the course of my career.

Contents

Part I

Stability of a Homogeneous Steady State and Introduction

Chapter 1

Introduction

Ecological systems often exhibit complex (spatio-)temporal dynamics. Without the use of mathematical tools, the progress of ecological research would be significantly impaired due to the difficulty of studying such complex ecosystems with field data collection as the only tool; in fact, field studies are often costly and time consuming because to obtain genuine data, many experiments are often needed. For example, pattern formation in vegetation happens over years and studying such patterns solely through field observation is simply not practical. The growth of mathematical ecology over the past years has been highly enlightening and has specifically revealed that complex dynamics in an ecological system are not just the product of chance but arise from the system's self-organisation. When these dynamics become unstable, periodic spatial patterns or spatiotemporal chaos are often born. Partial differential equations (PDEs) have been instrumental in modelling ecological systems and mathematical investigation of the spatiotemporal behaviour of these systems often requires the concept of stability of the PDEs' steady states. A very popular example of spatiotemporal patterns that stability theory helps explain are Turing patterns.

1.1 Unstable Equilibrium and Turing Patterns

In temporal systems, if a solution is locally stable any perturbation decays over time. It is well know through the extensive mathematical work of Alan Turing (1912-1954) that a steady state, stable in a temporal system, can become unstable when diffusion terms are added to the system. This 'destabilisation' has been named Turing instability and has been widely studied. For example, Segel & Jackson (1972) introduced a predator-prey

system where Turing instability arises under some conditions. The system is the following:

$$\boxed{\text{prey}} \quad \frac{\partial v}{\partial t} = \epsilon \frac{\partial^2 v}{\partial x^2} + f(v,w) \tag{1a}$$

$$\boxed{\text{predators}} \quad \frac{\partial w}{\partial t} = \frac{\partial^2 w}{\partial x^2} + g(v,w). \tag{1b}$$

Here $v,\ v>0$ and $w,\ w>0$ denote prey and predator densities, which depend on space x and time t, and the functions f and g are defined as $f(v,w) = (1+\kappa v)v - \mu v w$ and $g(v,w) = vw - w^2$.

The model (1) has a coexistence steady state (v^*, w^*) with

$$v^* = w^* = \rho = 1/(\mu - \kappa); \tag{2}$$

we need $\rho > 0$ which implies the condition $\mu > \kappa$. Let $\tilde{v}$ and $\tilde{w}$ denote small perturbations to v^* and w^* respectively. The first step in calculating the stability of $(\bar{v}, \bar{w})$ is to linearise (1) about (v^*, w^*). This yields the following system of linear equations:

$$\frac{\partial \tilde{v}}{\partial t} = \epsilon \frac{\partial^2 \tilde{v}}{\partial x^2} + a_{11}\tilde{v} + a_{12}\tilde{w} \tag{3a}$$

$$\frac{\partial \tilde{w}}{\partial t} = \frac{\partial^2 \tilde{w}}{\partial x^2} + a_{21}\tilde{v} + a_{22}\tilde{w} \tag{3b}$$

where $a_{11} = \left.\frac{\partial f}{\partial v}\right|_{(v^*,w^*)} = \kappa\rho,\ a_{12} = \left.\frac{\partial f}{\partial w}\right|_{(v^*,w^*)} = -\mu\rho,\ a_{21} = \left.\frac{\partial g}{\partial v}\right|_{(v^*,w^*)} = \rho$ and $a_{22} = \left.\frac{\partial g}{\partial w}\right|_{(v^*,w^*)} = -\rho$. The steady state (v^*, w^*) is stable in the temporal system

$$\frac{dv}{dt} = f(v,w) \tag{4a}$$

$$\frac{dw}{dt} = g(v,w) \tag{4b}$$

if and only if all the eigenvalues of the matrix

$$A = \begin{pmatrix} a_{11} & a_{12} \\ a_{21} & a_{22} \end{pmatrix}$$

have negative real parts. This condition is equivalent to:

$$a_{11} + a_{22} < 0 \tag{5a}$$

$$a_{11}a_{22} - a_{12}a_{21} > 0 \tag{5b}$$

implies

$$\kappa < 1 \tag{6a}$$

$$\mu > \kappa. \tag{6b}$$

The parameter values $\kappa = 0.9$ and $\mu = 0.94$, for example, satisfy the conditions in (6). Thus, the steady state $(v^*, w^*) = (25, 25)$ is stable in the temporal system (4); and PDE simulations confirm this (see Figure 1.1a). However, when the same simulations are run in the diffusive system (1) where we choose $\epsilon = 0.5$, we notice that the solution quickly moves away from (v^*, w^*) and we obtain spatiotemporal patterns (Turing patterns): the steady state (v^*, w^*) is unstable in (1). Figure 1.1b is an illustration of this Turing instability.

Obviously the linear stability criterion (an equilibrium is stable if and only if all the eigenvalues of the coefficients matrix of its linearisation have negative real parts) does not apply in spatiotemporal systems. In such systems, stability is characterised by the 'essential spectrum': an equilibrium is stable if and only if all the eigenvalues in its essential spectrum have negative real parts. In the next section, we show that the essential spectrum of the steady state (v^*, w^*) is unstable, thus confirming the simulation results in Figure 1.1b; but first, we start with an introduction to the calculation of essential spectra for reaction-diffusion equations in general.

1.1.1 Calculating Stability in Spatiotemporal Systems: the Essential Spectrum

Consider a reaction-diffusion system

$$U_t = DU_{xx} + f(U) \tag{7}$$

where $U \in \mathbb{R}^N$, f is a smooth function and D is positive diagonal matrix. Let U^* denote a steady state solution of 7. A small perturbation $\bar{U}$ to the steady state U^* satisfies the linearised system

$$\bar{U}_t = D\bar{U}_{xx} + \partial_{\bar{U}} f(U^*)\bar{U}, \tag{8}$$

to leading order. We look for perturbations of the form $\bar{U} = \tilde{U}e^{\lambda t + \nu x}$, where λ, $\nu \in \mathbb{C}$ and $\tilde{U} \in \mathbb{C}^N$. λ is called the temporal eigenvalue and ν, the spatial eigenvalue. Substituting this into 8 and omitting the tildes, we obtain

$$[D\nu^2 + a - \lambda]U = 0, \tag{9}$$

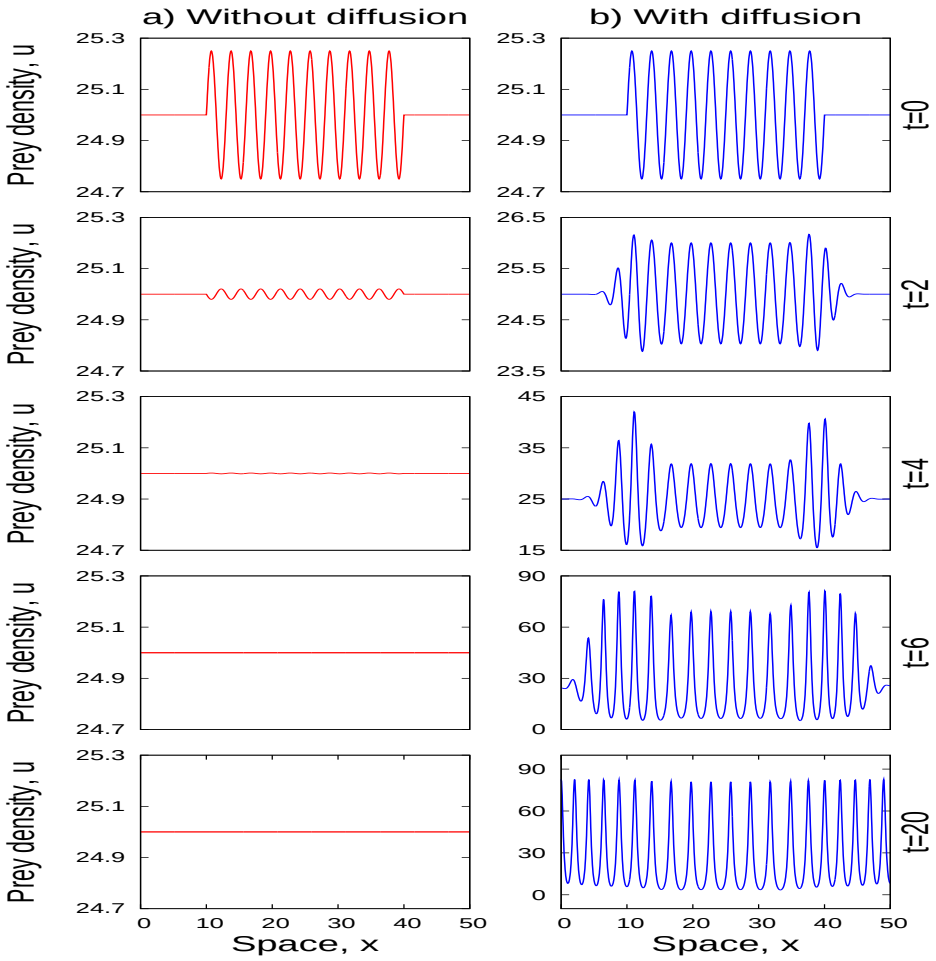

Figure 1.1: Illustrations of the destabilisation of a stable equilibrium through diffusion. We use $\epsilon = 0.5$, $\kappa = 0.9$ and $\mu = 0.94$. The steady state $(v^*, w^*) = (25, 25)$ is stable in the ODEs (4) but appear to be unstable in the PDEs (1). We run the simulations on the domain $x \in (0, 50)$ and initially, the population densities at each grid point on this domain were v^* and w^* slightly perturbed between $10 < x < 40$ by adding 1% of $\rho \sin(\frac{2\pi}{3}(x - 10))$ to both densities. Panel (a) shows simulation results in the nonspatial system while Panel (b) shows dynamics after diffusion has been added; on both panels from top to bottom, are solutions at $t = 0$, $t = 2$, $t = 4$, $t = 6$ and $t = 20$. We used a finite-difference scheme with a space step of 0.05 and a time step of 5×10^{-4} with zero-Neumann boundary conditions.

where a is matrix containing the coefficients $\partial_{\bar{U}} f(U^*)$.

Definition of the Essential Spectrum Let Σ_{ess} denote the essential spectrum. An eigenvalue λ is in Σ_{ess} if and only if λ satisfies (9) for some non-zero U in $\mathbb{C}^N$ and some $\nu \in i\mathbb{R}$, where i is the imaginary unit. In other words, the essential spectrum of U^* is the set of temporal eigenvalues λ satisfying the dispersion relation

$$\begin{aligned} \mathcal{D}(\lambda, \nu) &= \det(\mathrm{D}\nu^2 + \mathrm{a} - \lambda) = 0 \text{ for some } \nu \in \mathrm{i}\mathbb{R} && \text{(10a)} \\ &\Rightarrow \det(-\gamma^2 \mathrm{D} + \mathrm{a} - \lambda) = 0 \text{ for some } \gamma \in \mathbb{R}. && \text{(10b)} \end{aligned}$$

Note that condition (10b) is equivalent to $\det(a - \lambda) = 0$ when $\gamma = 0$ implying that the eigenvalues λ_a of the matrix a are always in the essential spectrum. The latter can then easily be traced by means of numerical continuation. The numerical continuation software we use in this thesis is `AUTO`. To implement the essential spectrum, we simply input Equation (10b) in `AUTO` and set $\gamma = 0$ and the λ_a's as starting points; continuing in γ, $\gamma \in \mathbb{R}$ then traces out the entire spectrum. We now revisit the Segel & Jackson's (1972) model (1) and implement in `AUTO` the essential spectrum of the equilibrium (2) for $\epsilon = 0.5$, $\kappa = 0.9$ and $\mu = 0.94$.

Results of the Implementation of the Essential Spectrum in `AUTO` We have seen previously that, for $\kappa = 0.9$ and $\mu = 0.94$, the steady state (2) is stable in the system (4) but appears unstable in the spatially extended system (1), with the diffusion coefficient $\epsilon = 0.5$. This suggests that the essential spectrum of (2) crosses into the right-half plane, for these parameter values. This was confirmed when we calculated this spectrum as described above (see Figure 1.2). A natural question now is this: given a value of ϵ, what characterises the region(s) in the parameter plane (κ, μ) in which these Turing instabilities arise?

1.1.2 The Extent of Turing Instability in the Segel-Jackson Equation

The calculation of the extent of Turing instability is based on the idea that the steady state (v^*, w^*) first becomes unstable with respect to a spatially heterogeneous perturbation with a certain wavenumber. Recall the linear equations (3) issued from the linearisation of (1) about (v^*, w^*).

- If (1) is considered on a bounded domain $(0, L)$ then any solution $(\tilde{v}, \tilde{w})$ of (3) has

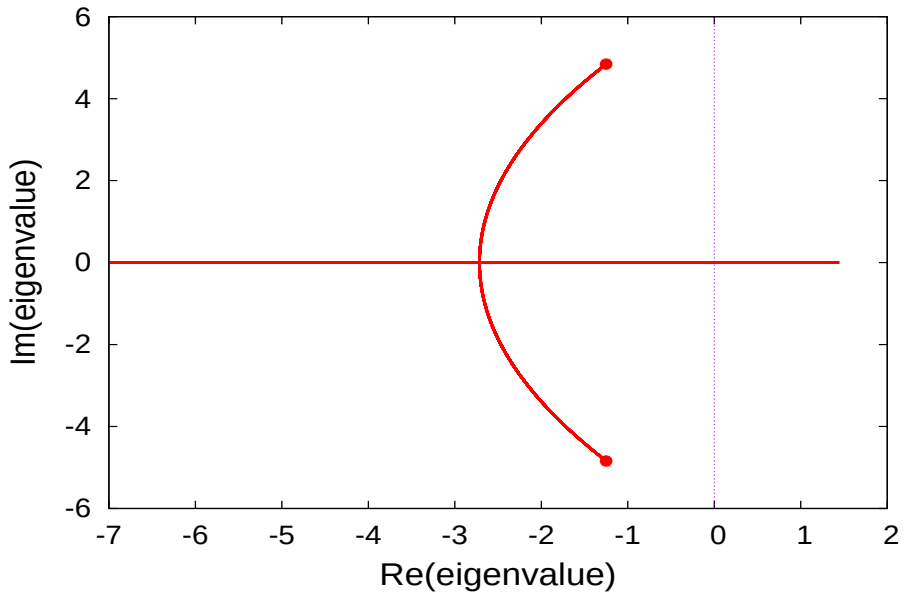

Figure 1.2: Essential spectrum of the steady state (v^*, w^*) in the system (1) for $\epsilon = 0.5$, $\kappa = 0.9$ and $\mu = 0.94$. This spectrum crosses into the right-half plane, therefore (v^*, w^*) is unstable; this explains the birth of the Turing patterns in Figure 1.1b. The filled red circles indicate our starting solutions in `AUTO`; these are the eigenvalues of the matrix (5) and correspond to $\gamma = 0$ in the dispersion relation (10b).

the following Fourier expansion:

$$\tilde{v}(t,x) = \sum_{n=0}^{\infty} v_n(t,x) = \sum_{n=0}^{\infty} \alpha_n(t) \sin k_n x \tag{11a}$$

$$\tilde{w}(t,x) = \sum_{n=0}^{\infty} w_n(t,x) = \sum_{n=0}^{\infty} \beta_n(t) \sin k_n x \tag{11b}$$

where $k_n = \pi n/L$, $n = 0, 1, ..., \infty$ are the corresponding wavenumbers. We substitute (v_n, w_n) into (3) to obtain

$$\frac{d\alpha_n}{dt} = (a_{11} - \epsilon k_n^2)\alpha_n + a_{12}\beta_n \tag{12a}$$

$$\frac{d\beta_n}{dt} = (a_{22} - k_n^2)\beta_n + a_{21}\alpha_n \tag{12b}$$

Solutions of (12) have the form $C_1 \exp(\lambda_1 t) + C_2 \exp(\lambda_2 t)$ with $C_1,\ C_2$ constant. Here λ_1 and λ_2 are the eigenvalues of the matrix

$$B = \begin{pmatrix} a_{11} - \epsilon k_n^2 & a_{12} \\ a_{21} & a_{22} - k_n^2 \end{pmatrix}$$

In other words, λ_1 and λ_2 solve the quadratic equation

$$\lambda^2 - (b_{11} + b_{22})\lambda + (b_{11}b_{22} - a_{21}a_{12}) = 0, \tag{13}$$

where $b_{11} = a_{11} - \epsilon k_n^2$ and $b_{22} = a_{22} - k_n^2$.

• On the other hand, if the system (1) is considered in an unbounded domain $-\infty < x < \infty$ then we expand the perturbations $(\tilde{v}, \tilde{w})$ into the following Fourier integrals:

$$\begin{aligned} \tilde{v}(x,t) &= \frac{1}{2\pi}\int \bar{v}(k,t)e^{ikx}dk, \\ \tilde{w}(x,t) &= \frac{1}{2\pi}\int \bar{w}(k,t)e^{ikx}dk, \end{aligned} \tag{14}$$

where $\bar{v}(k,t)$ and $\bar{w}(k,t)$ are the corresponding Fourier transforms. Substituting (14) into (3) yields the same equation (13).

The condition for stability of the steady state with respect to a perturbation with wavenumber k is then the following:

$$b_{11} + b_{22} < 0 \tag{15a}$$

$$b_{11}b_{22} - a_{12}a_{21} > 0 \tag{15b}$$

Comparing (5) and (15), we conclude that:

• (15a) follows from (5a). Thus, if a change in stability occurs, it stems from (15b) only.

• For a change in stability to be possible, a_{11} and a_{22} have to be of different sign; indeed, if a_{11} and a_{22} are both negative, (15b) follows from (5b).

• $a_{11}a_{22} < 0$ combined with (5b) then implies $a_{12}a_{21} < 0$.

Substituting b_{11} and b_{22} into (15b), we obtain the inequality

$$Q(k^2) = \epsilon k^4 - (\epsilon a_{22} + a_{11})k^2 + (a_{11}a_{22} - a_{12}a_{21}) > 0. \tag{16}$$

If the equilibrium (v^*, w^*) is stable with respect to a perturbation with wavenumber k then (16) holds. Correspondingly, the stable equilibrium becomes unstable with respect to a perturbation with wavenumber k in the diffusive system (1) if $Q(k^2) < 0$. It follows from (5b) that $Q(k^2) < 0$ is satisfied only when

$$\epsilon a_{22} + a_{11} > 0 \tag{17}$$

Assuming that (17) holds, a change in stability will occur if $Q(k^2_{min}) < 0$ where k_{min} is the minimum of Q and is given by

$$k_{min} = \frac{\epsilon a_{22} + a_{11}}{2\epsilon}.$$

Substituting these into the expression of $Q(k^2)$, we obtain the condition:

$$2\sqrt{\epsilon(a_{11}a_{22} - a_{12}a_{21})} - \epsilon a_{22} + a_{11} < 0. \tag{18}$$

In conclusion, the condition for (Turing) pattern formation is defined by (5) and (18). Recalling the values of a_{11}, a_{22}, a_{12} and a_{21}, we obtain that Turing instability occurs in the Segel-Jackson system (1) if

$$\kappa < 1 \tag{19a}$$

$$\mu > \kappa \tag{19b}$$

$$\mu < h_\epsilon(\kappa) = (\epsilon - \kappa)^2/(4\epsilon) + \kappa. \tag{19c}$$

Figure 1.3 shows a plot of the region in the parameter plane (κ, μ) of the system (1) for $\epsilon = 0.5$ where Turing patterns exist. These patterns are not the only interesting spatiotemporal dynamics that arise in reaction-diffusion systems. Others include spatiotemporal chaos, self-organised patchiness, dynamical stabilisation and semi-arid vegetation patterns. This thesis focuses on dynamical stabilisation and semi-arid vegetation patterns which we now introduce.

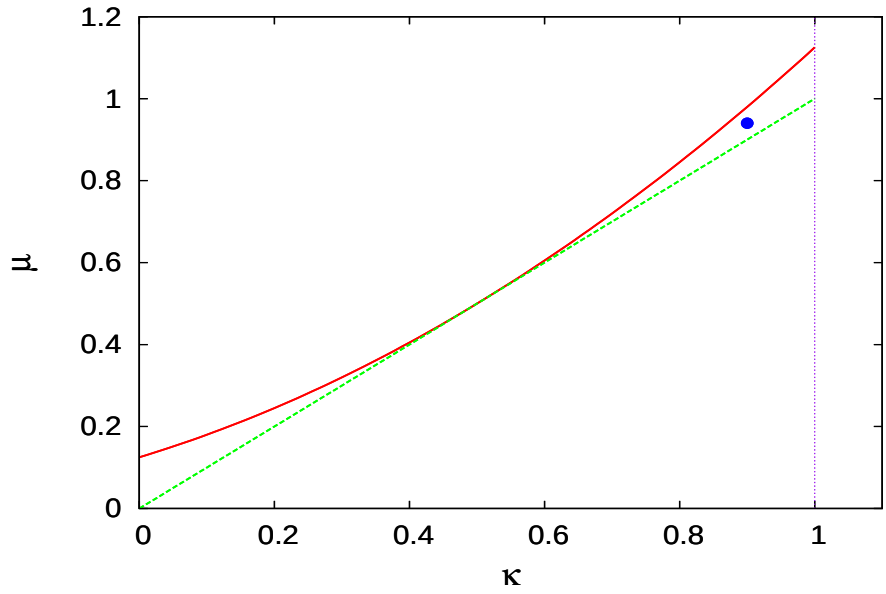

Figure 1.3: Parameter plane (κ, μ) of the system (1) for $\epsilon = 0.5$. The red curve plots the function h_ϵ (19c). Turing instability occurs for parameter values (κ, μ) in the region comprised between this curve and the lines $\mu = \kappa$ (green) and $\kappa = 1$ (purple). The filled blue circle indicates the location of the pair $(\kappa, \mu) = (0.9, 0.94)$ used in previous examples (Figures 1.1 and 1.2).

1.2 Thesis Contents

1.2.1 Dynamical Stabilisation

We have seen in our introductory example in Section 1.1 that a steady state, stable in a temporal system can become unstable in the corresponding reaction-diffusion system. However, diffusion can have an opposite effect. It has been widely reported that the addition of diffusion can have a stabilising effect on an unstable equilibrium. This is known as dynamical stabilisation and has often been observed in mathematical models of the invasion of a population by its predators, or in models of chemical reactions. In particular, in the case of ecological invasions, it is common for an unstable steady state to exist as a long term transient behind the invasion front. Chapters 2 and 3 of this thesis are dedicated to dynamical stabilisation. Our study of the phenomenon will be in the context of a model for a cyclic predator-prey system, in which the invasion front and spatiotemporal oscillations of predators and prey are separated by a region in which the coexistence steady state is dynamically stabilised. An understanding of dynamical

stabilisation requires the theory of convective and absolute stability. In temporal systems, if a solution is locally stable any small perturbation decays over time. However, in a spatiotemporal context one must consider also the propagation of growing perturbations. A solution is "convectively unstable" if all unstable linear modes propagate as they grow. By contrast, "absolutely unstable" solutions have stationary unstable linear modes. To predict how the width of the stabilised region depends on parameter values, we will combine computation and absolute stability theory.

1.2.2 Banded Vegetation Patterns in Arid/Semiarid Ecosystems

Vegetation in semideserts around the world are often organised in remarkably regular patterns. These patterns usually appear as stripes of grass or shrubs or trees alternating with bare ground. However, they cannot be easily detected at ground level and it was not until the invention of aerial photography that this kind of pattern formation was first reported by MacFadyan (1950*a*,*b*); since then vegetation patterns have been studied extensively and it was discovered that they were usual and widespread (Beard 1967, White 1969, 1970, Bernd 1978, Greig-Smith 1979, Lefever & Lejeune 1997). The phenomenon has attracted a lot of interest and has been widely studied. Different hypothesis on the cause of these patterns have been made; with water being limited in semideserts (only 50-750 mm of annual rainfall), one of the hypotheses is that vegetation patterns are triggered by a vegetation-water interaction. In Chapter 4, we will study periodic travelling wave solutions of a well-known vegetation model, the Rietkerk et al. (2002) model. For this model, we will firstly be investigating the existence and the stability of pattern solutions and we focus on the effects that rainfall variations have on banded vegetation patterns. Our main tool in this study is `WAVETRAIN`, a software package for investigating periodic travelling wave solutions of partial differential equations which is freely available for download at `(www.ma.hw.ac.uk/wavetrain)`. We will be making extensive use of the Hopf bifurcation theorem and our search for a periodic travelling wave in `WAVETRAIN` will often begin with locating a Hopf bifurcation point. We now give a brief definition of Hopf bifurcations and their link to limit cycles.

Hopf Bifurcations and Limit Cycles A bifurcation point is a location where the asymptotic structure of a dynamical system changes qualitatively. There is a rich variety of different bifurcations but they can be roughly divided into being either stationary when they involve a change in the number and/or the stability of steady states or periodic when there is a change in the number and/or the stability of periodic solutions.

Consider the following system

$$\frac{\partial v}{\partial t} = F(v, \mu) \tag{20}$$

where v is two dimensional vector and μ is a parameter. Let $\bar{v}$ be a steady state of (20). Linearising (20) about the steady state $\bar{v}$, we obtain two eigenvalues $Re(\lambda) \pm iIm(\lambda)$, where i is the imaginary unit. A Hopf bifurcation occurs when these two eigenvalues cross the imaginary axis due to a change in μ. Let μ_c be the value of μ where the eigenvalues are pure imaginary then there is a Hopf bifurcation at $\mu = \mu_c$. At a Hopf bifurcation, a stationary solution gives birth to a limit cycle; this stationary solution switches stability as the limit cycle is born. The Hopf bifurcation theorem implies that the limit cycle has 0 amplitude at μ_c and this amplitude grows proportionally to $\sqrt{|\mu - \mu_c|}$ as μ moves from μ_c. The period of the limit cycle is $T = \dfrac{2\pi}{Im(\lambda)}$.

Throughout this PhD work, we investigated stability in reaction-diffusion systems using two theories: the theory of (essential) stability and the theory of convective and absolute stability. This thesis is organised as follows: the goal of Chapters 2 and 3 is to provide a better understanding of dynamical stabilisation using the theory of convective and absolute stability. In Chapter 4, we explore semi-arid vegetation patterns and calculate the stability of pattern solutions through numerical continuation of their essential spectra. Chapter 5 is the discussion where we apply the theory of convective and absolute stability to semi-arid vegetation patterns.

Part II

Absolute Instability vs Convective Instability of a Homogeneous Steady State

Chapter 2

A Mathematical Biologist's Guide to Absolute and Convective Instability

This chapter is based on our review paper Sherratt, Dagbovie & Hilker (2013).

2.1 Introduction

Almost all undergraduate courses in mathematical biology include a section on ordinary differential equation (ODE) models. The central player in the course material is the stability of steady states. Students learn that only (locally) stable steady states are biologically significant. Later in their careers, students are introduced to partial differential equation (PDE) models. Again, the stability of (homogeneous) steady states plays a central role. In particular, the first exposure that many students receive to biological pattern formation is the Turing mechanism, in which a steady state that is stable in the kinetic ODEs is destabilised by the addition of diffusion terms. However steady states that are unstable in the kinetic ODEs are almost never mentioned. As a result, there is a widespread assumption that unstable steady states are not biologically significant as PDE solutions. This is not true. In fact, such steady states fall into one of two categories. If they are "absolutely unstable", then they are indeed not biologically significant, except perhaps as providing the mathematical origin of spatial or spatiotemporal patterns. But "convectively unstable" steady states can be an important and persistent feature of PDE solutions. The objective of Sherratt, Dagbovie & Hilker (2013) is to explain the concepts of absolute and convective instability and the related concepts of remnant and transient instability, to illustrate their implications for PDE models of biological systems, and to summarise methods for distinguishing different types of instability in practice.

We begin with an illustrative example: the invasion of a prey population by predators.

This problem has been addressed in many modelling studies. Simple invasions correspond to a standard transition front (e.g. Owen & Lewis 2001), but there is now a considerable body of work on invasions that leave more complex spatiotemporal phenomena in their wake: see for example Sherratt et al. (1995), Petrovskii & Malchow (2000), Morozov et al. (2006), Merchant & Nagata (2010, 2011). We will focus on the spatially extended Rosenzweig & Macarthur (1963) model for predator-prey interaction, and for clarity all of the numerical simulations in this chapter will use this model. We give the equations in a dimensionless form:

$$\boxed{\text{predators}} \quad \frac{\partial p}{\partial t} = \overbrace{d\,\frac{\partial^2 p}{\partial x^2}}^{\text{dispersal}} + \overbrace{c\,\frac{\partial p}{\partial x}}^{\text{advection}} + \overbrace{(\mu/b)hp/(1+\mu h)}^{\text{benefit from predation}} - \overbrace{p/ab}^{\text{death}} \tag{1a}$$

$$\boxed{\text{prey}} \quad \frac{\partial h}{\partial t} = \underbrace{\frac{\partial^2 h}{\partial x^2}}_{\text{dispersal}} + \underbrace{c\,\frac{\partial h}{\partial x}}_{\text{advection}} + \underbrace{h(1-h)}_{\substack{\text{intrinsic}\\ \text{birth \& death}}} - \underbrace{\frac{\mu p h}{1+\mu h}}_{\text{predation}}. \tag{1b}$$

Here p and h denote predator and prey densities, which depend on space x and time t. Here and throughout this chapter we restrict attention to one space dimension: the theory of absolute stability is not yet fully developed in higher dimensions. Most predator-prey studies do not include advection terms, but allowing $c \neq 0$ enables a clearer illustration of some of the concepts we will be discussing. Advection of this type arises naturally in river-based predator-prey systems (Hilker & Lewis 2010). The prey consumption rate per predator is an increasing saturating function of the prey density with Holling type II form: $\mu > 0$ reflects how quickly the consumption rate saturates as prey density increases. Parameters $a > 0$ and $b > 0$ are dimensionless combinations of the birth and death rates; details of the nondimensionalisation are given in Appendix A of Smith et al. (2008), and in many textbooks. The parameter $d > 0$ is the ratio of predator to prey dispersal coefficients. Most terrestrial systems will have d significantly greater than one, while for aquatic and host-parasite systems d is typically close to one. Provided $a > 1 + 1/\mu$, equations (1) have a unique homogeneous coexistence steady state (h_s, p_s) where $h_s = 1/(a\mu - \mu)$ and $p_s = (1-h_s)(1+\mu h_s)/\mu$, which is stable as a solution of the kinetic ODEs only if $\mu < \mu_{crit} = (a+1)/(a-1)$.

Figure 2.1 illustrates simulations of the invasion of a prey population by predators using (1) with no advection, i.e. $c = 0$. For $\mu < \mu_{crit}$, invasion takes the form of a simple transition wave, with the prey-only state $(1, 0)$ ahead of the wave and the stable coexistence state (h_s, p_s) behind it (see Figure 2.1a). But as μ is increased above μ_{crit}, so that the coexistence steady state becomes unstable, this steady state does not suddenly disappear (see Figure 2.1b,c). Rather, for a range of μ values above μ_{crit} there is plateau

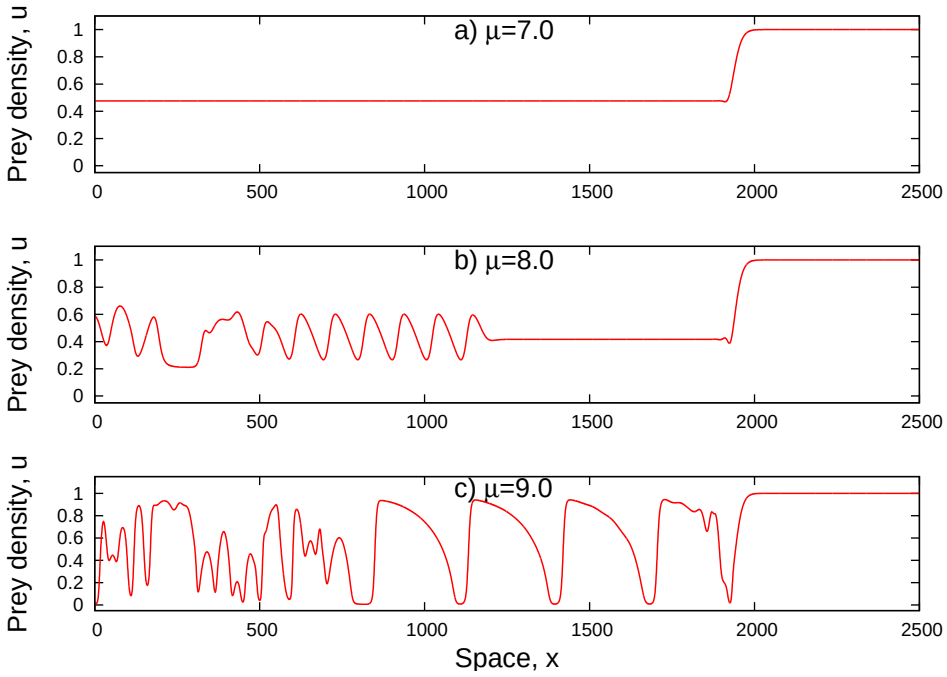

Figure 2.1: Numerical simulation of predators invading prey using the Rosenzweig & Macarthur (1963) model (1) without advection. At time $t = 0$ the system was in the prey-only steady state $(1, 0)$ except for a small predator density near the left hand boundary. The solution is plotted at $t = 4000$. In (a) the parameters are such that the coexistence steady state is stable, and the invasion consists of a simple transition front, connecting the prey-only state and the coexistence state. In (b) the coexistence state persists in a plateau behind the leading front, with spatiotemporal oscillations further back. In (c) there is a periodic travelling wave immediately behind and moving at the same speed as the leading front, with more irregular oscillations further back. Note that for Eq. (1), the existence of both steady state to steady state and steady state to wavetrain transition fronts has been proved by Dunbar (1986) in the limit as $d \to \infty$, with extensions to d finite and sufficiently large by Fraile & Sabina (1989) in the latter case. The parameter values were $a = 1.3$, $b = 4$, $c = 0$, $d = 2$ and (a) $\mu = 7$; (b) $\mu = 8$; (c) $\mu = 9$. The equations were solved numerically using a semi-implicit finite difference method with a grid spacing of 0.5 and a time step of 0.01. We solved on the domain $0 < x < 2500$, with zero flux conditions $p_x = h_x = 0$ at both boundaries.

behind the front in which the solution is at the coexistence state, with spatiotemporal oscillations further back. This plateau is a persistent feature of the invasion profile, despite the fact that the coexistence steady state is unstable. Malchow & Petrovskii (2002) termed this phenomenon "dynamical stabilization", and the key to understanding it is the concept of absolute vs. convective instability. In §2.2 we explain these terms, and in §2.3 we give an example of their use in explaining qualitative transitions in solution behaviour. In §2.4 we summarise the historical development of the theory, and in §2.5 we describe how to distinguish different types of instability using the relatively new approach of the "absolute spectrum". In §2.6 we explain how the theory can be used to make quantitative predictions on how aspects of spatiotemporal behaviour change with model parameters, and in §2.7 we summarise our discussion and consider its application to a wider class of solutions.

2.2 Absolute and Convective Stability

In a temporal system, stability is a relatively simple concept: a solution is (locally) stable if any small perturbation decays. The same is true in a spatiotemporal system: an unstable steady state is defined as one for which some small perturbations grow over time. However the situation is complicated by the fact that spatially localised perturbations may move while they are growing. Consequently it is possible that a perturbation may decay at the location at which it is applied, even though it is growing overall (Figure 2.2a,b). This behaviour defines "convective instability". In contrast, "absolute instability" denotes the situation in which there are perturbations (linear modes) that grow at the location at which they are applied (Figure 2.2c).

In Figure 2.3 we illustrate these two types of instability using simulations of (1). We apply a small perturbation, localised around the centre of the domain, to the coexistence steady state (h_s, p_s). For $\mu < \mu_{crit} = 7.67$ the steady state is stable and the perturbation decays. For $\mu = 9$ the perturbation grows but moves in the positive x direction, decaying at its original location, while for $\mu = 20$ the perturbation grows at its original location. This illustrates the fact that for the values of a, b, c and d used in the figure, the coexistence steady state is convectively unstable for $\mu = 9$ and absolutely unstable for $\mu = 20$.

Practical applications of PDE models in mathematical biology almost always occur on finite domains, and then boundary conditions must be considered when drawing conclusions about stability. If one considers (1) on a domain with periodic boundary conditions, and with a value of μ giving convective instability, a moving growing perturbation will eventually reach the right hand boundary. It will then re-enter at the left hand boundary

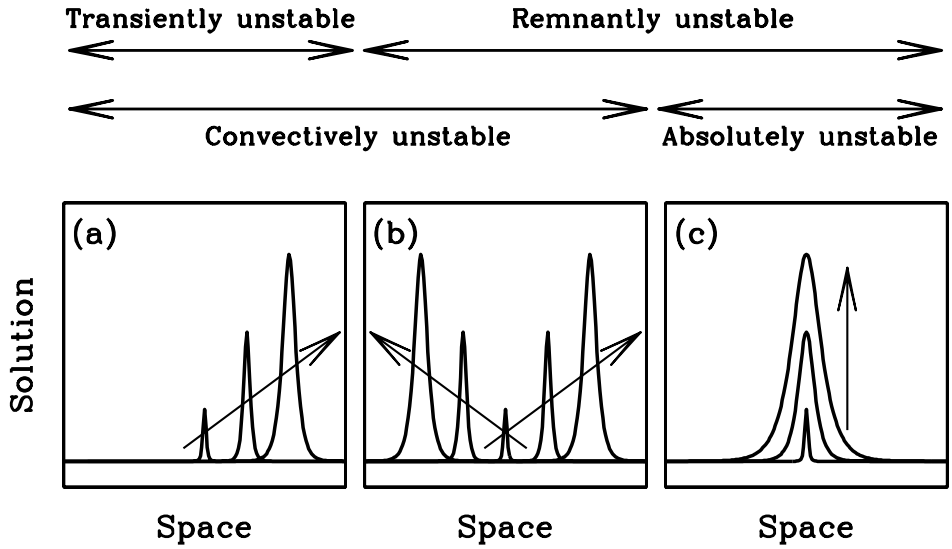

Figure 2.2: A schematic illustration of different types of instability. (a) In transient convective instability, all unstable linear modes move in a single direction while they are growing. (b) In non-transient convective instability, all unstable linear modes move while they are growing, but in both directions. (c) In absolute instability, there is a stationary unstable linear mode, so that there are perturbations that grow at the location at which they are applied. The figure is adapted from Figure 1 of Sandstede & Scheel (2000*a*).

and continue growing (and moving) (Figure 2.4a). Therefore the steady state is unstable in this case. In fact it is a general result that a steady state that is unstable as a solution of the kinetic ODEs is also unstable as a PDE solution on a finite domain with periodic boundary conditions (Sandstede & Scheel 2000*a*). However, for the same parameter values as used in Figure 2.4a but with separated boundary conditions such as Neumann, Dirichlet or Robin, the coexistence steady state of (1) is stable. This is because the growing perturbation moves in the positive x direction until it reaches the right hand boundary, where it is absorbed (Figure 2.4b). Note that in the context of a river-based system ($c \neq 0$ in (1)), a Dirichlet boundary condition corresponds to a hostile boundary such as a waterfall or a region containing toxic waste water, while a zero-flux condition is of Robin type. A zero Neumann boundary condition is known as a Danckwert boundary condition and corresponds to a long river in which the downstream boundary has little influence (Lutscher et al. 2006, Nauman 2008 §9.3.1, Hilker & Lewis 2010).

For most equation systems, a convectively unstable steady state is stable on a finite domain with separated boundary conditions, as is the case for (1). However this will not be the case if there are growing perturbations that travel to the left and right simultane-

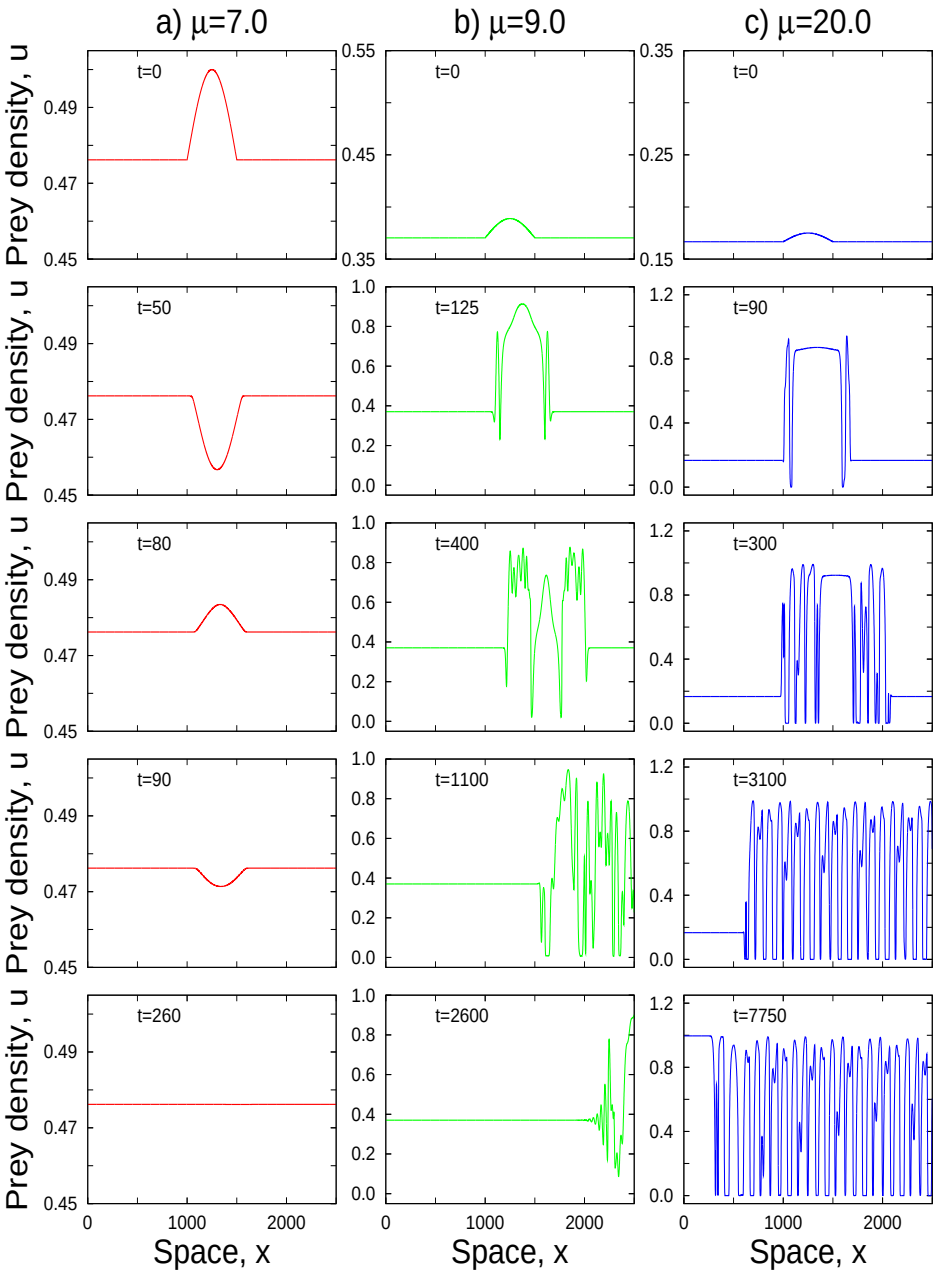

Figure 2.3: Numerical simulations of the Rosenzweig-MacArthur model (1) following a small perturbation to the coexistence steady state. (a) For $\mu = 7$ the steady state is stable and the perturbation decays. (b,c) For $\mu = 9$ and $\mu = 20$ the steady state is unstable. In the former case the perturbation grows but simultaneously moves across the domain, while in the latter case it grows at the point at which it was initially applied. The other parameters were $a = 1.3$, $b = 4$, $c = -1$, $d = 2$. The initial condition in each case was $(h, p) = (h_s, p_s) \cdot [1 + 0.05 \sin(\pi x/1000)]$ if $1000 < x < 1500$ and $(h, p) = (h_s, p_s)$ otherwise. The equations were solved numerically as in Figure 2.1, on $0 < x < 2500$ with Danckwert's (zero Neumann) boundary conditions at both ends.

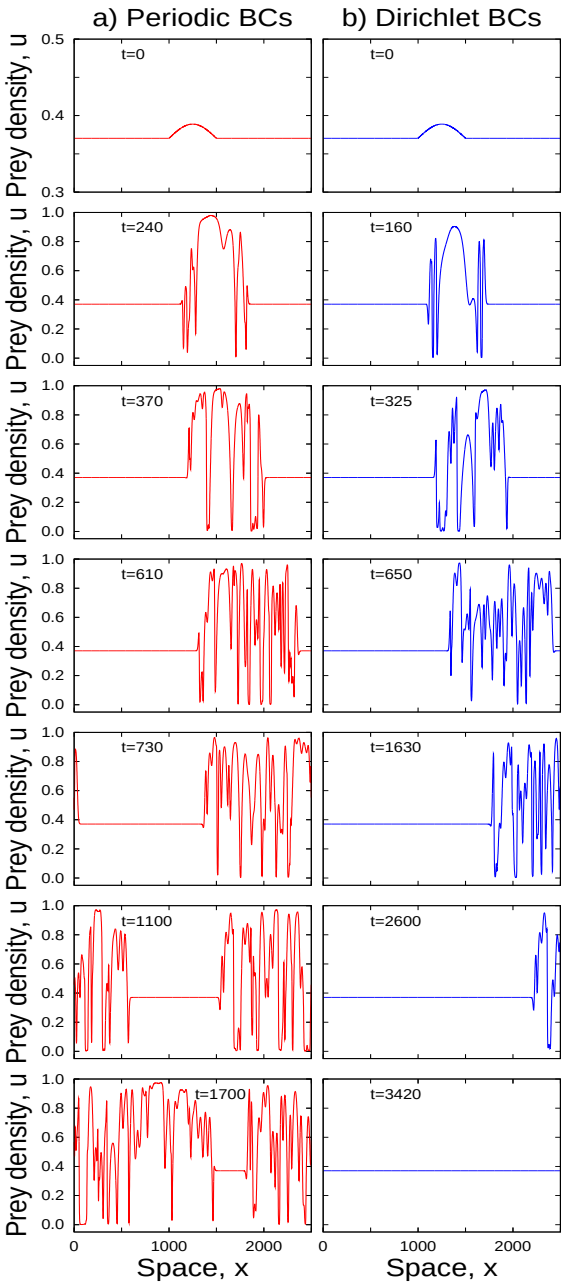

Figure 2.4: Numerical simulations of the Rosenzweig-MacArthur model (1) following a small perturbation to the coexistence steady state for $a = 1.3$, $b = 4$, $c = -1$, $d = 2$, $\mu = 9$ with (a) periodic boundary conditions; (b) Dirichlet conditions $(h, p) = (h_s, p_s)$ at both boundaries. In both cases the perturbation grows but travels in the positive x direction. In (a), when the growing perturbation reaches the right hand boundary it re-enters the domain at the left hand boundary and continues to move, reaching the original site of perturbation with a greater amplitude than it had initially. The repetition of this process results in the steady state being unstable. However in (b), when the growing perturbation reaches the right hand boundary it is absorbed, so that the steady state is stable. The initial conditions and the values of the other parameters were as in Figure 2.3, and the numerical method was as in Figure 2.1.

ously, while decaying at their original location: this is known as "non-transient convective instability" (Sandstede & Scheel 2000*a*; Figure 2.2). Then on a finite domain the growing perturbations will typically be reflected by the boundaries rather than being absorbed, so that the steady state is unstable. The distinction between transient and non-transient convective instabilities was first recognised by Proctor and coworkers (Worledge et al. 1997, Tobias et al. 1998, Fox & Proctor 1998), and Sandstede & Scheel (2000*a*) argue that it is more instructive to distinguish between transient and remnant instabilities than between convective and absolute instabilities. Here the term "remnant instability" means an instability that is either absolute or non-transient convective. One therefore has the following result:

> on a large finite domain with separated boundary conditions, transiently unstable steady states are stable, while remnantly unstable steady states are unstable

(see Sandstede & Scheel (2000*a*) for a more precise statement). Examples of non-transient convective instabilities are given in Sandstede & Scheel (2000*a*, example 2 in §3.3) and Rademacher et al. (2007, §5.2). However, we are not aware of an example from a biological application. This means that the distinctions between absolute and convective instabilities is the same as that between transient and remnant instabilities in all mathematical biology models in which these issues have been investigated.

2.3 An Illustrative Example

We now present an illustration of different qualitative solution forms resulting from a steady state being convectively or absolutely unstable. We consider (1) on a finite domain with the zero flux condition $h_x + ch = dp_x + cp = 0$ at the left hand boundary and the Danckwert condition $h_x = p_x = 0$ at the right hand boundary. An example situation in which such end conditions would be relevant is a long section of river in which the left hand boundary corresponds to the river's source (Lutscher et al. 2006). Initially we set the populations to their coexistence steady state levels in the interior of the domain. This steady state is incompatible with the zero flux boundary condition, and the predators are gradually washed out of system (Figure 2.5; Hilker & Lewis 2010). This occurs via a transition front moving across the domain, so that the prey-only steady state appears to "invade" the coexistence steady state. In Figure 2.5a the coexistence steady state is stable, and the transition front is of a simple type. However in Figure 2.5b the steady state is (transiently) convectively unstable. The tail of the transition front applies perturbations to the coexistence steady state ahead of it, and these perturbations all travel in the

positive x direction as they grow. Therefore the solution remains at (or very close to) the steady state immediately ahead of the front, with spatiotemporal oscillations developing further to the right, where the perturbations have grown sufficiently large to have a significant effect. In Figure 2.5c the steady state is absolutely unstable. Then there are both stationary and moving linear modes in the perturbation applied to the coexistence steady state by the transition front. Therefore spatiotemporal oscillations develop everywhere ahead of the front (Figure 2.5c).

This simple example illustrates the way in which convective and absolute instability lead to qualitatively different solutions. Within the convectively unstable parameter regime the width of the region in which the populations are at the coexistence steady state is a decreasing function of μ. Intuitively, as μ increases the perturbations imposed on the steady state by the invasion front travel away from the front more slowly, and grow more quickly. In §2.6 we will show how a detailed study of the movement and growth of small perturbations can be used to calculate the dependence on μ of the width of the steady state region.

2.4 A Brief History of Absolute Stability

The concept of absolute stability was initially developed in the context of plasma physics, with the first detailed presentation being the monograph by Briggs (1964). In the subsequent decades the ideas have come into common usage in fluid dynamics (reviewed by Huerre & Monkewitz (1990) and Chomaz (2005)) and spiral wave break-up (e.g. Aranson et al. 1992, Sandstede & Scheel 2000*b*, Wheeler & Barkley 2006). However they remain almost entirely absent from the literature on applications of mathematics to chemistry, ecology, biology and medicine.

A fundamental issue is how one calculates whether an unstable steady state is convectively or absolutely unstable. The original approach of Briggs (1964) was to solve the linear equations governing small perturbations by Fourier and Laplace transforms, and to consider the large time asymptotics of the inverse transforms. Eigenvalues satisfying a criterion known as the "pinching condition" play a special role in this asymptotic behaviour, because they prevent appropriate deformation of the Fourier integration contour. Briggs (1964) showed that the condition for convective instability was that all eigenvalues satisfying the pinching condition have negative real part. Briggs' (1964) work assumed that the integrand in the inverse Fourier transform has only first order poles; his results were extended to include higher order poles by Brevdo (1988), and to spatially and temporally periodic solutions by Brevdo & Bridges (1996, 1997).

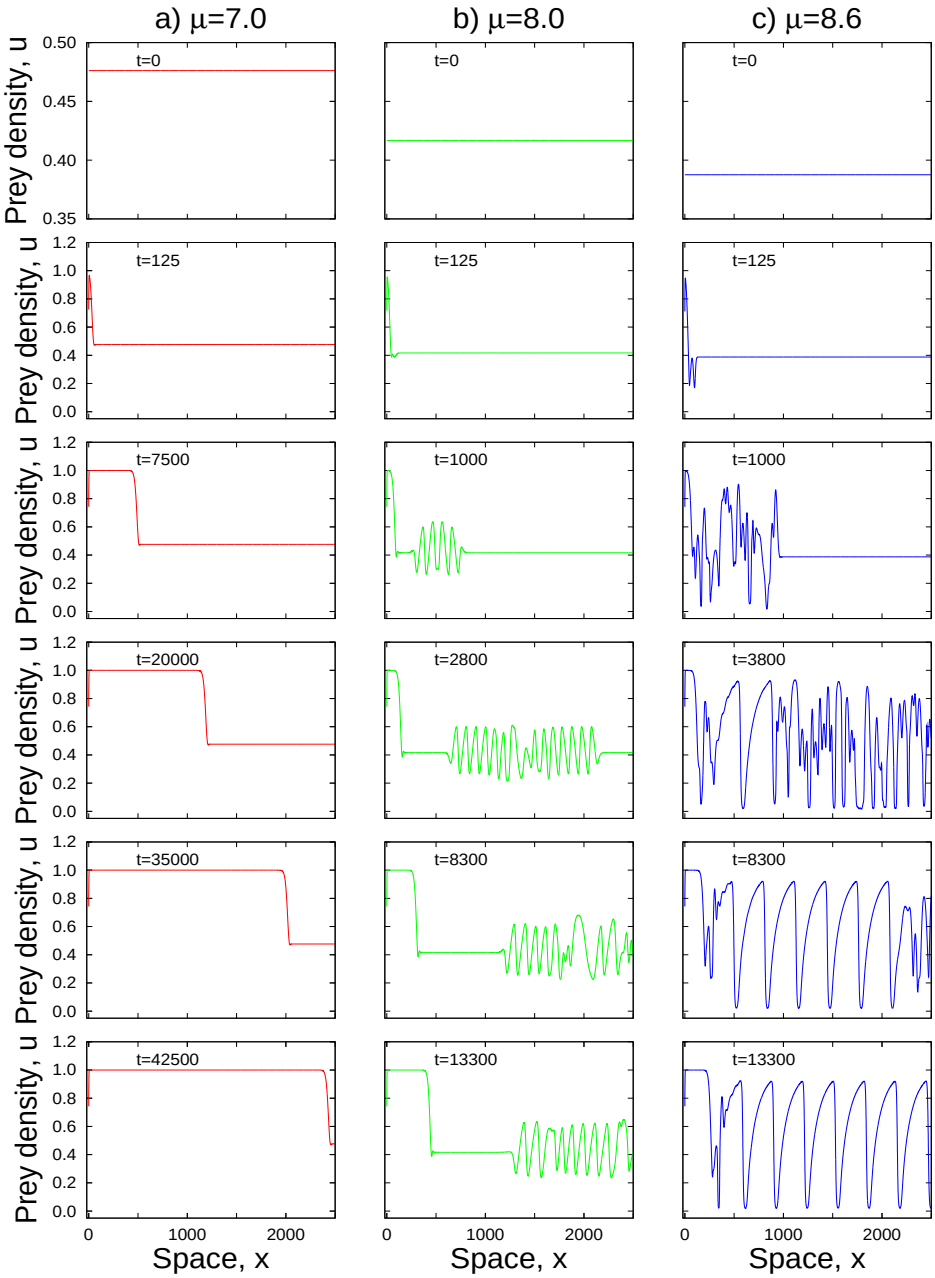

Figure 2.5: Numerical simulations of the Rosenzweig & Macarthur (1963) model (1) with the zero flux condition $h_x + ch = dp_x + cp = 0$ at the left hand boundary and the Danckwert condition $h_x = p_x = 0$ at the right hand boundary. Initially the solution is at the coexistence steady state, but this is incompatible with the left hand boundary condition, and a transition front develops that replaces the coexistence steady state with the prey-only state. The coexistence steady state is stable in (a) and unstable in (b,c). Therefore the transition front is of a simple type in (a) while in (b,c) spatiotemporal oscillations develop, either some distance downstream (b) or immediately ahead of the front (c). The parameter values were $a = 1.3$, $b = 4$, $c = -0.5$, $d = 2$ and (a) $\mu = 7$, (b) $\mu = 8$, (c) $\mu = 8.6$. The numerical method was as in Figure 2.1.

Numerical implementation of the Briggs-Brevdo-Bridges criterion is relatively difficult. Brevdo and coworkers (Brevdo 1995, Brevdo et al. 1999) developed a procedure based on numerical continuation of the location of a saddle point of a particular function of the eigenvalues; this saddle point gives the leading order contribution to the long-time asymptotics of the inverse Fourier transform. More recently Suslov ((2001, 2006, 2009); Suslov & Paolucci 2004) extended this approach to give an automatic search algorithm for calculating the convective–absolute stability boundary in parameter space. Brevdo's method is complicated, and Suslov's (highly ingenious) method is extremely complicated; neither is really suitable for non-specialists.

Fortunately, a new approach to the determination of convective/absolute instability has been developed by Sandstede & Scheel (2000*a*). Building on the work of Beyn & Lorenz (1999) on exponential dichotomies, Sandstede & Scheel (2000*a*) introduced the notion of the "absolute spectrum". This term is a slight misnomer, since the absolute spectrum is not the set of eigenvalues of any linear operator. However it serves a similar purpose in practice: it is a set of eigenvalues, and different types of instability can be distinguished by whether the absolute spectrum does / does not cross into the right hand half of the complex plane. In practice the absolute spectrum provides a relatively straightforward means of calculating absolute stability, even for the non-specialist.

2.5 The Absolute Spectrum

The first step in considering stability of a homogeneous steady state is to linearise the governing PDEs about the steady state. In the standard way, one then looks for solutions of these linear equations that are proportional to $e^{\lambda t+ikx}$; for non-trivial solutions, this leads to a dispersion relation $\mathcal{D}(\lambda,k)=0$ to be satisfied by λ and k. We denote by N the order of $\mathcal{D}$ as a polynomial in k; thus for (1), $N=4$. To calculate stability of the steady state, one considers values of λ satisfying $\mathcal{D}(\lambda,k)=0$ with $k\in\mathbb{R}$; the steady state is stable if and only if all such λ's (except possibly $\lambda=0$) have $\mathrm{Re}\lambda<0$. This procedure is familiar from calculations of the conditions for Turing patterns seen in Chapter 1.

When considering absolute stability, it is necessary to allow both k and λ to be complex-valued. For any given λ, we denote the roots for k of the dispersion relation by $k_1(\lambda)$, $k_2(\lambda)$, …, $k_N(\lambda)$, repeated with multiplicity, and labelled so that

$$\mathrm{Im}(k_1)\le\mathrm{Im}(k_2)\le\ldots\le\mathrm{Im}(k_N).$$

For absolute stability, one must consider a particular root k_{n^*}. A formal definition of

n^* is given in Sandstede & Scheel (2000*a*, §2.1), but it is most easily understood in the following intuitive way: for the PDE to be well-defined on a finite domain with separated boundary conditions, n^* boundary conditions are required at the right hand boundary, with $N - n^*$ conditions at the left hand boundary. Thus for (1), $n^* = 2$ (and $N = 4$). As a different example, consider the model of Klausmeier (1999) for vegetation patterning on gentle slopes in semi-arid environments. This model involves equations for the plant biomass $m(x,t)$ and the water density $w(x,t)$, with the spatial coordinate x increasing in the uphill direction:

$$\partial m/\partial t = \overbrace{wm^2}^{\text{plant growth}} - \overbrace{Bm}^{\text{plant loss}} + \overbrace{\partial^2 m/\partial x^2}^{\text{plant dispersal}} \tag{2a}$$

$$\partial w/\partial t = \underbrace{A}_{\text{rain-fall}} - \underbrace{w}_{\text{evapo-ration}} - \underbrace{wm^2}_{\text{uptake by plants}} + \underbrace{\nu\,\partial w/\partial x}_{\text{flow downhill}}. \tag{2b}$$

Here the parameters A, B and ν are all positive. For these equations, conditions on m would be required at both boundaries, but a condition on w is required only at the right hand (upslope) boundary: therefore $n^* = 2$ (and $N = 3$).

The "absolute spectrum" is the set of values of λ such that $\operatorname{Im} k_{n^*} = \operatorname{Im} k_{n^*+1}$. It is also useful to have a name for the more general set of λ's for which $\operatorname{Im} k_i = \operatorname{Im} k_{i+1}$ for any i, and this is known as the "generalised absolute spectrum". This latter set of eigenvalues was considered (without the name) in the original monograph of Briggs (1964), but the special significance of the case $i = n^*$ was not realised until Sandstede & Scheel's (2000*a*) work. Two final pieces of terminology are also useful: values of λ for which $k_n = k_{n+1}$ are known as "branch points of index n", and "branch points in the absolute spectrum" are simply those with index n^*. Figures 2.6-2.8 show absolute spectra and the generalised absolute spectra for $b = 4$ and $b = 1.2$ with various c values. The parameter values used in Figure 2.7c are the same as in Figure 2.3b.

For a spatially homogeneous steady state that is unstable as a solution of the kinetic ODEs, Sandstede & Scheel (2000*a*) showed that the absolute spectrum determines the nature of its instability in the PDEs as follows:

- the steady state is absolutely / convectively unstable according to whether there are/are not branch points of the absolute spectrum in the right hand half of the complex plane;

- the steady state is remnantly / transiently unstable according to whether the abso-

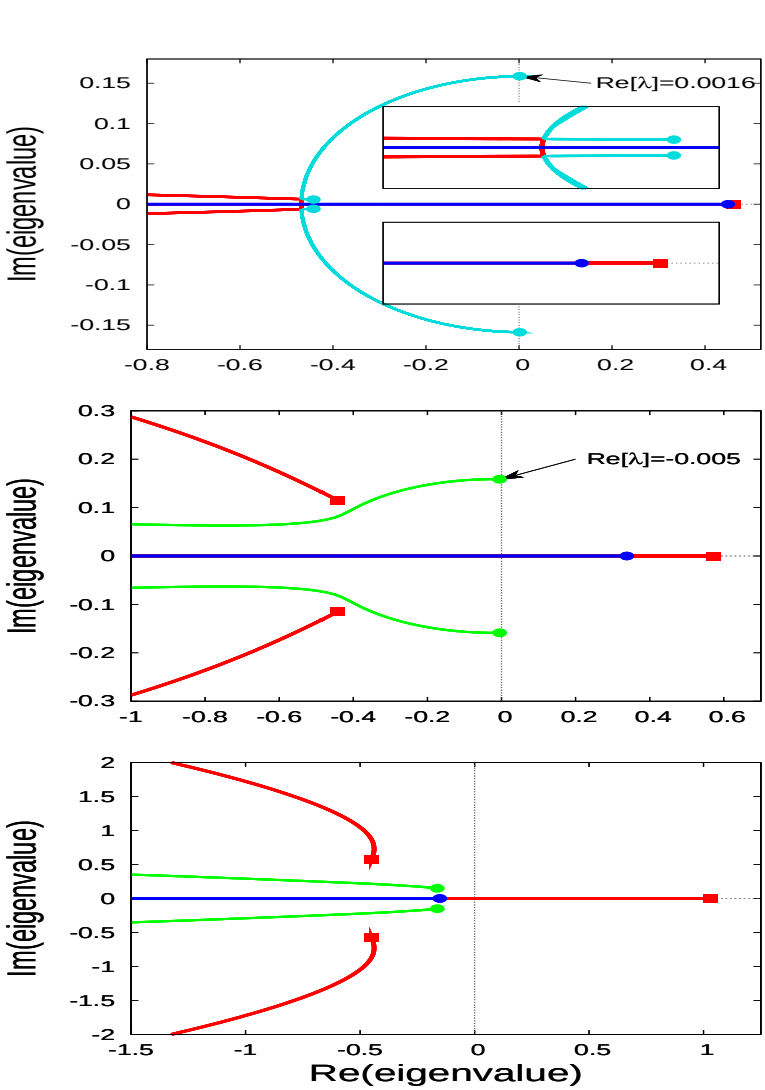

Figure 2.6: Illustrations of the absolute spectrum and generalised absolute spectrum for the Rosenzweig-MacArthur model (1). Branch points are indicated by filled circles and filled squares. The values of μ, a, b and d are fixed as follows: $\mu = 7.7$, $a = 1.3$, $b = 4$ and $d = 2$. The numerical method was as described in the text: we first calculated the branch points (see Appendix A.1), then use these as starting points for the calculation of the generalised absolute spectrum, monitoring all of the k_i's during the continuation in order to determine which sections constitute the absolute spectrum. In green, we plot stable absolute spectra while unstable absolute spectra are represented by cyan curves. The red curves correspond to $\operatorname{Im} k_1 = \operatorname{Im} k_2$, while on the blue curves $\operatorname{Im} k_3 = \operatorname{Im} k_4$. On Panel (a), the advection constant is $c = 0.01$ and the absolute spectra is unstable. The inserts show details of behaviour near branch points; $-0.5 < \operatorname{Re}\lambda < -0.433$ and $-0.03 < \operatorname{Im}\lambda < 0.03$ for the top insert while $0.42 < \operatorname{Re}\lambda < 0.47$ and $-0.01 < \operatorname{Im}\lambda < 0.01$ for the bottom insert. Panels (b) and (c) both show stable absolute spectra and correspond respectively to $c = 0.2$ and $c = 1$.

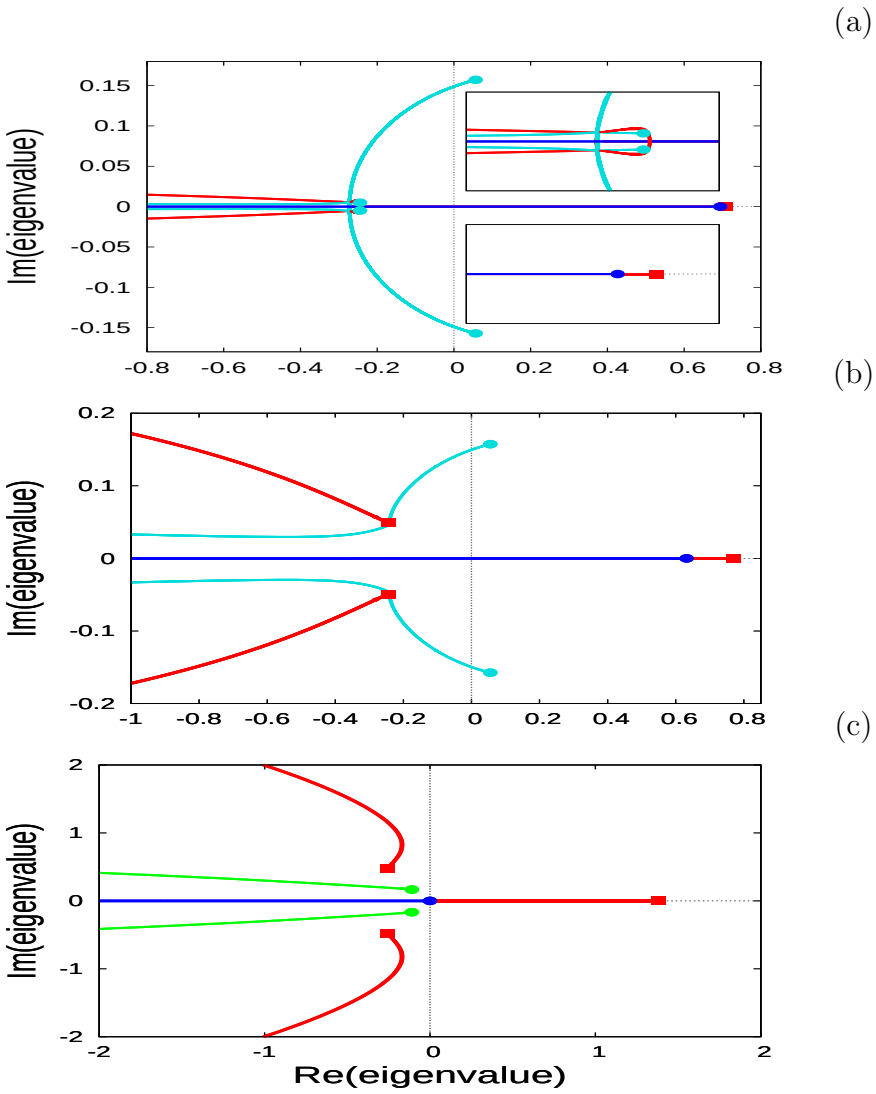

Figure 2.7: Illustrations of the absolute spectrum and generalised absolute spectrum for the Rosenzweig-MacArthur model (1). Branch points are indicated by filled circles and filled squares. The values of μ, a, b and d are fixed as follows: $\mu = 9.0$, $a = 1.3$, $b = 4$ and $d = 2$. The meaning of the colours is the same as on Figure 2.6. On Panel (a), the advection constant is $c = 0.01$ and the absolute spectra is unstable. The inserts show details of behaviour near branch points; $-0.35 < \mathrm{Re}\,\lambda < -0.2$ and $-0.03 < \mathrm{Im}\,\lambda < 0.03$ for the top insert while $0.64 < \mathrm{Re}\,\lambda < 0.73$ and $-0.01 < \mathrm{Im}\,\lambda < 0.01$ for the bottom insert. Note that a complex conjugate pair of triple points were found at $\lambda = -0.273 \pm 0.005i$ where the corresponding spatial eigenvalues satisfy $\mathrm{Im}\,k_1 = \mathrm{Im}\,k_2 = \mathrm{Im}\,k_3$; portions of the absolute spectrum emanate from these triple points. Panel (b) shows an unstable absolute spectrum for $c = 0.1$ while the absolute spectrum on Panel (c) is stable and corresponds to $c = -1$.

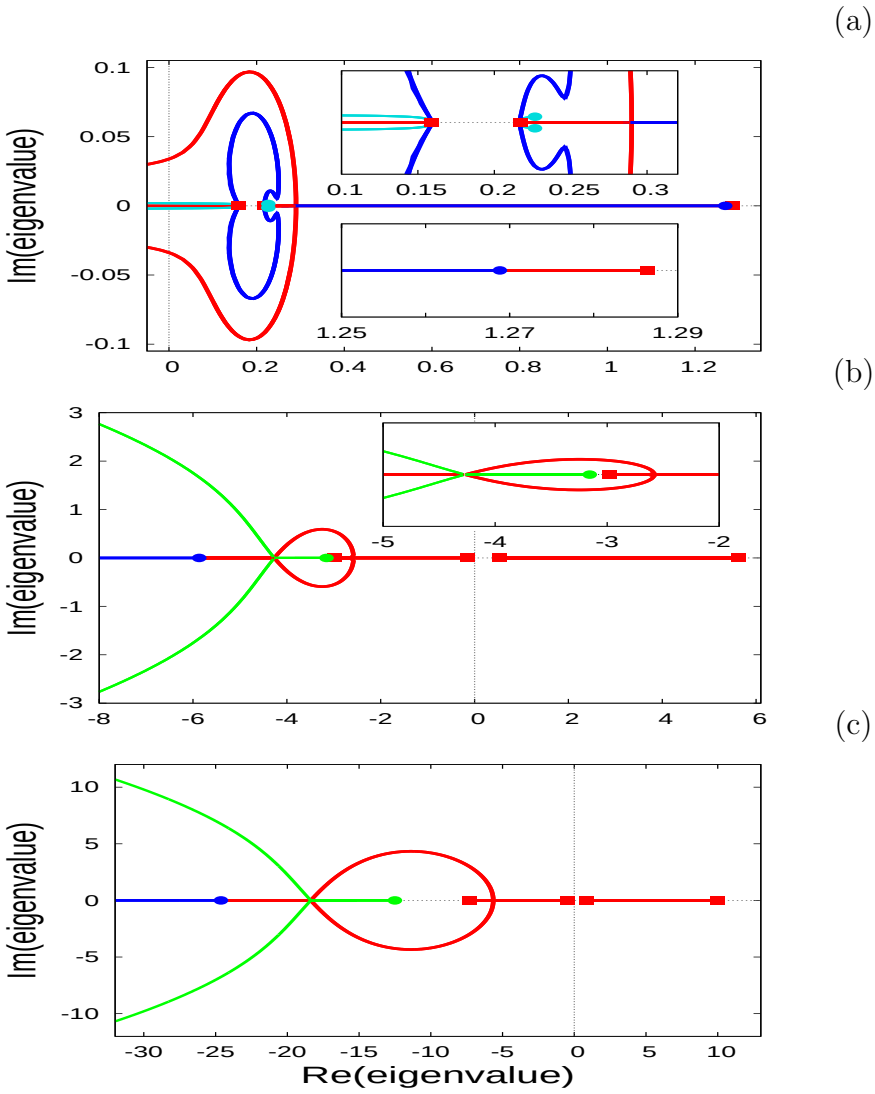

Figure 2.8: Illustrations of the absolute spectrum and generalised absolute spectrum for the Rosenzweig-MacArthur model (1). Branch points are indicated by filled circles and filled squares. The values of μ, a, b and d are fixed as follows: $\mu = 15$, $a = 1.3$, $b = 4$ and $d = 2$. The meaning of the colours is the same as on Figure 2.6. On Panel (a), the advection constant is $c = 0.01$ and the absolute spectra is unstable. The inserts show details of behaviour near branch points; the range on the vertical axis is $-0.012 < \mathrm{Im}\,\lambda < 0.012$ for the top insert while the range on the vertical axis is $-0.01 < \mathrm{Im}\,\lambda < 0.01$ for the bottom insert. Panels (b) and (c) both show stable absolute spectra and correspond respectively to $c = 5$ and $c = 10$; the range on the vertical axis on the insert on Panel (b) is $-2 < \mathrm{Im}\,\lambda < 2$. In all three cases, triple points were found and portions of the corresponding absolute spectra emanate from them.

lute spectrum does / does not extend into the right hand half of the complex plane.

More precise versions of these statements, including the required technical assumptions, are given in Sandstede & Scheel (2000*a*). Note that the "pinching condition" of Briggs (1964) translates to the condition that λ is a branch point in the absolute spectrum. Note also that in Chapter 1 we presented an intuitive argument motivating the relationship between the absolute spectrum and absolute stability.

Branch points are the key to numerical calculation of the absolute spectrum. Since $\mathcal{D}$ has a repeated root for k at a branch point, we have

$$\mathcal{D}(\lambda, k) = 0 \quad \text{and} \quad (\partial/\partial k)\mathcal{D}(\lambda, k) = 0\,. \tag{3}$$

Now $\mathcal{D}$ is a polynomial in both λ and k, and thus it is usually relatively straightforward to solve (3) for the branch points. For example, for (1) one can eliminate λ between the two equations in (3) to give a sixth order polynomial in k. This can be solved numerically and then each of the solutions can be substituted back into (3) to get the corresponding values of λ (see Appendix A.1 for further details).

Branch points will be in the absolute spectrum if their index is n^*. To check this for a given branch point, one substitutes the calculated value of λ back into $\mathcal{D}(\lambda, k) = 0$ and solves the resulting polynomial in k. Two of the roots will be the repeated pair corresponding to the branch point. If these are k_{n^*} and k_{n^*+1} then the branch point is in the absolute spectrum; otherwise it is not.

The above procedure may seem a little involved at first sight, but in practice it is very straightforward and very quick, involving just the numerical solution of polynomials. In the Appendix we demonstrate the calculation of the branch points for the Rosenzweig & Macarthur (1963) model (1) and the Klausmeier (1999) model (2).

Having calculated the branch points, one can proceed to calculate the entire generalised absolute spectrum via numerical continuation. Using a branch point of index j as a starting point, one performs a numerical continuation of the polynomial $\mathcal{D}(\lambda, k)$, using $\operatorname{Re} k_j - \operatorname{Re} k_{j+1}$ as a continuation variable. This method was proposed by Rademacher et al. (2007), and it is also described in detail in Smith et al. (2009); the latter paper includes an online supplement with a detailed tutorial guide and sample code. Repeating this procedure for each branch point generates the entire generalised absolute spectrum, since for constant coefficient problems all curves of generalised absolute spectrum emanate from a branch point, at least for a wide class of equations including reaction-diffusion systems (Rademacher et al. 2007). The same statement does not necessarily hold for the absolute spectrum itself; instead, curves of absolute spectrum can emanate from "triple points",

defined by $\operatorname{Im} k_i = \operatorname{Im} k_{i+1} = \operatorname{Im} k_{i+2}$ for some i (Rademacher et al. 2007, Smith et al. 2009). Therefore it is not possible to calculate the absolute spectrum directly using this approach. Rather it is necessary to calculate the generalised absolute spectrum, and to monitor all four roots for k of $D(\lambda, k) = 0$ as one moves along it. The absolute spectrum is simply the part of the generalised absolute spectrum for which $\operatorname{Im} k_{n^*} = \operatorname{Im} k_{n^*+1}$. See Figures 2.8a-c for examples of parts of absolute spectra emanating from triple points.

In practice one is interested in the most unstable point in the absolute spectrum, and also its most unstable branch point. Usually these are the same: this will be the case unless there is a non-transient convective instability (see §2.2). For some systems it has been proved that the most unstable point in the absolute spectrum is a branch point (Smith et al. 2009), but the complexity of most models of biological phenomena puts them outside the compass of these results. Therefore when considering absolute stability in a model for the first time, it is good practice to calculate the full absolute spectrum for a selection of parameter sets; usually these will show that the most unstable point in the absolute spectrum is a branch point in each case. One can then have confidence in making statements about absolute / convective / remnant / transient stability on the basis of branch points, which is usually a very simple calculation. In fact in the physics literature, where different types of instability are often considered, many authors draw their conclusions based only on calculations of branch points. As an example of a calculation done in this way, Figure 2.9 shows the boundary between convective and absolute stability of the coexistence steady state in the μ–c plane for (1), based simply on numerically solving a polynomial to determine the branch points, as described in Appendix A.1.

2.6 Quantitative Calculations Using Absolute Stability

The example in §2.3 illustrates how determination of the type of instability can be used to understand and predict important qualitative features of spatiotemporal behaviour. However the theory is in fact much more powerful than this. Quantitative information can also be obtained, by investigating stability in different frames of reference. We will demonstrate this for the solutions presented in §2.3, by adapting the method proposed by Sherratt et al. (2009) for invasions in reaction-diffusion systems of λ–ω type.

Given a PDE with space variable x and time variable t, one changes to a moving frame of reference in the usual way, by changing coordinates to $z = x - Vt$ and t. The frame velocity V is an additional parameter. For any given V, one can use the methods in §2.5 to calculate the most unstable point in the absolute spectrum, say $\lambda^*(V)$. This is

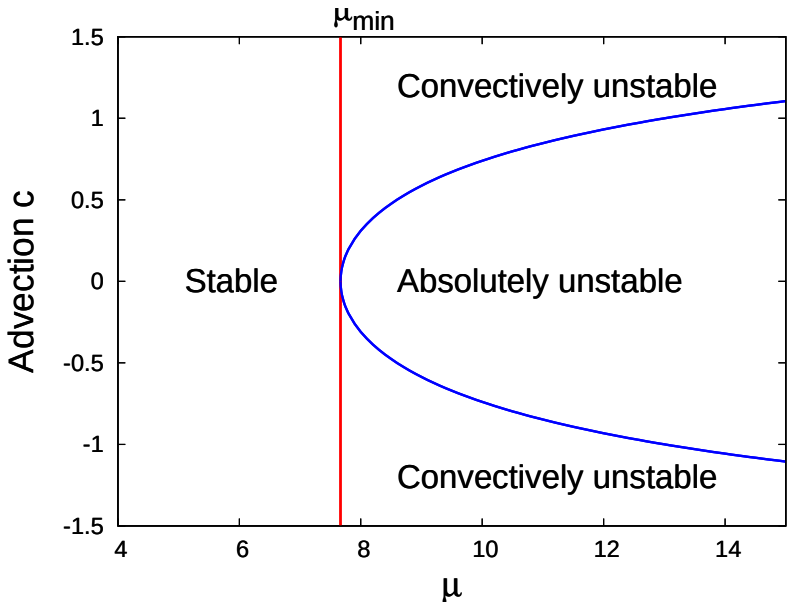

Figure 2.9: An example of stability boundaries in the (μ, c) plane for (1). The vertical red line marks the transition between the coexistence steady state being stable and unstable, while the blue curve shows the transition between convective and absolute instability. The latter curve was plotted via the calculation of branch points, as described in Appendix A.1. The parameter values were $a = 1.3, b = 4, d = 2$.

the eigenvalue associated with the most unstable linear mode moving with velocity V. We denote by k^* the corresponding value of k. Figure 2.10 shows a typical plot of $\mathrm{Re}\,\lambda^*$ against V, for the model (1). There is a finite range of velocities for which there are growing linear modes: all linear modes moving with speed $(= V)$ less than V_L or greater than V_R are decaying.

A plot such as Figure 2.10 is quite instructive in its own right. For example, we presented simulations in §2.1 showing that there can be a plateau region ahead of the invasion front in which the (unstable) coexistence steady state is "dynamically stabilised". Denoting the invasion velocity by V_{front}, the condition for such a plateau is $V_{\mathrm{front}} > V_R$, so that the invasion can outrun all growing linear modes (Dagbovie & Sherratt 2013). But the curve $\lambda^*(V)$ can also form the basis of calculations. For example, a natural question arising from the simulations shown in §2.3 is how the width of the steady state region depends on parameters. To determine this, note that the amplitude of a linear mode travelling with velocity V will double over the time period $\log(2)/\mathrm{Re}\,\lambda^*(V)$. During this time, the linear mode moves a distance $V\log(2)/\mathrm{Re}\,\lambda^*(V)$ while the transition front moves a distance $V_{\mathrm{front}}\log(2)/\mathrm{Re}\,\lambda^*(V)$. Recall that V_{front} is the speed of the front, which can be found using the theory of minimal spreading speeds (van Saarloos 2003); in the absence

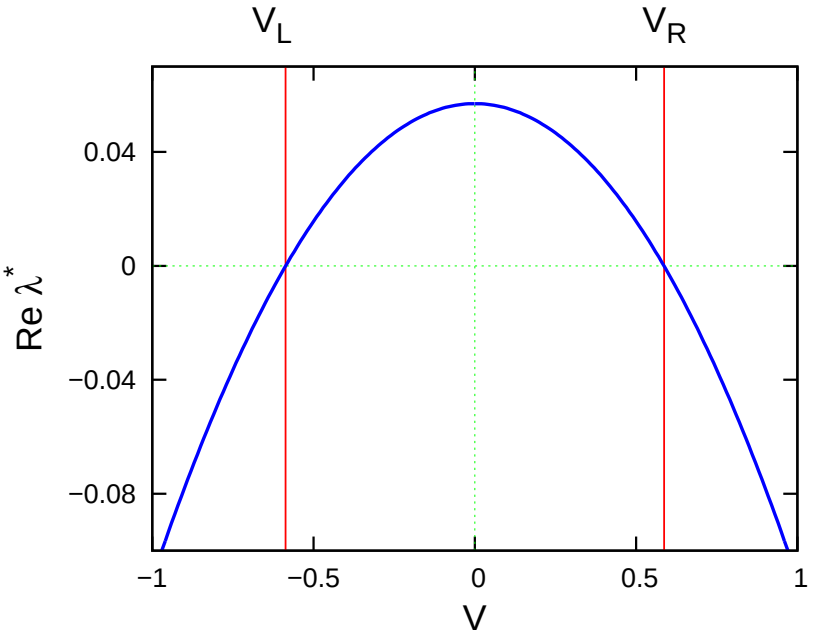

Figure 2.10: An example of the dependence of $\mathrm{Re}\,\lambda^*$ against V. For a given velocity V, $\lambda^*(V)$ is the most unstable point in the absolute spectrum, meaning that $\mathrm{Re}\,\lambda^*(V)$ is the maximum growth rate of perturbations moving with velocity V. The example shown is for the Rosenzweig & Macarthur (1963) model (1) with parameters $a = 1.3$, $b = 4$, $c = 0$, $d = 2$, $\mu = 9$. Calculation of the absolute spectrum for this case, with a variety of different V values, showed that the most unstable point in the absolute spectrum was a branch point in all cases. Therefore we determined $\lambda^*(V)$ by calculating branch points, as described in Appendix A.1.

of advection, this speed is given by $V_{\mathrm{front0}} = 2\sqrt{\frac{d}{ab}\left(\frac{a\mu}{\mu+1} - 1\right)}$ but in the context of this chapter, it is defined by $V_{\mathrm{front}} = -V_{\mathrm{front0}} - c$. Therefore the linear mode doubles in amplitude while moving a distance $(V - V_{\mathrm{front}})\log(2)/\mathrm{Re}\,\lambda^*(V)$ from the front. One can reasonably assume that the transition front applies a perturbation to the coexistence steady state that contains all unstable linear modes. Therefore the perturbation doubles in amplitude over the "doubling distance"

$$x_{dbl} = \log(2)(V_{dbl} - V_{\mathrm{front}})/\mathrm{Re}\,\lambda^*(V_{dbl}) \tag{4}$$

where V_{dlb} minimises $(V - V_{\text{front}})/\text{Re}\,\lambda^*(V)$, i.e.

$$(V_{dbl} - V_{\text{front}})\ \frac{d}{dV}\text{Re}\,\lambda^*(V)\Big|_{V=V_{dbl}} = \text{Re}\,\lambda^*(V_{dbl}). \tag{5}$$

More specifically, let (x^*, t^*) denote a point on the invasion front. When t increases above t^*, the perturbations applied to the steady state (u^*, v^*) by the invasion front spread out in time and space, growing along all rays $x = x^* + (t - t^*)V$ with V between V_L and V_R. In order to calculate precisely the width of the stabilised region, we must give a precise definition of its ends. The left-hand end is simply the invasion front, and we define the right-hand end to be the point at which perturbations applied to the steady state (u^*, v^*) by the invasion front first become amplified by a factor of 2. This occurs at time $t_{crit}(V) = t^* + \log(2)/\text{Re}[\lambda^*(V)]$, with the corresponding location being $x_{crit}(V) = x^* + V\log(2)/\text{Re}[\lambda^*(V)]$. Perturbations that move at a speed V_{dbl} are the first to be amplified by 2. Figure 3.12 shows an example of the curve $(x_{crit}(V), t_{crit}(V))$, $(V_L < V < V_R)$.

Numerical solution of (5) is made relatively straightforward by the following identity $(d/dV)\text{Re}\,\lambda^*(V)|_{V=V_{dbl}} = -\text{Im}\,k^*(V_{dbl})$ (Sherratt et al. 2009). In some cases (5) will have more than one solution: then the relevant solution is the one giving the smallest value of x_{dbl}; an example of this is given in Figure 5 of Sherratt et al. (2009). Figure 2.12 shows a plot of V_{front}, V_L and V_{dbl} as functions of μ. The steady state changes stability at $\mu_{min} \simeq 7.667$ and at this value, $V_L = V_{dbl} = -c$ (the perturbations are moving as fast as the advection); below this value, V_{dbl} and V_L do not exist. As μ increases from 7.667, V_L and V_{dbl} both decrease from $-c$. Initially $V_L < V_{dbl} < -c$ and at $\mu_{max} = 8.609$, $V_L = V_{dbl} = V_{\text{front}}$. For $\mu > 8.609$, the invasion front is able to outrun the perturbations, and there is no stabilised region. For $7.667 < k < 8.609$, perturbations travel faster than the invasion and dynamical stabilisation occurs.

The formula (4) for x_{dbl} contains all of the parameter dependence of the width of the steady state region in the simulations shown in §2.3. For example, Figure 2.13 plots x_{dbl} against estimates of the width from simulations as the parameter μ is varied, demonstrating their linear relationship.

2.6.1 Measuring the Width of the Steady State Region

To produce Figure 2.13, we needed to estimate the width of the stabilised region for each of the values of μ shown in numerical simulations of invasion in (1). To estimate this width in simulations, we need to determine the location of the invasion front (left-hand edge) and of the right-hand edge of the stabilised region. We choose the left-hand edge

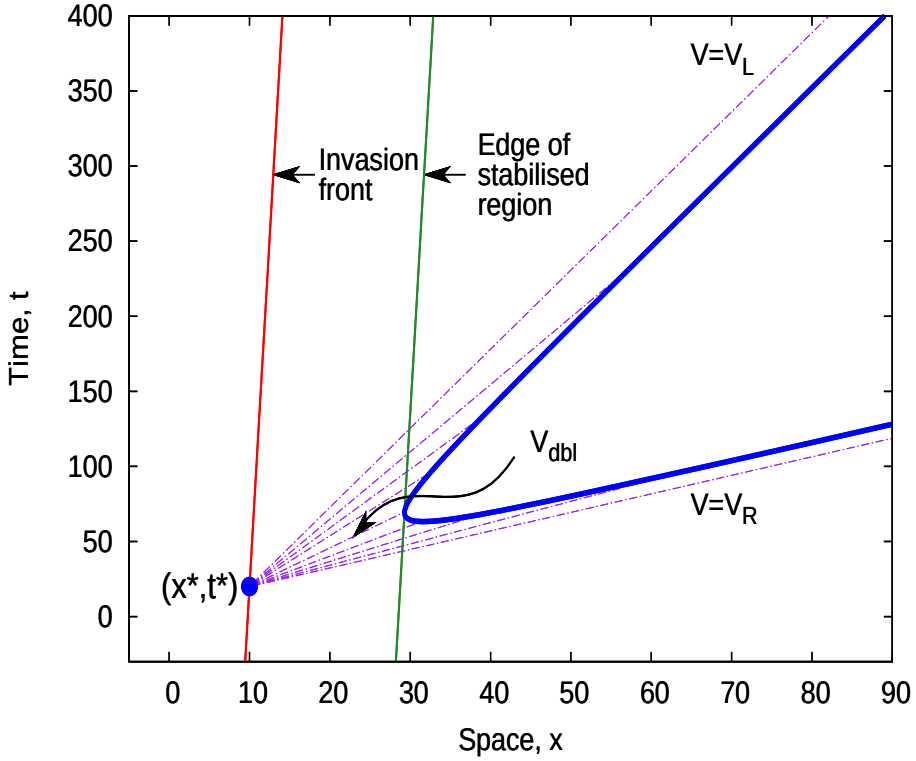

Figure 2.11: An illustration of the argument on which our calculation of the width of the stabilised region is based. The thick solid curve is a plot of calculated values, not a sketch, and the parameters are given by $b = 4$, $k = 8.0$ and $c = -0.5$. Then, if we view the point $(x^*, t^*) = (10, 20)$ in a frame of reference moving at a velocity V, with $V_L < V < V_R$, perturbations grow and spread out in time and space, reaching the point (x_{crit}, t_{crit}) (thick curve) when their amplitude has doubled. Perturbations moving at the velocity V_{dbl} reach the edge of stabilised region closest to the invasion front.

to be the point x_1 on the invasion front that is halfway between the coexistence steady state and the prey only steady state; that is the point at which the amplitude $\mathcal{A}$ equals $\frac{1}{2}\sqrt{(1-u^*)^2 + v^{*2}}$. Keeping in mind that the right-hand end is the first point in front of the stabilised region, we define it as the point x_2 at which $\mathcal{A} = \sqrt{(u-u^*)^2 + (v-v^*)^2}$ equals a small value, taken as 0.005. We estimate both x_1 and x_2 by linear interpolation between numerical grid points; of course they are both time-dependent. Now recall that the width of the stabilised region is a function of time, has a growth and then reaches a constant phase from a time value $t = t_1$. At a certain $t_2 > t_1$, the right-hand edge of the stabilised region reaches the right-hand boundary of the simulation domain. On Figure 2.14a, we show a space-time plot of how actual edges x_1 and x_2 from PDE simulations vary with time for $b = 4.0$, $\mu = 8.1$ and $c = -0.5$. On Figure 2.14b, we show for the same

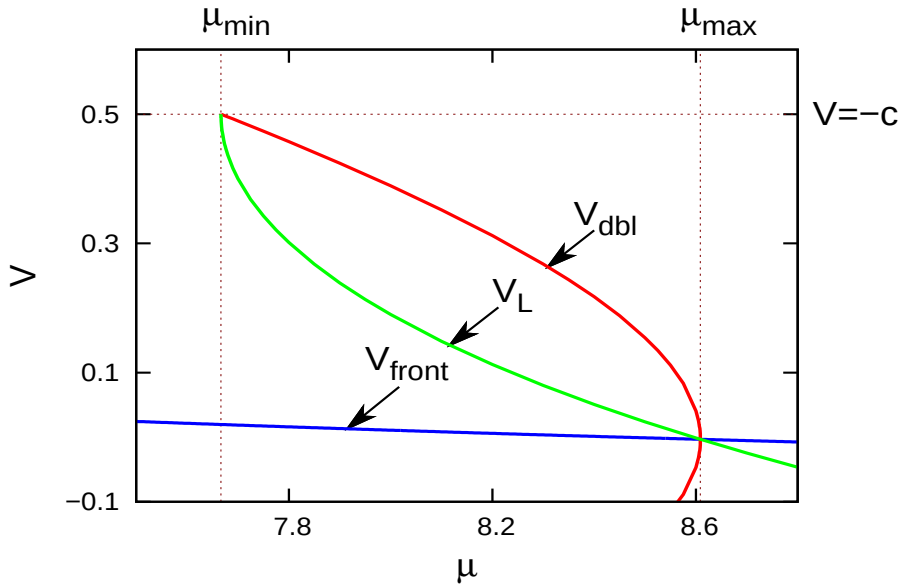

Figure 2.12: Plots of V_L, V_{dbl} and V_{front} against μ for $c = -0.5$; the other parameter values were $a = 1.3, b = 4, d = 2$. At $\mu = \mu_{min}$, the coexistence steady state becomes unstable. This value of μ is also characterised by $V_L = V_{dbl} = -c$. As μ increases, V_L and V_{dbl} decrease until $\mu = \mu_{max}$. For $\mu \in (\mu_{min}, \mu_{max})$, we have $V_{\text{front}} < V_L < V_{dbl}$, so that the unstable steady state is dynamically stabilised for these μ values. The V_{dbl} curve folds at $\mu = \mu_{max}$ while intersecting both the V_L and V_{front} curves. For $\mu > \mu_{max}$, the velocity V_{dbl} does not exist as Equation (5) has no solution. Meanwhile V_L has now become smaller than V_{front}: the invasion overtakes the unstable linear modes and dynamical stabilisation will no longer occur.

parameter values a space-time plot of how the estimated (as described above) edges x_1 and x_2 vary with time. Note that the $t(x_1)$ curve is smooth while $t(x_2)$ curve fluctuates. We find our estimation of the width by averaging the value of $x_2 - x_1$ over a time included in (t_1, t_2). Here $t_1 \simeq 5100$, $t_2 \simeq 72200$ and the invasion front reaches the right-hand boundary of the simulation domain at time $t_3 \simeq 97200$.

Note however that the time values t_1 and t_2 increase as μ increases; for example when $\mu = 8.3$, $t_1 = 6100$ and $t_2 = 99500$. It is hence important to choose a time range appropriate to all μ values over which the distances $x_2 - x_1$ are to be averaged. For the calculation on Figure 2.13, the time range used was $10000 < t < 40000$.

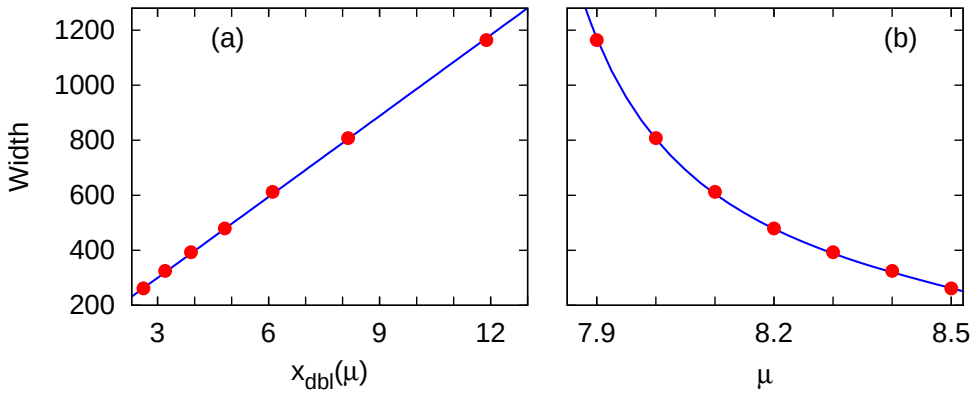

Figure 2.13: An illustration of the correlation between the doubling distance x_{dbl} and the width of the steady state region in simulations of (1) with the zero flux condition $h_x + ch = dp_x + cp = 0$ at the left hand boundary and the Danckwert condition $h_x = p_x = 0$ at the right hand boundary, as in Figure 2.5. The parameter μ was varied between 7.9 and 8.5. (a) A plot of x_{dbl} against the numerically calculated width (dots), showing a very strong linear correlation between the two quantities (regression coefficient = 0.999). This confirms that the dependence on parameters of the width of the steady state region is captured by x_{dbl}. The line is the best-fit regression line, which has slope 98.05 and intercept 5.795; there is a non-zero intercept because our method for measuring the width of the steady-state region excludes small portions on either side (see Sherratt et al. 2009 for further discussion). (b) A plot of the width of the steady state region (dots) against μ. We superimpose on this a curve showing x_{dbl}, rescaled using the regression line found from (a). The doubling distance was calculated using (4) and (5). The width of the steady state region was calculated using numerical simulations performed as in Figure 2.5. The method used to measure the width in numerical simulations is described in Dagbovie & Sherratt (2013). The parameter values were $a = 1.3, b = 4, c = -0.5, d = 2$.

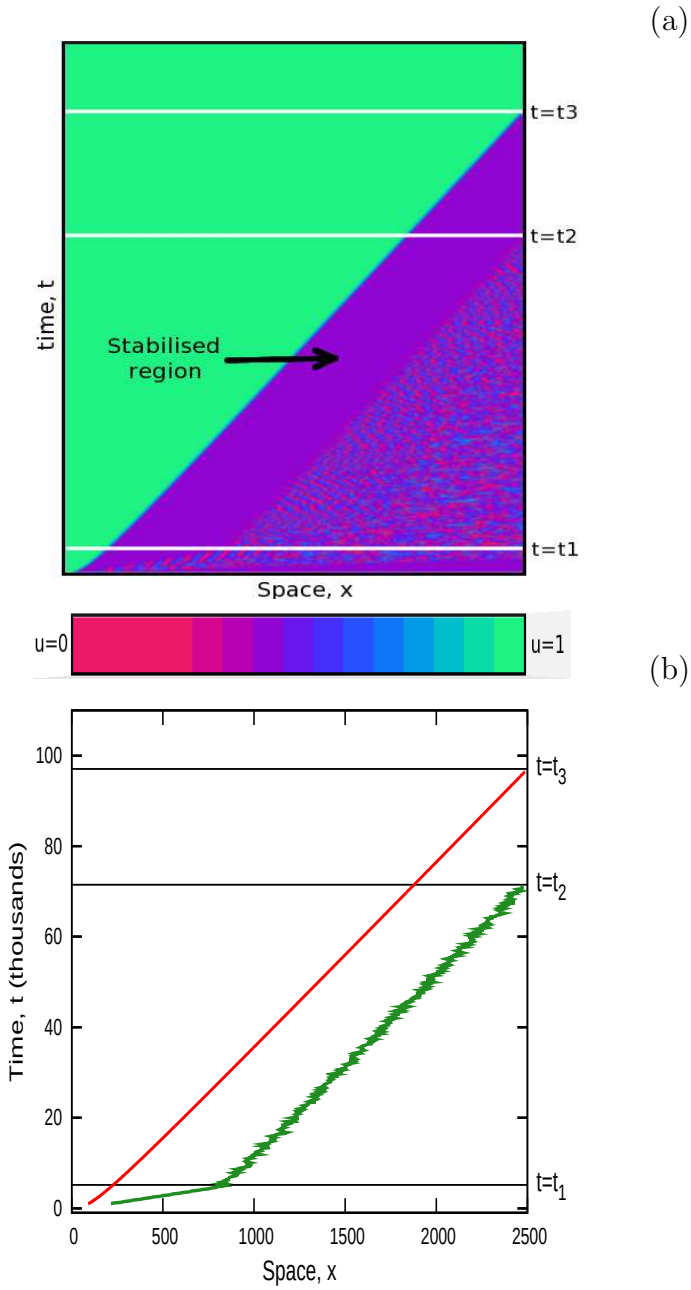

Figure 2.14: Panel (a): space-time plot showing how the edges of the stabilised region vary with time for $b = 4.0$, $\mu = 8.1$ and $c = -0.5$. The space variable x varies between 0 and 2500, with t between 0 and 110000. As t increases from zero, the stabilised region expands until $t_1 \simeq 5100$, after which the width remains constant. The right-hand edge of the stabilised region reaches the right-hand boundary of the domain ($x = 2500$) at $t_2 = 72200$. We have solved (1) numerically using a semi-implicit finite difference method with a grid spacing of 0.5 and time step of 0.05. Numerical simulations of the Rosenzweig & Macarthur (1963) model (1) with the zero flux condition $h_x + ch = dp_x + cp = 0$ at the left hand boundary and the Danckwert condition $h_x = p_x = 0$ at the right hand boundary. Initially the solution is at the coexistence steady state, but this is incompatible with the left hand boundary condition, and a transition front develops that replaces the coexistence steady state with the prey-only state. Panel (b) shows how the estimated edges x_1 and x_2 vary with time. The invasion front is represented by the red curve while the right-hand edge of the steady state region is represented by a green curve.

2.7 Summary and Discussion

Biology abounds with complex spatiotemporal phenomena. Mathematical models have been highly successful at reproducing this complexity, but currently our ability to numerically simulate such phenomena far outstrips our ability to provide an underlying mathematical understanding. As a result, models can sometimes fail to fulfil their potential for qualitative and quantitative prediction. The theory of absolute stability provides a tool that has the potential to redress this inbalance in some cases, and whose use within mathematical biology is currently almost non-existent. Until recently one had to overcome a steep learning curve to make practical use of this theory, but new computational methods based on the absolute spectrum now make it easily accessible to non-specialists. We hope that this article will encourage greater use of these methods within the mathematical biology community.

We have focussed on the stability of spatially homogeneous solutions, for which both the theory and methods for numerical calculation are most complete. The absolute stability of spatially varying solutions was first considered by Brevdo & Bridges (1996), 1997b). Most of the key concepts that we have discussed extend from homogeneous solutions to a wide variety of non-uniform solutions, including solutions of reaction-diffusion systems that approach either constant or spatially periodic states at infinity. One complication is that the absolute spectrum can be augmented by discrete eigenvalues, and Wheeler & Barkley (2006) discuss an example of spiral wave break-up in which absolute stability is determined by discrete eigenvalues rather by than the absolute spectrum. However, for large classes of systems it can be shown there are no such discrete eigenvalues: this includes spatially homogeneous solutions, and wavetrain solutions of reaction-diffusion systems (Sandstede 2002, §3.4.2).

The biggest difficulty when considering spatially varying solutions is numerical calculation. Numerical continuation is still a viable method for calculation of the absolute spectrum (Rademacher et al. 2007), but finding appropriate starting points is problematic. In particular, branch points lose their suitability because for spatially varying solutions there are in general infinitely many branch points (Rademacher et al. 2007, §4.3). Alternative approaches to the generation of starting points are discussed in §4.4 of Rademacher et al. (2007), but in most cases the only systematic way of calculating absolute stability for non-constant solutions is the method of Brevdo and coworkers (Brevdo 1995, Brevdo et al. 1999; see also Suslov 2006).

The restriction to spatially uniform solutions is more inclusive than it appears superficially. For example, wavetrain solutions to reaction-diffusion systems of "λ–ω type"

are spatially uniform when the equations are written in phase-amplitude form (Kopell & Howard 1973), and the same is true for wavetrains in the complex Ginzburg-Landau equation (Aranson & Kramer 2002). Also the absolute spectrum of wave fronts and pulses in reaction-diffusion systems depends only on the asymptotic states behind and ahead of the wave (Sandstede 2002, §3.4.3-3.4.4), although in this case one will also need to consider discrete eigenvalues, and these do depend on the wave profile.

We also emphasise that our remarks only concern behaviour in one space dimension. Absolute stability has been widely used to study spiral wave break-up (e.g. Aranson et al. 1992, Sandstede & Scheel 2000*b*, Wheeler & Barkley 2006), but this is effectively a one-dimensional problem. There has been some discussion of absolute stability for genuinely two-dimensional solutions in the hydrodynamics literature (e.g. Chomaz 2004, Biancofiore et al. 2011), but a detailed theory is currently lacking. This, and more effective numerical methods for spatially varying solutions, are major current objectives for the research community working on absolute stability.

In ecology, the term 'stability' plays a central role. In their 1997 review of the ecological literature, Grimm & Wissel found 163 definitions of 70 different stability concepts. Yet, the theory of absolute stability has been, to our knowledge, absent from the ecological literature, and it appears that the spatial dimension is generally lacking in ecological stability concepts.

This is particularly surprising since stream ecologists (and water resource managers alike) have long been on the quest how lotic systems respond to disturbances and spatial variabilities. Much of the current knowledge comes from experiments in study sites that comprise only a small fragment of the stream or river (Fausch et al. 2002). But how do populations much further downstream, i.e. outside the study arena, respond to upstream perturbations (Cooper et al. 1998)? This is a key question in the assessment of instream flow needs, or how the location of wastewater treatment plants affects environmental conditions downstream (Anderson et al. 2006). One attempt to address this question is the concept of the response length (Anderson et al. 2005), a characteristic length scale measuring the scale over which environmental disturbances are felt by distant populations.

Convective instabilities appear particularly intriguing in this context. The perturbed steady state remains stable locally, but is enormously brought out of equilibrium further downstream (cf. Figure 2.5b). Small-scale experiments and observations might only see the local (stable) response, but miss out on the instabilities arising further away. In §6 we have shown how the width of the region where the steady state remains stable can be calculated quantitatively (see also Dagbovie & Sherratt 2013). This may be useful information for the design of experiments, ecological monitoring as well as environmental

assessment.

The convective and absolute instabilities that we have described do not necessarily need to be 'harmful' to the populations. On the contrary, the spatiotemporal oscillations caused by the instabilities can be beneficial. For example, they might facilitate non-equilibrium coexistence of species that would otherwise mutually exclude each other (Armstrong & McGehee 1980, Huisman & Weissing 1999). For example, Scheuring et al. (2000) have shown that the chaotic flow around a cylindrical obstacle creates a small-scale mosaic ensuring that coexisting species can coexist. Similarly, Lee (2012) has argued that rotational flow, as caused by a rock, can increase survival probabilities of predators and prey. Petrovskii et al. (2004) have shown, in a non-advective model, that spatiotemporal chaos can reverse the paradox of enrichment and thus make the persistence of predators and prey more likely.

Advective environments feature a number of spatiotemporal pattern formation mechanisms that cannot arise in non-advective systems. Interestingly, they do not require activator–inhibitor type of interactions as for diffusion-driven (Turing) instabilities, but they critically depend on either a significant difference in the flow experienced by species (Rovinsky & Menzinger 1992, Perumpanani et al. 1995, Malchow 2000) or resource-dependent dispersal (Anderson et al. 2012). Neither of these conditions are necessary for the convective and absolute instabilities considered here, but it should be noted that the steady state of the kinetic ODEs is unstable in the first place. This, however, is a situation that arises frequently in nature (e.g. Turchin 2003).

Streams and river are particularly iconic examples of flow-dominated systems, but there are many others. Marine organisms dispersed in longshore currents or plant seeds and insects dispersed by winds with a prevailing wind direction (Levine 2003) are also environments with a predominantly unidirectional flow. These systems are strongly characterised by the importance of longitudinal transport through habitat. The theory of absolute stability appears to have a lot to offer when there is a downstream bias that can induce very different spatial responses to localised perturbations.

Appendix: Examples of Calculating Branch Points

In this Appendix we show how to calculate the branch points for the Rosenzweig-MacArthur model (1) and the Klausmeier model (2). We present these calculations in some detail.

A.1 Branch Points for the Rosenzweig-MacArthur Model

Recall that the Rosenzweig-MacArthur model (1) has a unique homogeneous coexistence steady state (h_s, p_s) where $h_s = 1/(a\mu - \mu)$ and $p_s = (1 - h_s)(1 + \mu h_s)/\mu$. We begin by linearising (1) about (h_s, p_s) giving

$$\begin{aligned}\tilde{p}_t &= \alpha\tilde{p} + \beta\tilde{h} + c\tilde{p}_x + d\tilde{p}_{xx}\\ \tilde{h}_t &= \gamma\tilde{p} + \delta\tilde{h} + c\tilde{h}_x + \tilde{h}_{xx}\end{aligned}$$

where $\tilde{p} = p - p_s$, $\tilde{h} = h - h_s$, and $\alpha,\ \beta,\ \gamma,\ \delta$ are coefficients from linearisation and are given by

$$\begin{aligned}\alpha &= \frac{\mu h_s}{b(1+\mu h_s)} - \frac{1}{ab}\\ \beta &= \frac{\mu p_s}{b(1+\mu h_s)^2}\\ \gamma &= 1 - 2h_s - \frac{\mu p_s}{(1+\mu h_s)^2}\\ \delta &= -\frac{\mu h_s}{1+\mu h_s}\,.\end{aligned}$$

Substituting $(\tilde{p}, \tilde{h}) = (\bar{p}, \bar{h})\exp(ikx + \lambda t)$ into (1) and requiring $\bar{p}$ and $\bar{h}$ to be non-zero gives the dispersion relation

$$\begin{aligned}\mathcal{D}(\lambda, k) &= dk^4 - cik^3(d+1) - k^2(\alpha - \lambda + d\gamma - d\lambda + c^2)\\ &\quad + cik(\gamma + \alpha - 2\lambda) + (\alpha - \lambda)(\gamma - \lambda) - \delta\beta = 0\,.\end{aligned} \tag{A.1}$$

Branch points are double roots of the dispersion relation for k, and satisfy (A.1) and also

$$\begin{aligned}0 = \partial\mathcal{D}/\partial k &= 4dk^3 - 3k^2(1+d)ci - 2k(\gamma + d\alpha - (1+d)\lambda) + c^2 + ci(\alpha + \gamma - 2\lambda)\\ \Rightarrow \lambda &= \frac{4dk^3 - 3cidk^2 - 2dk\gamma + \alpha ci - 2c^2k - 3cik^2 - 2\alpha k + ci\gamma}{-2(k + dk - ci)}\,.\end{aligned} \tag{A.2}$$

Substituting (A.2) into (A.1) gives the following hexic polynomial in k:

$$\begin{aligned}&\left[-4d(d-1)^2\right]k^6+\left[2ci(d+1)(d-1)^2\right]k^5+\left[(d-1)(c^2d+8d\alpha-8d\gamma-c^2)\right]k^4\\&+\left[4ci(-\alpha+\gamma)(d-1)(d+1)\right]k^3+\left[2c^2(d-1)(\gamma-\alpha)-4\beta\delta(d+1)^2-4d(\alpha-\gamma)^2\right]k^2\\&+\left[2i(4\beta\delta+\alpha^2-2\alpha\gamma+\gamma^2)c(d+1)\right]k+c^2(4\beta\delta+\alpha^2-2\alpha\gamma+\gamma^2)=0\,.\end{aligned}\tag{A.3}$$

We must now proceed numerically and we fix $a=1.3$, $b=4.0$, $c=-1$, $d=2$ and $\mu=9$. These parameter values satisfy $\mu>\mu_{crit}$, so that the coexistence steady state is unstable. Substituting these values into (A.3), we obtain six roots for k, two real and two pairs of complex conjugates. We then substitute each into (A.2) to find the corresponding value of λ. To determine whether these branch points belong to the absolute spectrum, we substitute each λ value into (A.1) and solve for k, giving the repeated roots found from (A.3) and two others.

Branch point $k=0.676i$. Substituting this value of k into (A.2) gives $\lambda=1.380$. Substituting this value of λ back into (A.1) gives a quartic polynomial for k whose roots are $-1.727i$, $-1.125i$, $0.676i$, $0.676i$. Recall that a branch point is in the absolute spectrum if the repeated roots are k_2 and k_3, when the roots k_1, k_2, k_3 and k_4 of (A.1) are labelled in increasing order of their imaginary parts. In this case the repeated roots are k_3 and k_4 so that the branch point is not in the absolute spectrum.

Branch point $k=-0.473-0.013i$. Substituting this value of k into (A.2) gives $\lambda=-0.255+0.483i$. Substituting this value of λ back into (A.1) gives a quartic polynomial for k whose roots are $0.570-0.943i$, $0.377-0.530i$, $-0.473-0.013i$, $-0.473-0.013i$ Therefore the repeated roots are k_3 and k_4 so that the branch point is not in the absolute spectrum.

Branch point $k=0.473-0.013i$. Substituting this value of k into (A.2) gives $\lambda=-0.255-0.483i$. Substituting this value of λ back into (A.1) gives a quartic polynomial for k whose roots are $-0.570-0.943i$, $-0.377-0.530i$, $0.473-0.013i$, $0.473-0.013i$. the repeated roots are k_3 and k_4 so that the branch point is not in the absolute spectrum.

Branch point $k=0.001-0.334i$. Substituting this value of k into (A.2) gives $\lambda=-0.110-0.167i$. Substituting this value of λ back into (A.1) gives a quartic polynomial for k whose roots are $-0.314-0.816i$, $0.001-0.334i$, $0.001-0.334i$, $0.312-0.0165i$. Therefore the repeated roots are k_2 and k_3 so that the branch point is in the absolute spectrum.

Branch point $k = -0.001 - 0.334i$. Substituting this value of k into (A.2) gives $\lambda = -0.110 + 0.167i$. Substituting this value of λ back into (A.1) gives a quartic polynomial for k whose roots are $0.314 - 0.816i$, $-0.001 - 0.334i$, $-0.001 - 0.334i$, $-0.312 - 0.0165i$. Therefore the repeated roots are k_2 and k_3 so that the branch point is in the absolute spectrum.

Branch point $k = -0.732i$. Substituting this value of k into (A.2) gives $\lambda = 0.000$. Substituting this value of λ back into (A.1) gives a quartic polynomial for k whose roots are $-0.732i$, $-0.732i$, $0.160 - 0.017i$, $-0.160 - 0.017i$. Therefore the repeated roots are k_1 and k_2 so that the branch point is not in the absolute spectrum.

Therefore of the six branch points, two are in the absolute spectrum, with the corresponding eigenvalues being $-0.110 \pm 0.167i$. Since these eigenvalues have negative real parts, the steady state (h_s, p_s) is absolutely stable. To determine whether the convective instability is of transient or remnant type, it is necessary to calculate the absolute spectrum. This can be done via numerical continuation of the generalised absolute spectrum, using the six branch points listed above as starting points, as discussed in §2.5. This shows that the branch points are the most unstable points in the absolute spectrum, so that the steady state has a transient convective instability.

A.2 Branch Points for the Klausmeier Model

For all parameters, the Klausmeier model (2) has a "desert" steady state $m = 0$, $w = A$. When $A \geq 2B$ there are two further steady states $(m_\pm, w_\pm)$ where

$$m_\pm = \frac{2B}{A \pm \sqrt{A^2 - 4B^2}}, \quad w_\pm = \frac{A \pm \sqrt{A^2 - 4B^2}}{2}.$$

Ecologically realistic values of B are relatively small, and in particular satisfy $B < 2$ (Klausmeier 1999, Rietkerk et al. 2002). Under this constraint, (m_-, w_-) is stable as a solution of the kinetics ODEs, although it can be destabilised by the diffusion and advection terms, leading to spatial patterns (Klausmeier 1999, Sherratt 2005,Sherratt 2010). However (m_+, w_+) is unstable as a solution of the kinetic ODEs, and we will consider the nature of its instability as a solution of the PDEs (2).

We begin by linearising (2) about (m_+, w_+), giving

$$\tilde{m}_t = a\tilde{m} + b\tilde{w} + \tilde{m}_{xx} \tag{A.4a}$$

$$\tilde{w}_t = c\tilde{m} + d\tilde{w} + \nu\tilde{w}_x \tag{A.4b}$$

where $\tilde{m} = m - m_+$, $\tilde{w} = w - w_+$, and the linear coefficients α, β, γ, δ are given by

$$\tilde{\alpha} = B \tag{A.5a}$$

$$\tilde{\beta} = \frac{A - \sqrt{A^2 - 4B^2}}{A + \sqrt{A^2 - 4B^2}} \tag{A.5b}$$

$$\tilde{\gamma} = -2B \tag{A.5c}$$

$$\tilde{\delta} = \frac{-2A}{A + \sqrt{A^2 - 4B^2}}\,. \tag{A.5d}$$

Substituting $\left(\tilde{m}, \tilde{w}\right) = \left(\overline{m}, \overline{w}\right) \exp(ikx + \lambda t)$ into (A.2.4,A.2.5) and requiring $\overline{m}$ and $\overline{w}$ to be non-zero gives the dispersion relation

$$\tilde{\mathcal{D}}(\lambda, k) = \lambda^2 + \lambda\left(k^2 - \tilde{\alpha} - ik\nu - \tilde{\delta}\right) + (\tilde{\alpha} - k^2)(ik\nu + \tilde{\delta}) - \tilde{\beta}\tilde{\gamma} = 0\,. \tag{A.6}$$

Branch points are double roots (for k) of the dispersion relation, and satisfy (A.6) and also

$$\begin{aligned} 0 = \partial\tilde{\mathcal{D}}/\partial k &= \lambda\,(2k - i\nu) - \left(3ik^2\nu + 2\tilde{\delta}k - i\nu\tilde{\alpha}\right) \\ \Rightarrow\ \lambda &= \left(3ik^2\nu + 2\tilde{\delta}k - i\nu\tilde{\alpha}\right) / \left(2k - i\nu\right)\,. \end{aligned} \tag{A.7}$$

Substituting (A.7) into (A.6) gives a quintic polynomial in k:

$$\begin{aligned} \left(3ik^2\nu + 2\tilde{\delta}k - i\nu\tilde{\alpha}\right)^2 + (2k - i\nu)\left(3ik^2\nu + 2\tilde{\delta}k - i\nu\tilde{\alpha}\right)\left(k^2 - \tilde{\alpha} - ik\nu - \tilde{\delta}\right) \\ + (2k - i\nu)^2\left[(\tilde{\alpha} - k^2)(ik\nu + \tilde{\delta}) - \tilde{\beta}\tilde{\gamma}\right] = 0\,. \end{aligned} \tag{A.8}$$

We must now proceed numerically, and we will fix the parameter values to be $A = 2$, $B = 0.5$ and $\nu = 20$. These parameters satisfy the condition $A > 2B$ but otherwise they are chosen arbitrarily. The value $\nu = 20$ is too small for ecological realism: the formula for the dimensionless parameter ν involves the ratio of the advection rate of water and the (square root of the) plant diffusion coefficient (Klausmeier, 1999; (Sherratt 2005), so that ν is relatively large, with Klausmeier's (1999) estimate being 182.5. However we use the smaller value to improve the clarity of the numerical calculations. Substituting the parameter values into (A.8) gives five distinct roots for k, two complex and three pure imaginary. For each we substitute into (A.7) to find the corresponding value of λ. We then substitute this value of λ into (A.6) to determine whether the branch point is in the absolute spectrum. We performed all of the various calculations using the software package MAPLE with 20 decimal places, but for clarity we give results to 3 decimal places.

Branch point $k = -0.099 + i\,0.012$. Substituting this value of k into (A.7) gives $\lambda = 0.473 + i\,0.022$. Substituting this value of λ back into (A.6) gives a cubic polynomial for k whose roots are $-0.099 + i\,0.012$, $-0.099 + i\,0.012$, $0.199 - i\,0.101$. Recall from §2.5 that the branch point is in the absolute spectrum if the repeated roots are k_2 and k_3, when the roots k_1, k_2, k_3 of (A.6) are labelled in increasing order of their imaginary parts. Therefore in this case the branch point is in the absolute spectrum.

Branch point $k = -i\,19.950$. Substituting this value of k into (A.7) gives $\lambda = 398.112$. Substituting this value of λ back into (A.6) gives a cubic polynomial for k whose roots are $-i\,19.950$, $-i\,19.950$ and $i\,19.94$. Therefore the repeated roots are k_1 and k_2, so that this branch point is not in the absolute spectrum.

Branch point $k = -i\,19.892$. Substituting this value of k into (A.7) gives $\lambda = 396.587$. Substituting this value of λ back into (A.6) gives a cubic polynomial for k whose roots are $-i\,19.892$, $-i\,19.892$ and $i\,19.902$. Therefore the repeated roots are k_1 and k_2, so that this branch point is not in the absolute spectrum.

Branch point $k = -i\,0.181$. Substituting this value of k into (A.7) gives $\lambda = 0.569$. Substituting this value of λ back into (A.6) gives a cubic polynomial for k whose roots are $-i\,0.181$, $-i\,0.181$ and $i\,0.281$. Therefore the repeated roots are k_1 and k_2, so that this branch point is not in the absolute spectrum.

Branch point $k = 0.099 + i\,0.012$. Substituting this value of k into (A.7) gives $\lambda = 0.473 - i\,0.022$. Substituting this value of λ back into (A.6) gives a cubic polynomial for k whose roots are $-0.199 - i\,0.101$, $0.099 + i\,0.012$ and $0.099 + i\,0.012$. Therefore the repeated roots are k_2 and k_3, so that this branch point is in the absolute spectrum.

Therefore of the five branch points, two are in the absolute spectrum, with the corresponding eigenvalues being $0.473 \pm i\,0.022$. Since these eigenvalues have positive real part, the steady state (m_+, w_+) is absolutely unstable.

Chapter 3

Absolute Stability and Dynamical Stabilisation in Predator-Prey Systems

This chapter is based on our paper Dagbovie & Sherratt (2013).

3.1 Introduction

Ecological invasion is a widespread phenomenon with important environmental and economic impacts (Matsumura et al. 2004, Tokarska-Guzik et al. 2008). Moreover, invasions are occurring with increasing frequency due to climate change, which can enable previously non-invasive species to invade (Hellmann et al. 2008). This chapter concerns one particular class of invasions: the spread of a predator into a population of its prey. This process has been explored in many mathematical modelling studies using models formulated as partial differential equations (pdes), integrodifference equations, cellular automata and others (Dunbar 1984, Owen & Lewis 2001, Sherratt 2001, Sherratt et al. 1997). In simple cases, invasion takes the form of a transition wavefront, with a prey-only equilibrium ahead of the front and constant coexistence of predator and prey behind it. In such cases, the main question of interest is the dependence of the invasion speed on ecological parameters.

A characteristic feature of predator-prey interactions is their ability to generate population cycles. This feature of predator-prey models dates back to the original work of Lokta and Volterra (Lotka 1925, Turchin 2003, May & Mclean 2007, Volterra 1926), and empirical studies have confirmed predation as the cause of cycling in some prey populations (Korpimäki et al. 2002). For cyclic interactions, invasion of prey by predators is inevitably more complicated: the constant coexistence of predators and prey is unstable; therefore homogeneity cannot be expected as the only behaviour behind the invasion

front. Instead, a number of modelling studies have predicted spatiotemporal oscillations organised into periodic travelling waves (Garvie 2007, Petrovskii et al. 1998, Sherratt 2001). Such waves have been found in spatiotemporal data sets on a number of natural populations (Sherratt & Smith 2008), with invasion being among the factors proposed for their generation.

The change from a simple invasive transition wave to a periodic wave behind the invasion front as parameters are varied occurs because the coexistence equilibrium becomes unstable. However, numerical simulations show that, in many cases, the invasion front and the periodic travelling wave are separated by a region in which the solution is approximately at the coexistence equilibrium. In the early stages of an invasion, this region expands until it eventually reaches a maximum width which then remains constant as the invasion proceeds (see Figure 3.1 for a typical space-time plot showing the dependence on time of the width). The existence of a region in which the solution is approximately at the unstable coexistence steady state is known as "dynamical stabilisation" (Petrovskii & Malchow 2000, Malchow et al. 2008, Petrovskii et al. 2001, Malchow & Petrovskii 2002) and it is a major feature of predator-prey invasions for a wide range of parameter values. Although the analysis in this chapter is quite general, all of our numerical examples are for the Rosenzweig & Macarthur's (1963) model which assumes logistic growth for the prey population and a Holling type 2 response to predation:

$$u_t = D_u u_{xx} + f(u,v) \tag{3.1a}$$

$$v_t = D_v v_{xx} + g(u,v) \tag{3.1b}$$

$$\text{with } f(u,v) = u(1-u) - \frac{kuv}{1+ku} \tag{3.1c}$$

$$g(u,v) = \frac{1}{b}\left(\frac{kuv}{1+ku}\right) - \frac{v}{ab}. \tag{3.1d}$$

Here the variables u and v are prey and predator densities at time t and spatial location x in a one dimensional domain. We will focus on two different values of b; firstly $b = 3.0$ and later $b = 1.2$. In both cases, we vary k with the other parameter values fixed as follows:

$$a = 1.3, D_u = 1 \text{ and } D_v = 2. \tag{3.1e}$$

The model (3.1a-d) has a unique coexistence steady state (u^*, v^*) with $u^* = 1/(ak-k)$ and $v^* = (1-u^*)(1+ku^*)/k$. Standard linear stability analysis indicates that (u^*, v^*)

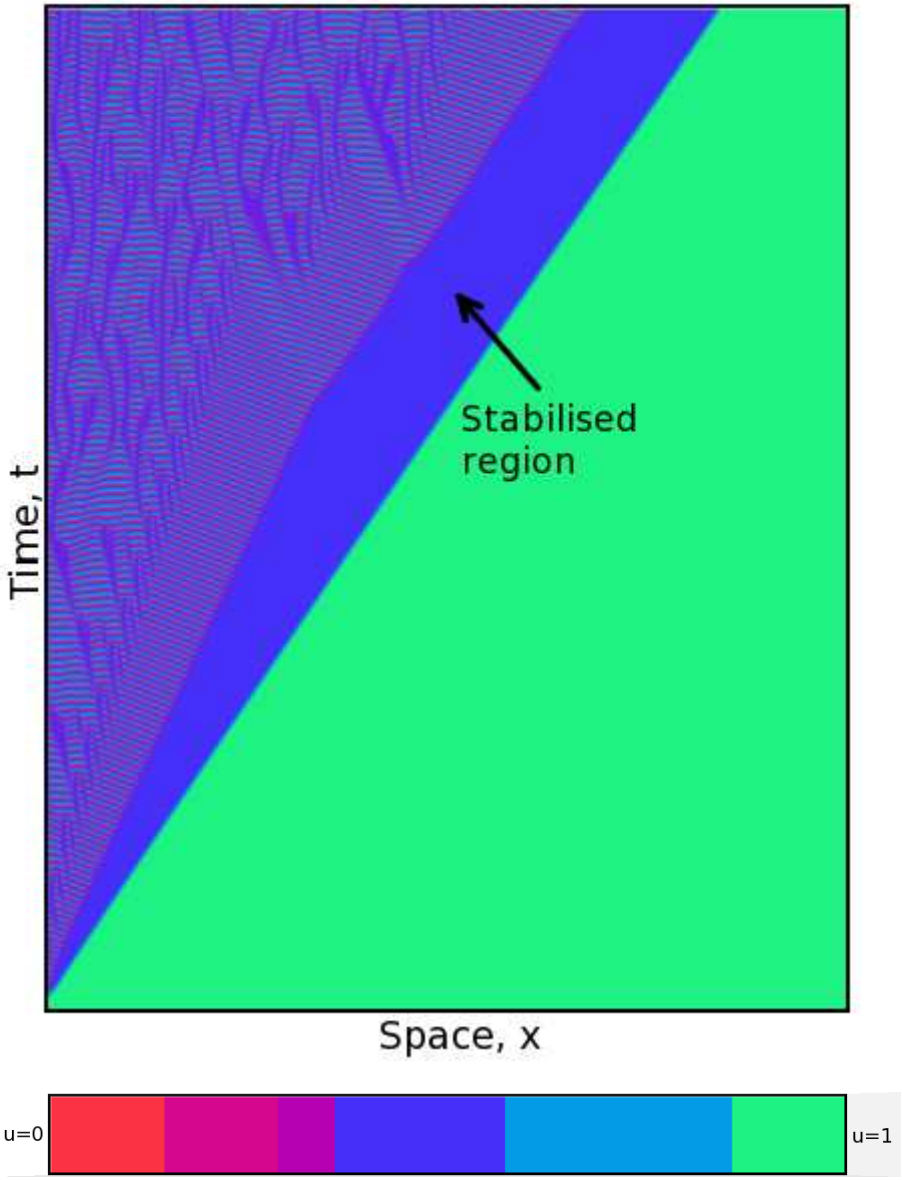

Figure 3.1: Space-time plot showing how the edges of the stabilised region vary with time for $b = 3.0$ and $k = 8.2$. All other parameters are as in (3.1e). The space variable x varies between 0 and 4000, with t between 0 and 6000. As t increases from zero, the stabilised region expands until $t \simeq 2745$, after which the width remains constant. We have solved (3.1) numerically using a semi-implicit finite difference method with a grid spacing of 0.5 and time step of 10^{-2}. Our initial condition is given by the prey-only state $u(x, 0) = 1$ and $v(x, 0) = 0$ with a slight perturbation near $x = 0$; we assume that there is no flux on both ends of the domain giving the boundary conditions $u_x = v_x = 0$ at $x = 0$ and $x = 4000$. Note that the scale bar has been deliberately made discrete, in order to achieve better clarity.

is unstable for $k \geq (a+1)/(a-1) = k_{min}$ and stable to homogeneous perturbations for $k < k_{min}$.

Figure 3.2 shows numerical simulations of invasions using (3.1), for four different values of k, with the other parameters fixed (as in (3.1e), with $b = 3.0$). In (a), $k < k_{min} = 7.67$ and the system settles to the stable coexistence steady state (u^*, v^*) behind the invasion front. In (b) and (c) there is a clear "stabilised region" in which the solution is very close to (u^*, v^*), before the onset of spatiotemporal oscillations. Note that the stabilised region is wider for (b) which has the smaller of the two k values. In (d), there is no dynamical stabilisation, and spatiotemporal oscillations develop immediately behind the invasion front.

The phenomenon of dynamical stabilisation has been studied in detail by Petrovskii and coworkers (2000, 2002, 2001). Their numerical simulations were run for relatively short times, and as a result they only observed the initial phase of the solution, in which the width of the stabilised region grows at a constant rate. Petrovskii and coworkers (2002, 2001) calculated the growth rate by applying linear spreading speed theory (van Saarloos 2003) to the interface between the coexistence steady state and spatiotemporal oscillations. The condition for dynamical stabilisation to occur at all is that this interface moves more slowly than the invasion front. Similar calculations were done by Nozaki & Bekki (1983) in their study of periodic wave generation in the complex Ginzburg-Landau equation.

The objective of our paper Dagbovie & Sherratt (2013) is an improved mathematical understanding of dynamical stabilisation. In contrast to Petrovskii and coworkers (2002, 2001), our focus is on the width of the stabilised region once it has become constant, after the initial growth phase. In particular, we present a method that enables calculation of the dependence on parameter values of the width of the stabilised region. Our approach is based on the theory of absolute stability. In Section 3.2, we discuss the notions of absolute and convective stability for spatiotemporal systems, which will be our key tools for determining the extent of dynamical stabilisation in Sections 3.3 and 3.4.

3.2 Convective and Absolute Stability

The phenomenon of "dynamical stabilisation" illustrated in Figure 3.2b, c is an intuitively surprising one: the coexistence steady state is unstable even to spatially homogeneous perturbations and yet it appears as a long term feature of the solution. An understanding of this behaviour requires the theory of convective and absolute stability, which we now summarise. In temporal systems, if a solution is locally stable any small perturbation

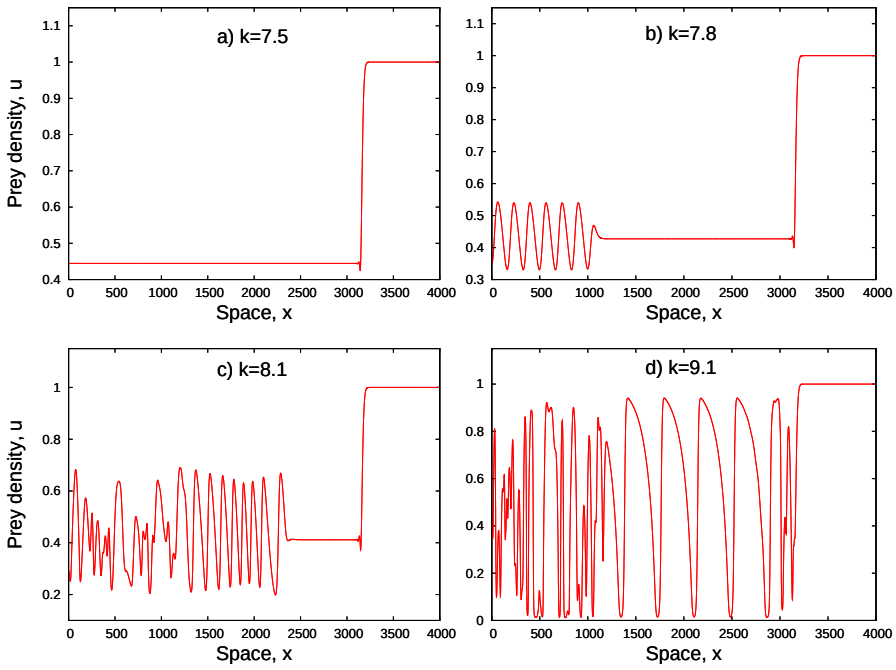

Figure 3.2: Numerical simulations of invasion in (3.1) for four different values of k. Here $b = 3.0$ and the other parameters are given in (3.1e). At time $t = 0$, the unstable steady state $(1, 0)$ is slightly perturbed near $x = 0$. Panel (a) illustrates the structure of a stable solution: it simply consists of an invasion front followed by the coexistence steady state. Panels (b)-(c) show a prey-only region followed by an invasion front, itself followed by a stabilised region which then gives way to oscillations. These plots also suggest that the width of the stabilised region decreases as k increases. For bigger values of k, that region is absent as we can observe in Panel (d). In each case, $x \in (0, 4000)$ and the details of the numerical method were as in Figure 3.1.

decays over time. However, in a spatiotemporal context one must consider also the propagation of growing perturbations. A solution is "convectively unstable" if all unstable linear modes propagate as they grow. By contrast, "absolutely unstable" solutions have stationary unstable linear modes. A more detailed discussion of these concepts is given in Sandstede & Scheel (2000*a*). Our investigation of dynamical stabilisation is based on the absolute stability of the coexistence steady state in a frame of reference moving with an arbitrary velocity V. Therefore we rewrite (3.1) as

$$u_t = D_u u_{zz} + V u_z + f(u, v) \tag{3.2a}$$

$$v_t = D_v v_{zz} + V v_z + g(u, v) \tag{3.2b}$$

where $z = x - Vt$.

We now summarise a numerical method for calculating whether the coexistence equilibrium (u^*, v^*) of (3.2) is absolutely stable; the method is discussed at greater length by Rademacher et al. (2007). The first step is to compute the equations satisfied by small perturbations to the steady state (u^*, v^*). We obtain these by linearising (3.2) about (u^*, v^*). We look for solutions of the form

$$(u, v) = (u^*, v^*) + (\bar{u}, \bar{v})e^{\lambda t + \nu z} \tag{3.3}$$

where λ is the temporal eigenvalue and ν is the corresponding spatial eigenvalue ($\lambda,\ \nu \in \mathbb{C}$); $\bar{u}$ and $\bar{v}$ are complex valued constants. Substituting (3.3) into (3.2) and neglecting terms that are nonlinear in $\bar{u}$ and $\bar{v}$ gives

$$A(\lambda, \nu)y = 0 \tag{3.4}$$

where

$$A(\lambda, \nu) = \begin{pmatrix} D_u\nu^2 + V\nu + \left.\dfrac{\partial f}{\partial u}\right|_{(u^*,v^*)} - \lambda & \left.\dfrac{\partial f}{\partial v}\right|_{(u^*,v^*)} \\ \left.\dfrac{\partial g}{\partial u}\right|_{(u^*,v^*)} & D_v\nu^2 + V\nu + \left.\dfrac{\partial g}{\partial v}\right|_{(u^*,v^*)} - \lambda \end{pmatrix}$$

$$\text{and } y = \begin{pmatrix} \bar{u} \\ \bar{v} \end{pmatrix}$$

The dispersion relation $\mathcal{D}(\lambda, \nu) = \det[A(\lambda, \nu)]$ must be zero for non-trivial solutions. For fixed λ, $\mathcal{D}$ is a fourth order polynomial in ν and we denote its four roots by $\nu_1(\lambda)$, $\nu_2(\lambda)$, $\nu_3(\lambda)$ and $\nu_4(\lambda)$, repeated with multiplicity and indexed such that

$$Re(\nu_1) \geq Re(\nu_2) \geq Re(\nu_3) \geq Re(\nu_4).$$

Then the "absolute spectrum" of (u^*, v^*) is $\Sigma_{abs} = \{\lambda \big| Re[\nu_2(\lambda)] = Re[\nu_3(\lambda)]\}$, and (u^*, v^*) is absolutely stable if and only if Σ_{abs} only contains eigenvalues with negative real part (Sandstede & Scheel 2000*a*).

The larger set $\{\lambda | Re[\nu_i(\lambda)] = Re[\nu_j(\lambda)]$, for some $i \neq j\}$ is known as the "generalised absolute spectrum" (Rademacher et al. 2007). We calculate the absolute spectrum using the method of Rademacher et al. (2007) which involves first calculating the entire generalised absolute spectrum and then determining which parts of it form the absolute spectrum.

Calculation of the Generalised Absolute Spectrum To calculate the generalised absolute spectrum, we first compute the pairs (λ_*, ν_*) that solve

$$\mathcal{D}(\lambda, \nu) = 0 \tag{3.5a}$$

$$\partial_\nu \mathcal{D}(\lambda, \nu) = 0; \tag{3.5b}$$

these are known as branch points. Note that ν_* is a repeated root of $\mathcal{D}(\lambda_*, \nu) = 0$ and therefore any branch point is in the generalised absolute spectrum. The approach in Rademacher et al. (2007) is to calculate the generalised absolute spectrum by continuing it numerically using the branch points as starting points. General theory (Rademacher et al. 2007) implies that the generalised absolute spectrum is a union of connected components, each of which emanates from a branch point. Therefore this numerical continuation procedure calculates the whole generalised absolute spectrum, and the part of this that is absolute spectrum can be determined by monitoring all four roots for ν at each point. Full details of this numerical approach and its practical implementation are given in Rademacher et al. (2007), Smith et al. (2009).

Figures 3.3-3.5 show examples of generalised absolute spectra, calculated in this way. A key feature of these plots is that the most unstable points of the absolute spectrum are branch points. This property has been proved for some simpler equations (Smith et al. 2009), although it does not hold in general: there are some equations for which the absolute spectrum extends to the right of the most unstable branch point (Rademacher et al. 2007). Our study of dynamical stabilisation will depend fundamentally on the most unstable point in the absolute spectrum. Therefore we calculated the absolute spectrum of (3.2) for a range of values of k and V. In every case, the most unstable points in the absolute spectrum were branch points, and in our subsequent calculations we will assume that this property holds. Calculations of the most unstable points in the absolute spectrum then reduces to a straightforward solution of polynomials. Elimination of λ from (3.5a) and (3.5b) gives a sixth order polynomial in ν. For each of the six roots, we calculate the corresponding λ. We then substitute this λ value back into $\mathcal{D}(\lambda, \nu) = 0$, giving a quartic polynomial for ν. Two of the roots of this quartic will be the repeated root for ν that has already been calculated; a comparison of the real parts of this repeated root and the real parts of the other two roots enables us to determine whether or not the repeated roots are ν_2 and ν_3, which is the condition for the branch point to be in the absolute spectrum.

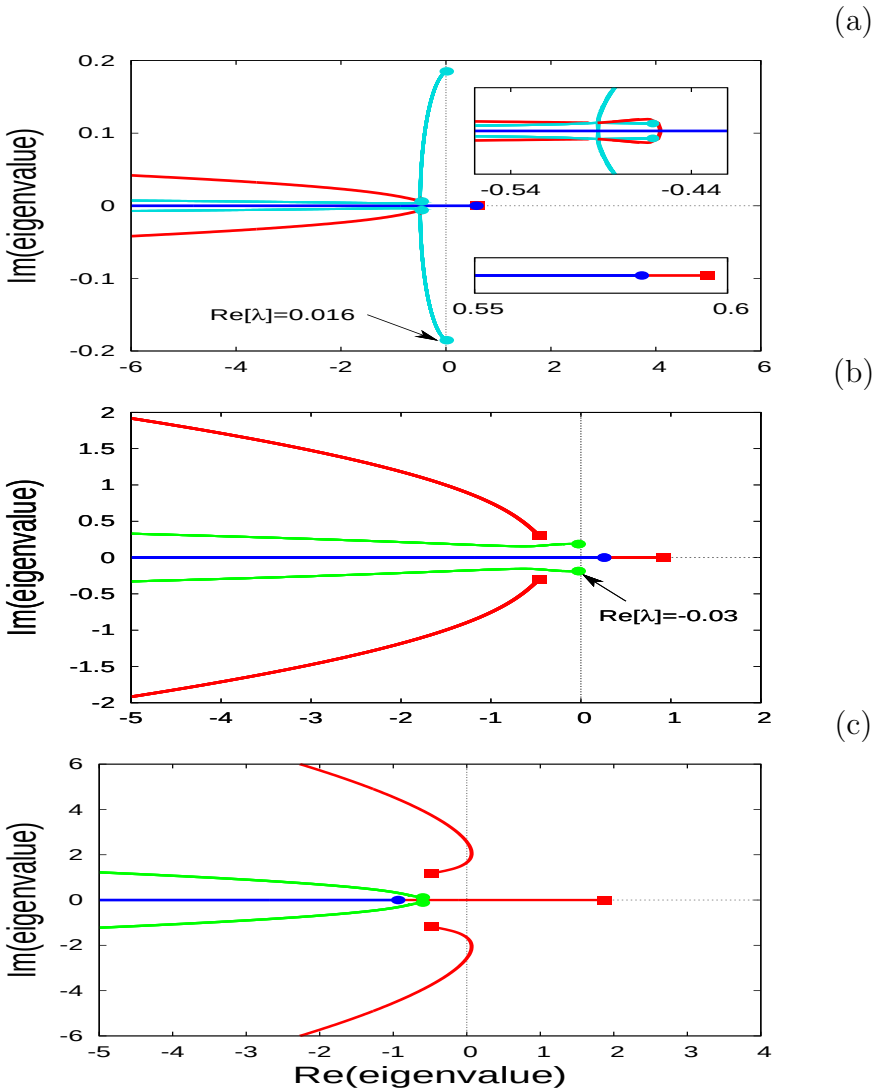

Figure 3.3: Illustrations of the absolute spectrum and generalised absolute spectrum for the Rosenzweig-MacArthur model (3.1). Branch points are indicated by filled circles and filled squares. The value of k is 8 and the values of a, b, D_u and D_v are fixed as in (3.1e). We use $V = 0.01,\ 0.5,\ 2$ on panels $(a), (b)$ and (c) respectively. In green, we plot stable absolute spectra while unstable absolute spectra are represented by cyan curves. The red and blue curves represent the rest of the generalised absolute spectrum. On Panel (a) the λ range is $-0.56 < \mathrm{Re}\,\lambda < -0.42$ and $-0.035 < \mathrm{Im}\,\lambda < 0.035$ on the top insert and $0.55 < \mathrm{Re}\,\lambda < 0.6$ and $-1 < \mathrm{Im}\,\lambda < 1$ on the bottom insert.

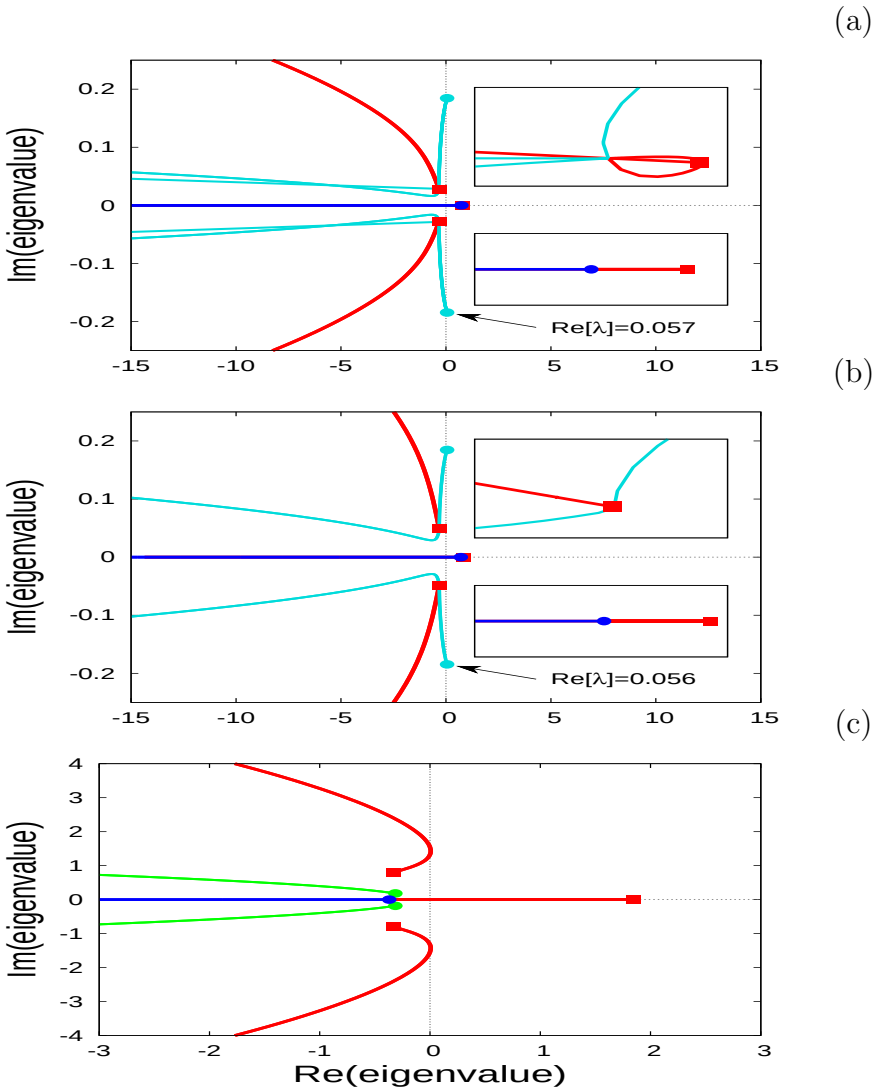

Figure 3.4: Illustrations of the absolute spectrum and generalised absolute spectrum for the Rosenzweig-MacArthur model (3.1). Branch points are indicated by filled circles and filled squares. The value of k is 9 and the values of a, b, D_u and D_v are fixed as in (3.1e). We use $V = 0.05,\ 0.09,\ 1.5$ on panels (a), (b) and (c) respectively. In green, we plot stable absolute spectra while unstable absolute spectra are represented by cyan curves. The red and blue curves represent the rest of the generalised absolute spectrum. On panel (a) the λ range is $-0.35 < \mathrm{Re}\,\lambda < -0.314$ and $0.02 < \mathrm{Im}\,\lambda < 0.05$ on the top insert and $0.65 < \mathrm{Re}\,\lambda < 0.84$ and $-0.01 < \mathrm{Im}\,\lambda < 0.01$ on the bottom insert. On Panel (b) the λ range is $-0.4 < \mathrm{Re}\,\lambda < -0.25$ and $0.03 < \mathrm{Im}\,\lambda < 0.09$ on the top insert and $0.55 < \mathrm{Re}\,\lambda < 0.86$ and $-0.01 < \mathrm{Im}\,\lambda < 0.01$ on the bottom insert.

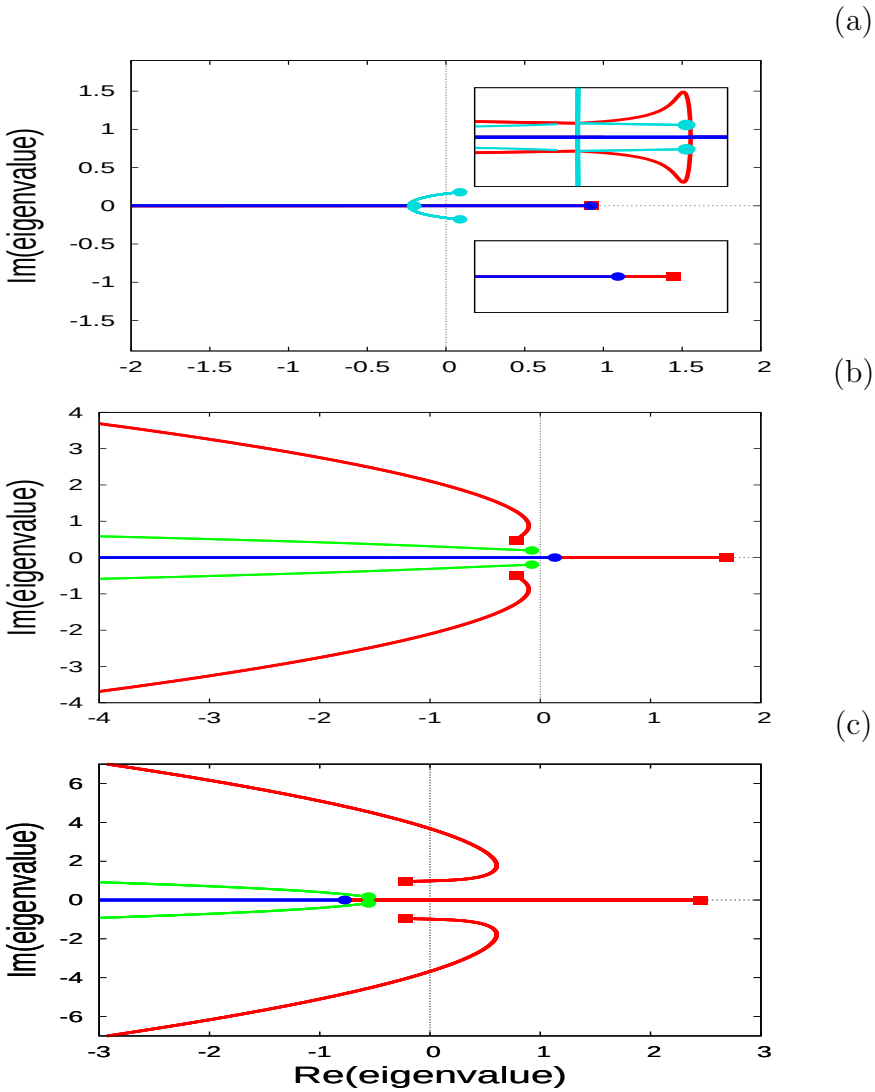

Figure 3.5: Illustrations of the absolute spectrum and generalised absolute spectrum for the Rosenzweig-MacArthur model (3.1). Branch points are indicated by filled circles and filled squares. The value of k is 10 and the values of a, b, D_u and D_v are fixed as in (3.1e). We use $V = 0.001,\ 1,\ 2$ on panels (a), (b) and (c) respectively. In green, we plot stable absolute spectra while unstable absolute spectra are represented by cyan curves. The red and blue curves represent the rest of the generalised absolute spectrum. On Panel (a) the λ range is $-0.269 < \mathrm{Re}\,\lambda < -0.19$ and $-0.02 < \mathrm{Im}\,\lambda < 0.02$ on the top insert and $0.916 < \mathrm{Re}\,\lambda < 0.923$ and $-0.01 < \mathrm{Im}\,\lambda < 0.01$ on the bottom insert.

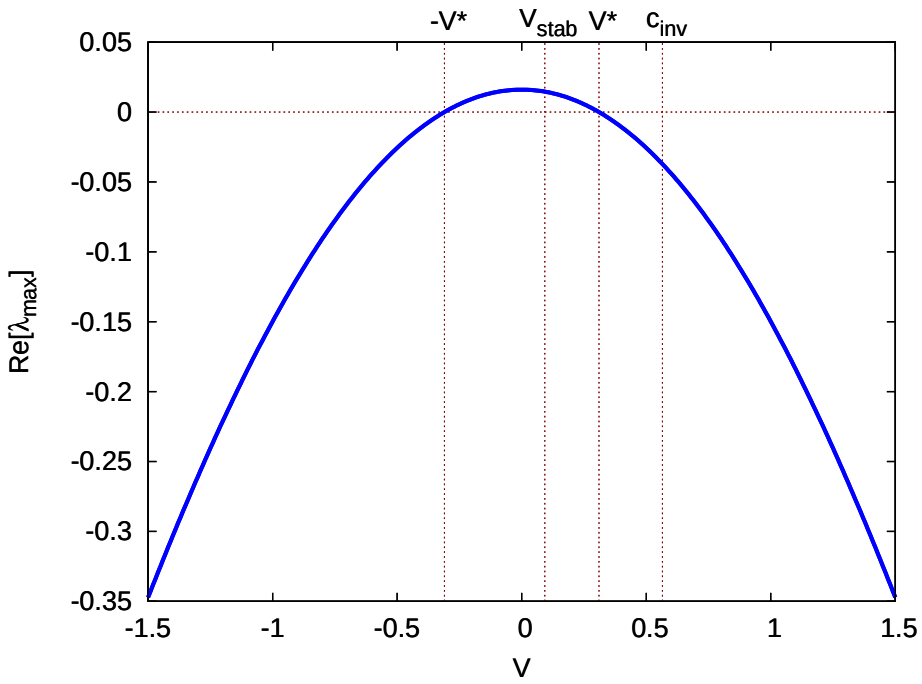

Figure 3.6: Plot of $Re[\lambda_{max}(V)]$, the maximum growth rate of perturbations to the steady state in a frame of reference moving with velocity V, for $b = 3.0,\ k = 8.0$. Here $c_{inv} > V^*$ which means that the invasion front is moving faster than all growing linear modes so that dynamical stabilisation will occur for these parameter values.

3.3 Calculating the Extent of Dynamical Stabilisation

We denote by λ_{max} the most unstable point in the absolute spectrum of (u^*, v^*). Figure 3.6 illustrates $Re[\lambda_{max}]$ as a function of the reference frame velocity V for one value of k; the qualitative form remains the same as k is varied. In particular, $Re[\lambda_{max}] > 0$ on an interval of V values, say $-V^* < V < V^*$, with $Re[\lambda_{max}] < 0$ otherwise. Note that V_L and V_R from the previous chapter are the same as $-V^*$ and V^* respectively. $Re[\lambda_{max}]$ is symmetric about $V = 0$: this is due to the directional symmetry of (3.1). The plot of $Re[\lambda_{max}]$ against V provides the basis for our calculation of the width of the stabilised region. Our arguments follow directly those used to calculate the width of wavetrain bands in Sherratt et al. (2009), Smith & Sherratt (2009), and the description below is deliberately brief. The coexistence steady state that develops immediately behind the invasion front will be perturbed by the front. We make the reasonable assumption that this perturbation contains all unstable linear modes. To understand the subsequent

behaviour of these perturbations, we will visualise the dynamics in the space-time plane (Figure 3.7). We denote by (x^*, t^*) a point on the invasion front. When t increases above t^*, the perturbations applied to the steady state (u^*, v^*) by the invasion front spread out in time and space, growing along all rays $x = x^* + (t - t^*)V$ with V between $-V^*$ and V^*. In order to calculate precisely the width of the stabilised region, we must give a precise definition of its ends. The right-hand end is simply the invasion front, and we define the left-hand end to be the point at which perturbations applied to the steady state (u^*, v^*) by the invasion front first become amplified by a factor $\mathcal{F}$. This occurs at time $t_{crit}(V) = t^* + \log(\mathcal{F})/Re[\lambda_{max}(V)]$, with the corresponding location being $x_{crit}(V) = x^* + V\log(\mathcal{F})/Re[\lambda_{max}(V)]$. Note that $\mathcal{F} > 0$ can be chosen arbitrarily, but we will show that the parameter dependence of the width of the stabilised region is independent of the choice of $\mathcal{F}$. Figure 3.7 shows an example of the curve $(x_{crit}(V), t_{crit}(V))$, $(-V^* < V < V^*)$. The left-hand edge of the stabilised region occurs at the point on this curve that is closest to the invasion front $x = x^* + (t - t^*)c_{inv}$, where c_{inv} is the invasion speed.

A straightforward calculation shows that this closest approach occurs when V satisfies

$$(V - c_{inv})Re[\nu_{max}(V)] = Re[\lambda_{max}(V)], \quad -V^* < V < V^*. \tag{3.6}$$

Numerical calculations indicate that (3.6) has a unique solution for V, which we denote by V_{stab}. Figure 3.10 shows a plot of V_{stab} and V^* as functions of k. The steady state (u^*, v^*) changes stability at $k_{min} \simeq 7.67$ and below this value, V^* and V_{stab} are not defined. As k increases from 7.67, V^* and V_{stab} both increase from zero. Initially $V^* > V_{stab} > 0$ and at $k_{max} = 9.027$, $V^* = V_{stab} = c_{inv}$. For $k > 9.027$, perturbations are able to outrun the invasion front, and there is no stabilised region. Note that the condition $V^* > V_{stab}$ for dynamical stabilisation to occur matches the condition of Petrovskii et al. (2001), which is based on linear spreading speeds, because of the known relationship between spreading speeds and absolute stability (van Saarloos 2003). For $7.67 < k < 9.027$, perturbations travel more slowly than the invasion and dynamical stabilisation occurs (Figure 3.8).

The width of the stabilised region is the spatial distance between the invasion front and $(x_{crit}(V_{stab}), t_{crit}(V_{stab}))$, which can be simplified to

$$\mathcal{L}(k) = \frac{-1}{Re[\nu_{max}(V_{stab})]}\log(\mathcal{F}) \tag{3.7}$$

(see Sherratt et al. (2009) for more details). Of course, this width depends on the arbitrary factor $\mathcal{F}$, but crucially all of the parameter dependence decouples from $\mathcal{F}$ and appears only

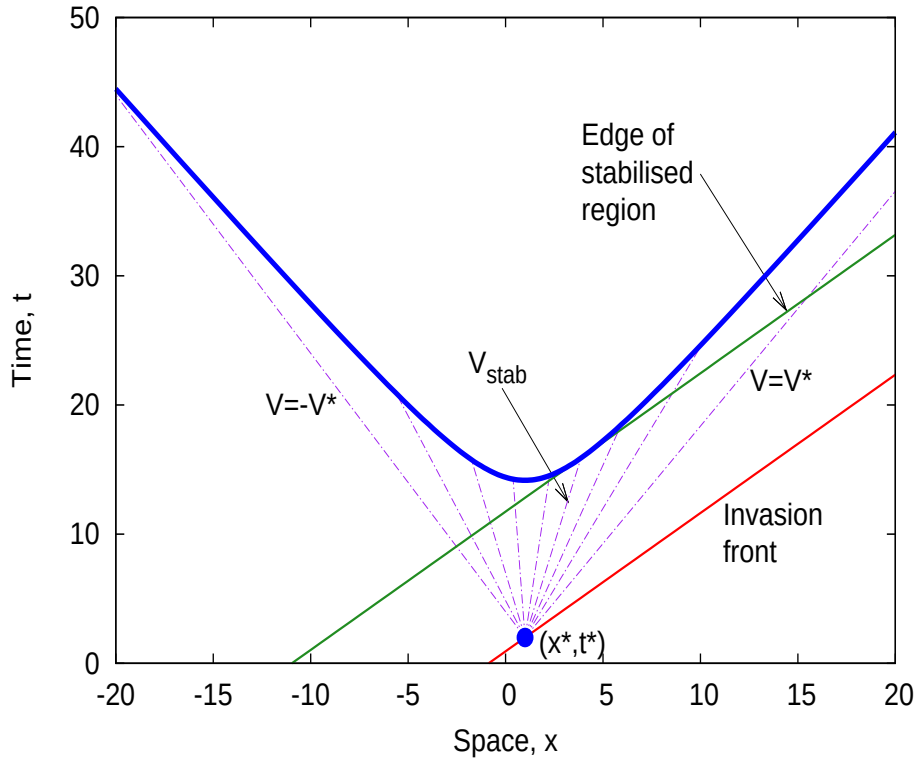

Figure 3.7: An illustration of the argument on which our calculation of the width of the stabilised region is based. The thick solid curve is a plot of calculated values, not a sketch, and the parameters are given by (3.1e) with $b = 1.2$, $k = 9.0$ and $\mathcal{F} = 2$; this value of $\mathcal{F}$ is very much smaller than any suitable real value, but is useful for illustration purposes. Then, if we view the point $(x^*, t^*) = (1, 2)$ in a frame of reference moving at a velocity V, with $-V^* < V < V^*$, perturbations grow and spread out in time and space, reaching the point (x_{crit}, t_{crit}) (thick curve) when their amplitude has doubled. Perturbations moving at the velocity V_{stab} reach the edge of stabilised region closest to the invasion front.

in the coefficient

$$\mathcal{W}(k) = \frac{-1}{Re[\nu_{max}(V_{stab})]}. \tag{3.8}$$

As a test of our theory, we estimated the width $\mathcal{L}(k)$ of the stabilised region for a number of different values of k in numerical simulations of invasion in (3.1), and compared these with the calculated values of $\mathcal{W}(k)$. To estimate $\mathcal{L}(k)$ in simulations, we need to determine the left- and right-hand edges of the stabilised region. Keeping in mind that the left-hand end is the first point behind the stabilised region, we define it as the point x_1 at which $\mathcal{A} = \sqrt{(u-u^*)^2 + (v-v^*)^2}$ equals a small value, taken as 0.005. We choose the right-hand edge to be the point x_2 on the invasion front that is halfway between

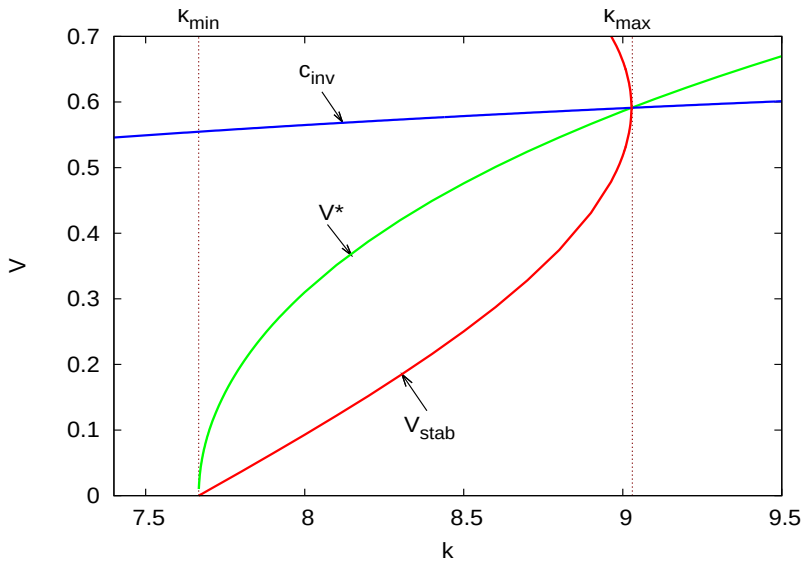

Figure 3.8: Plots of V^*, V_{stab} and c_{inv} against k for $b = 3.0$; a, D_u, D_v are given by (3.1e). At $k = k_{min}$, the coexistence steady state becomes unstable. This value of k is also characterised by $V^* = V_{stab} = 0$. V^* and V_{stab} increase with k until $k = k_{max}$. For $k \in (k_{min}, k_{max})$, we have $V_{stab} < V^* < c_{inv}$, so that the unstable steady state is dynamically stabilised for these k values. The V_{stab} curve folds at $k = k_{max}$ while intersecting both the V^* and c_{inv} curves. For $k > k_{max}$, the velocity V_{stab} does not exist as Equation (3.6) has no solution. Meanwhile V^* has now become bigger than c_{inv}: there are unstable linear modes that overtake the invasion and dynamical stabilisation will no longer occur.

the coexistence steady state and the prey only steady state; that is the point at which $\mathcal{A} = \frac{1}{2}\sqrt{(1-u^*)^2 + v^{*2}}$. We estimate both x_1 and x_2 by linear interpolation between numerical grid points; of course they are both time-dependent. Now recall that the width of the stabilised region is a function of time and has a growing and then a constant phase. Here is an intuitive reason why this is the case: initially the spatio-temporal oscillations invade the uniform (coexistence) steady state but more slowly than the invasion of the prey-only state, leading to a growing stabilised region. However, the leading front of the invasion by predators generates a perturbation of the coexistence steady state which grows sufficiently large to become visible over a fixed distance. At larger times, this distance is the width of the stabilised region. We calculated the average value of $x_2 - x_1$ over the time interval of $(8000, 11000)$, which is during the constant phase for all the parameter sets we considered. Numerical details are the same as in Figure 3.1 except that we now take a larger domain $(0, 8000)$ and that the time variable varies between 0 and 11000.

Figure 3.9a plots the value of $\mathcal{L}(k)$, estimated in this way, against calculated values

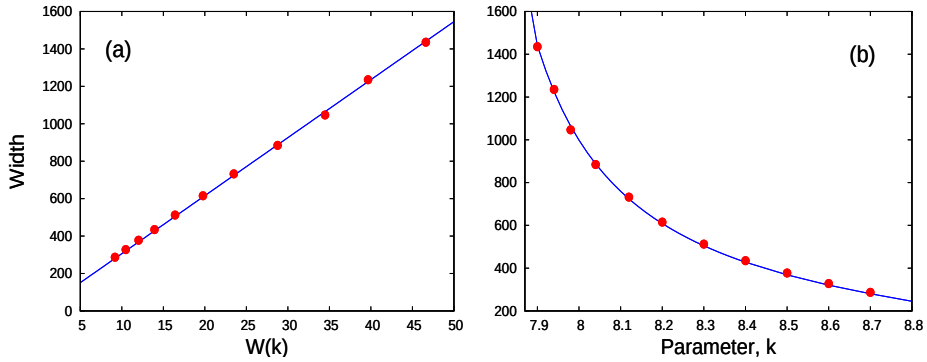

Figure 3.9: (a) plots the numerically calculated width of the stabilised region $\mathcal{L}(k)$ against $\mathcal{W}(k)$ (dots); the straight line is the best fit line, given by linear regression. In (b) we plot our measured width against the parameter $k \in [k_{min}, 8.8]$. The curve shows the calculated width vs k; we obtained the calculated width as a function of $\mathcal{W}(k)$ using the best fit line in (a).

for $\mathcal{W}(k)$. Our theory predicts that these should be linearly related, and this is confirmed by the figure. The slope of the best fit line provides an estimate for $\log(\mathcal{F})$. Note that the best fit line has a small but non-zero (positive) intercept: this corresponds to the edges of the numerically estimated stabilised region being excluded from the theoretical calculations. Combining the best fit line with our formula (3.8) for $\mathcal{W}(k)$, we can predict actual widths of the stabilised region. Figure 3.9b demonstrates the very good comparison between these predictions and the stabilised width measured from simulations, across a wide range of values of k.

3.4 Point-to-Limit Cycle Invasions

For smaller values of b, the behaviour described in Section 3.3 is augmented by an additional complicating factor. To describe this, we consider in detail the case of $b = 1.2$, with k varying and the other parameters given by (3.1e). Calculations as in Section 3.3 show that $k_{max} = 14.56$ (Figure 3.10). However, in numerical simulations, dynamical stabilisation is only observed for k between $k_{min} = 7.67$ and about 10.5; above this, spatiotemporal oscillations occur immediately behind the invasion front (illustrated in Figure 3.11d). Insight into this is given by comparing space-time plots for values of k above the upper limit for dynamical stabilisation, for $b = 3.0$ and $b = 1.2$ (Figure 3.12). In both cases there are spatiotemporal oscillations immediately behind the invasion front. For $b = 3.0$ these are somewhat disordered, and move in the opposite direction to the invasion. However, for

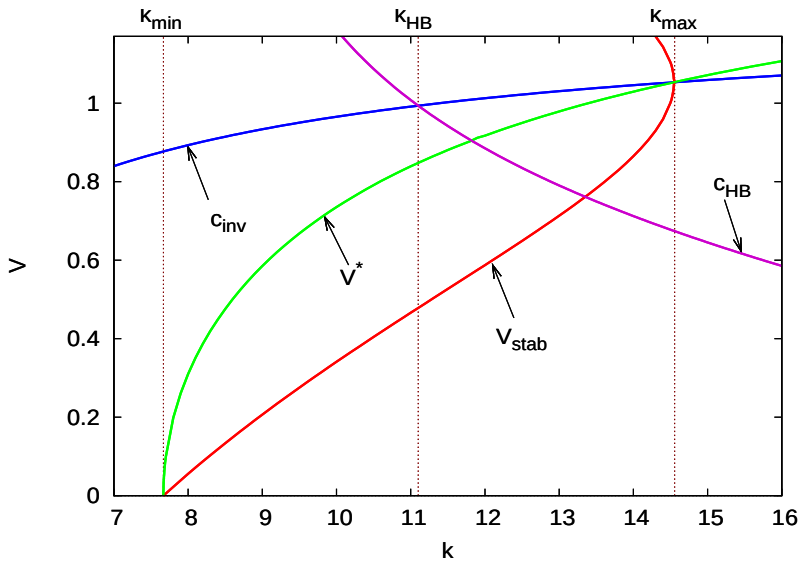

Figure 3.10: Plots of V^*, V_{stab}, c_{HB} and c_{inv} against k for $b = 1.2$. The steady state (u^*, v^*) is unstable for values of k above k_{min}. For k in this range, (u^*, v^*) has a Hopf bifurcation in the travelling wave equation corresponding to (3.1) at a critical value of V. On this picture, we also show c_{HB}, the wave speed at which this Hopf bifurcation occurs, as a function of k. Note that the intersection between the c_{HB} and c_{inv} curves occurs at a value $k_{HB} \simeq 11.1$, which is less than k_{max}.

$b = 1.2$, they have the form of periodic travelling waves moving with the invasion front; further back, there is a transition to more disordered oscillations moving in the opposite direction. Thus for $b = 1.2$, the invasion itself consists of a point-to-periodic orbit connection in the travelling wave ODEs, rather than the heteroclinic connection seen for $b = 3.0$. When the invasion is of the former type, the solution does not approach the coexistence steady state, and thus dynamical stabilisation of this steady state cannot occur.

General theory (Kopell & Howard 1973) implies that in the travelling wave ODEs corresponding to (3.1a-d), for $k > k_{min}$, the coexistence steady state undergoes a Hopf bifurcation as the wave speed $c > 0$ is increased, at $c = c_{HB}$ say. Calculations of the eigenvalues at this steady state show that they all have negative real parts for $c > c_{HB}$, implying that there cannot be an invasion front of heteroclinic connection type, and numerical simulations indicate that there is instead a point-to-limit cycle invasion front. Note that the existence of this type of front solution of (3.1a-d) has been proved in Dunbar (1986) for $D_u = 0$ and in Fraile & Sabina (1989) for $D_u > 0$ sufficiently small. For the case $b = 3.0$ considered in Section 3.3, c_{HB} is significantly greater than c_{inv} for all values of $k \in [k_{min}, k_{max}]$, so that this change in the form of the invasion front does not have any

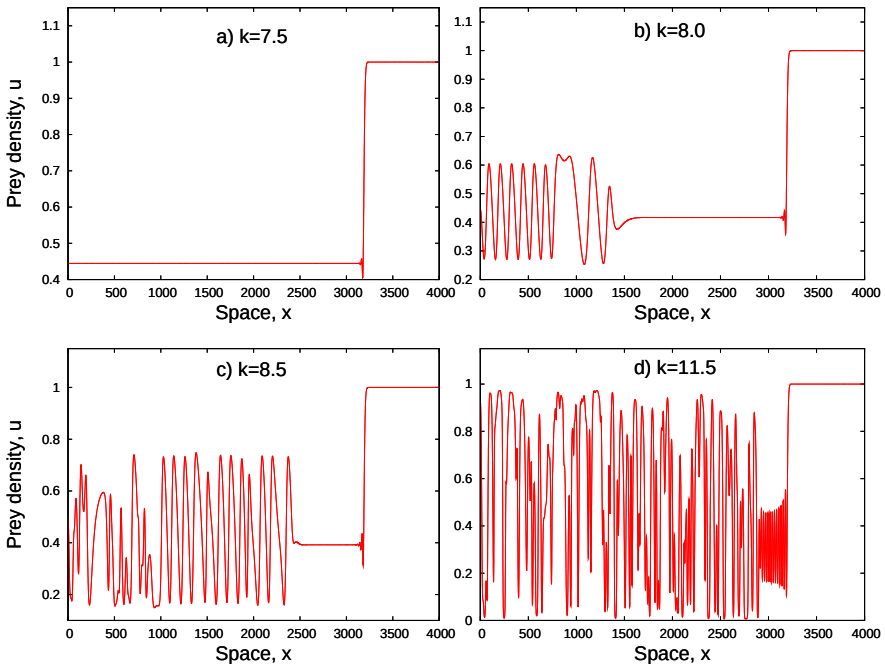

Figure 3.11: Numerical simulations of invasion in (3.1) for $b = 1.2$ and four different values of k. The other parameters are given by (3.1e). Panel (d) corresponds to $k = 11.5$; even though this value is less than k_{max}, there is no dynamical stabilisation. Initial conditions, boundary conditions and the numerical method were as in Figure 3.2.

effect on dynamical stabilisation. However for $b = 1.2$, $c_{HB} < c_{inv}$ for $k > 11.1$ (see Figure 3.10), implying that dynamical stabilisation will only occur for $k_{min} < k < k_{HB} = 11.1$. Here we define by k_{HB} the value of k at which $c_{HB} = c_{inv}$. In fact, as mentioned earlier, we observe stabilisation only up to about $k = 10.5$. A close look at numerical solutions for $k \in (10.5, 11.1)$ reveals that the solution behind the invasion front decays relatively slowly and does not get sufficiently close to the coexistence steady state before giving way to the spatiotemporal oscillations. For values of k in the range $k_{min} < k < 10.5$, there is a very close agreement between the predicted width of the stabilised region, calculated as described in Section 3.3, and the width measured in numerical simulations (Figure 3.13).

3.5 Extension to Other Parameter Values

The main results of Dagbovie & Sherratt (2013) are the determination of the parameter region in which dynamical stabilisation occurs, and of the parameter dependence of the width of the stabilised region. For $k < k_{min}$ the invasion consists of a simple transition

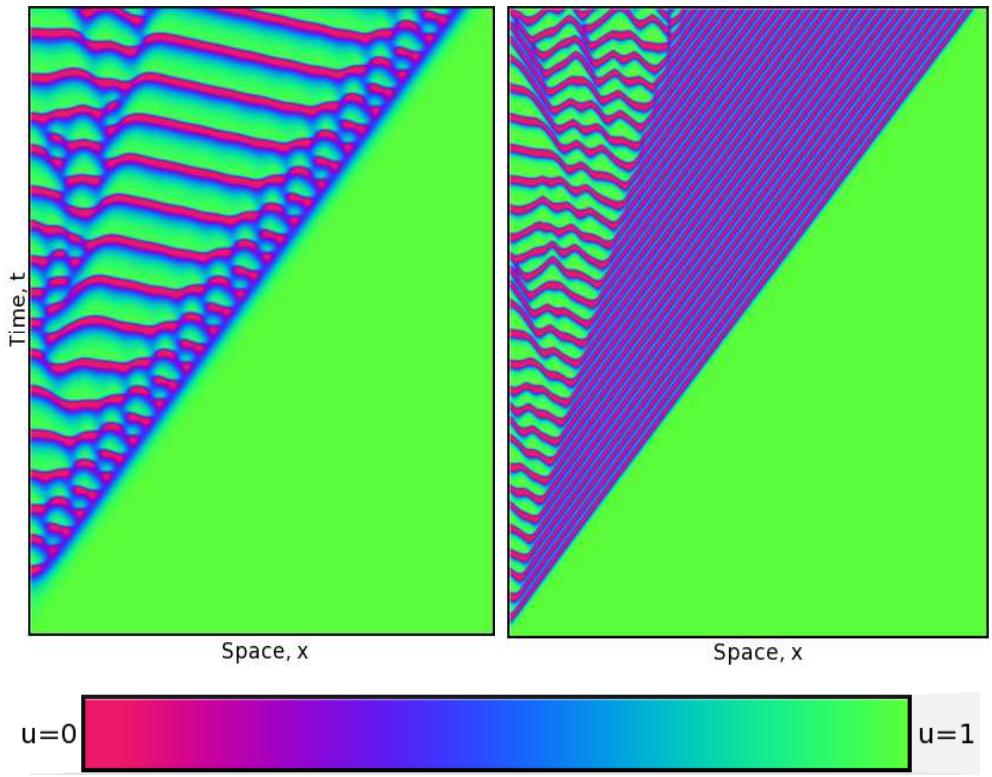

Figure 3.12: Plots of prey densities for $t \in [0, 1070]$ with $x \in [0, 4000]$. The left panel corresponds to $b = 3.0$, $k = 9.5$ and shows that the waves behind the invasion front are moving in a direction opposite to that of the front. However in the right panel ($b = 1.2$, $k = 15$) we see the waves initially moving in the same direction as the front; further back there is a transition to waves moving in the opposite direction. Numerical details are the same for Figure 3.1, and the other parameter values are given by (3.1e).

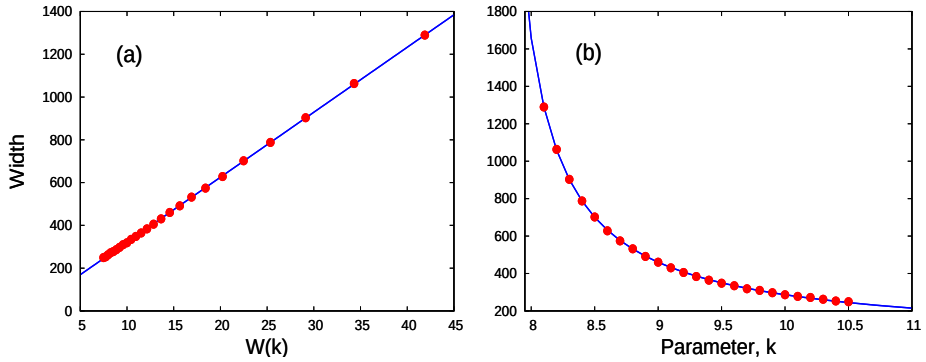

Figure 3.13: (a) The variation in the width $\mathcal{L}(k)$ in numerical simulations of (3.1) with the width coefficient $\mathcal{W}(k)$ (dots); the straight line is the best fit line, given by linear regression. In (b) we plot our measured band width against the parameter $k \in [k_{min}, 10.5]$. The black curve shows the calculated bandwidth vs k.

wave. When $k_{max} < k_{HB}$, dynamical stabilisation occurs for $k \in (k_{min}, k_{max})$; for k just above k_{max} there are spatiotemporal oscillations immediately behind the invasion front, in the opposite direction. When $k_{max} > k_{HB}$, dynamical stabilisation occurs for most of the interval $k_{min} < k < k_{HB}$; it is lost for k just below k_{HB} because of the slow decay behind the invasion front, as discussed in Section 4. For k just above k_{HB} there are spatiotemporal oscillations immediately behind the invasion that move with the same speed and direction as the invasion. Our results indicate that there is a critical value of $b \in (1.2, 3.0)$ at which there is switch between these behaviours. We calculated this critical value by first computing k_{HB} and $c_{HB}(k_{HB}) = c_{inv}(k_{HB})$ for a range of b values; this can be done by numerical continuation of the travelling wave equations. For this grid of b values, we then calculated $V^*(k_{HB})$ using the methods described in Section 3.3; recall that $(-V^*, V^*)$ is the range of velocities for which the coexistence steady state has growing linear modes. Now k_{max} is defined by $V^* = c_{inv}$. Therefore $k_{max} > k_{HB} \Leftrightarrow V^*(k_{HB}) < c_{HB}(k_{HB})$. Figure 3.14a shows a plot of $V^*(k_{HB})$ and $c_{HB}(k_{HB})$ against b; in Figure 3.14b, we see how the upper limit of the extent of dynamical stabilisation varies with b by plotting k_{HB} and k_{max} as functions of b. The curves $c_{HB}(k_{HB})$ and $V^*(k_{HB})$ in Figure 3.14a, and k_{HB} and k_{max} in Figure 3.14b, intersect at the critical value of $b = 1.758$.

Other values of b do not give any behaviour that differs qualitatively from that described for $b = 1.2$ and $b = 3.0$, and the methods that we have presented can be used to determine the occurrence and extent of dynamical stabilisation. As an example, Figure 3.15 illustrates the variation in the width coefficient $\mathcal{W}$, which is proportional to the width of the stabilised region, for $1.2 < b < 2.1$ and $7.8 < k < 8.7$. Dynamical stabilisa-

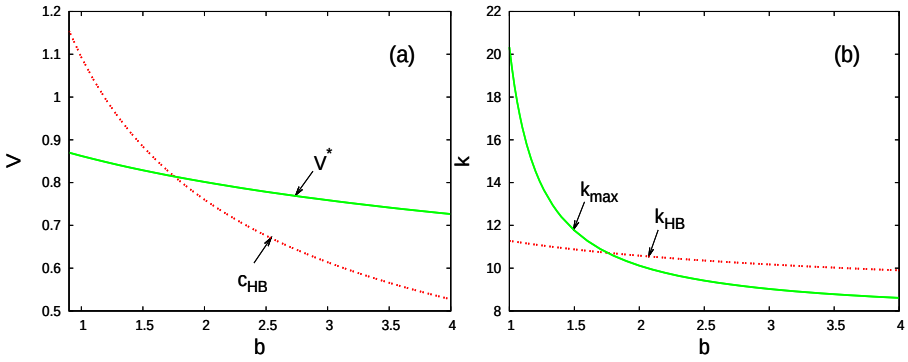

Figure 3.14: Panel (a) shows plots of $c_{HB}(k_{HB})$ (dotted) and $V^*(k_{HB})$ (solid) against b. The two curves intersect at 1.758 as do the curves k_{HB} (dotted) and k_{max} (solid) shown on Panel (b). For values of b below this, $k_{HB} < k_{max}$ implying a point-to-periodic cycle invasion front. However, $k_{HB} > k_{max}$ for $b > 1.758$, meaning that there is a heteroclinic connection behind the invasion front.

tion occurs throughout this parameter region, with no point-to-periodic waves, and the width of the stabilised region is a decreasing function of both b and k.

3.6 Application to Vole-Weasel interactions

As an example application of our approach to a specific ecological system, we consider the invasion of *Microtus* voles by their specialist predator the least weasel (*Mustela nivalis*). Multi-year cycles in the abundance of these voles is a classic and much-studied aspect of the ecology of northern Fennoscandia. The cause of these cycles has been the subject of extensive debate, but a significant volume of data from predator exclusion experiments now points to predation as a leading cause of vole cycling (Korpimäki et al. 2002, Korpimäki & Norrdahl 1998). However it should be noted that vole cycles in other locations, such as Northern UK, appear to result from different mechanisms (Graham & Lambin 2002, Oli 2003, Reynolds et al. 2012).

Parameterisation of the equations (3.1a-d) for the case of the vole-weasel interaction in Northern Fennoscandia is made possible by the large volume of relevant field and laboratory data. The reproductive rate of *Microtus* voles is relatively uniform across different locations in Northern Europe. We take the maximum per capita birth rate to be 3.3 year^{-1}, following Sherratt et al. (2002). This is based on an average litter size of 5, with six litters per season in optimal conditions, and with early-born females breeding themselves in the same season (Dyczkowski & Yalden 1998, Norrdahl & Korpimäki 2002).

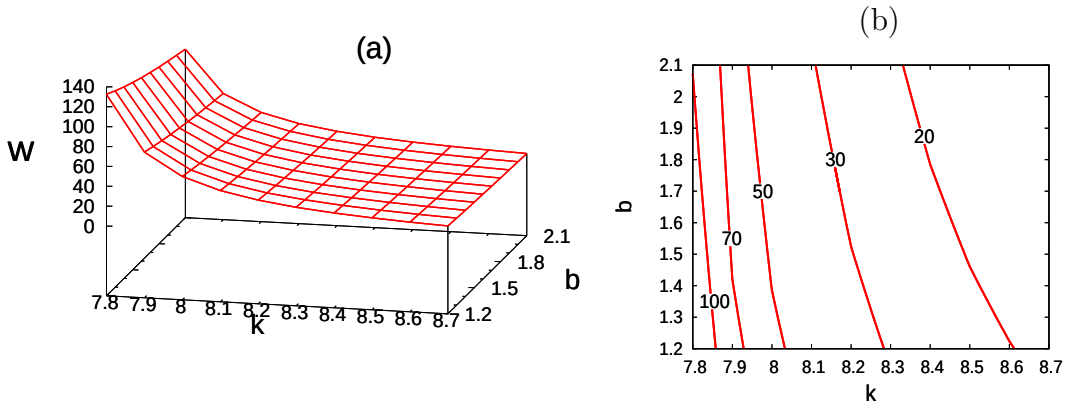

Figure 3.15: On Panel (a), we show a three-dimensional plot of the width coefficient $\mathcal{W}$ as a function of b and k. Featured on Panel (b) are contour plots of $\mathcal{W}$ at levels 20, 30, 50, 70 and 100 in the k, b plane. The plots are based on calculations of $\mathcal{W}$, using the method described in the main text, for $1.2 < b < 2.1$ and $7.8 < k < 8.7$.

However it should be noted that other authors have proposed higher estimates (Turchin & Hanski 1997).

For weasels, the corresponding numbers are a mean litter size of 6, with two litters per season when prey is abundant, and with the females from the first litter breeding themselves in the same season (King 1989, McDonald & Harris 2002). This implies a maximum annual productivity of 30 per adult female weasel, and hence a maximum per capita productivity of 15 year^{-1}. The corresponding per capita birth rate is $\log_e 15 = 2.7\,\text{year}^{-1}$. Annual mortality for weasels is 77.5% (King 1989), implying a mean annual death rate of $-\log_e 0.225 = 1.5\,\text{year}^{-1}$. Using standard nondimensionalisation rescalings for the Rosenzweig-MacArthur model (e.g. Sherratt et al. 2002), these estimates imply $a = 1.8$ and $b = 1.2$. Given these values, the dimensionless parameter k can be estimated based on the amplitude of the vole population cycles. For $a = 1.8$ and $b = 1.2$, the kinetics of (3.1a-d) have a Hopf bifurcation at $k = 3.5$, and the cycle amplitude increases monotonically with k above this value. Field data shows that vole cycle amplitude varies significantly between locations in Northern Fennoscandia (Turchin 2003, §12.2), and we take $k = 4.5$; this implies a ratio of maximum to minimum vole densities of about 21, which is a reasonable representative value.

In comparison with the large volume of data on demographic parameters, there is very limited information on vole dispersal. The mark-capture data of Sherratt et al. (2002) suggests $0.2\,\text{km}^2\text{year}^{-1}$ as a reasonable estimate of the vole diffusion coefficient. For weasels we are not aware of any relevant data, although the diffusion coefficient will

certainly be larger than that for voles. Therefore we varied the dispersal ratio δ (> 1) with $a = 1.8$, $b = 1.2$ and $k = 4.5$ fixed. Figure 3.16a shows that the width of the stabilised region is an increasing function of δ, and that even for the relatively modest estimate $\delta = 2$, the width is significant in comparison to the length scale of typical vole habitats in Northern Europe (10's of km). This implies that the dynamical stabilisation phenomenon would be of major significance in the aftermath of an invasion of *Microtus* voles by least weasels. Figure 3.17a-c show simulations of invasions for δ =2, 5 and 8, which confirm these trends.

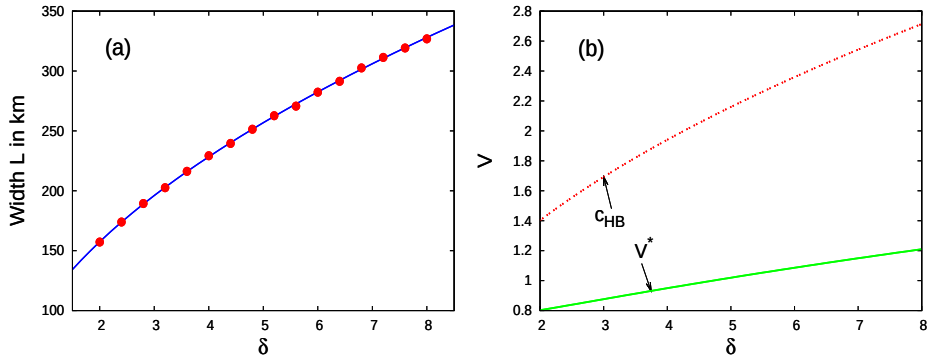

Figure 3.16: Panel (a) plots (in dots) the width $\mathcal{L}$ (in km) of the stabilised region against the dispersal ratio δ with the other ecological parameters fixed as stated in Section 3.6. For each δ in the range $(2, 8)$, we calculated $\mathcal{L}$ in numerical simulations of 3.1 by averaging the widths measured on PDE simulations on the domain $(0, 8000)$ at times between 1000 and 3000 as described in Section 3.3; according to Sherratt et al. (2002), this time range corresponds to a period of 303-909 years after the beginning of invasion. The dimensionless width obtained is then converted into kilometers through multiplication by a factor of 0.246 (see Sherratt et al. 2002). We also calculated the coefficient $\mathcal{W}$ as function of δ then fitting the converted width $\mathcal{L}$ with $\mathcal{W}$ through linear regression, we plotted the obtained expression of the width in terms of $\mathcal{W}$ as a function of δ (straight line). Panel (b) shows c_{HB} and V^* as functions of δ. This indicates that for δ in the range considered, when k rises above $k_{HB}(\delta)$, point-to-periodic invasions occur and there is no stabilised region; for all $\delta \in (2, 8)$, $k_{HB}(\delta)$ is bigger than 4.5, our chosen k value for vole-weasel simulations.

Dynamical stabilisation occurs for all of the values of δ considered in Figures 3.16a and 3.17a-c; in particular there are no point-to-periodic waves. This is confirmed in Figure 3.16b, which shows that c_{HB} is greater than V^* throughout this parameter region. However, this result depends on the value of k, which is expected to vary between geographical locations in view of the observed variations in cycle amplitude. To illustrate this, we show in Figure 3.17d a simulated invasion for $k = 5$, with other parameters as in Figure 3.17c. In this case there is a point-to-periodic invasion, and thus no dynamical

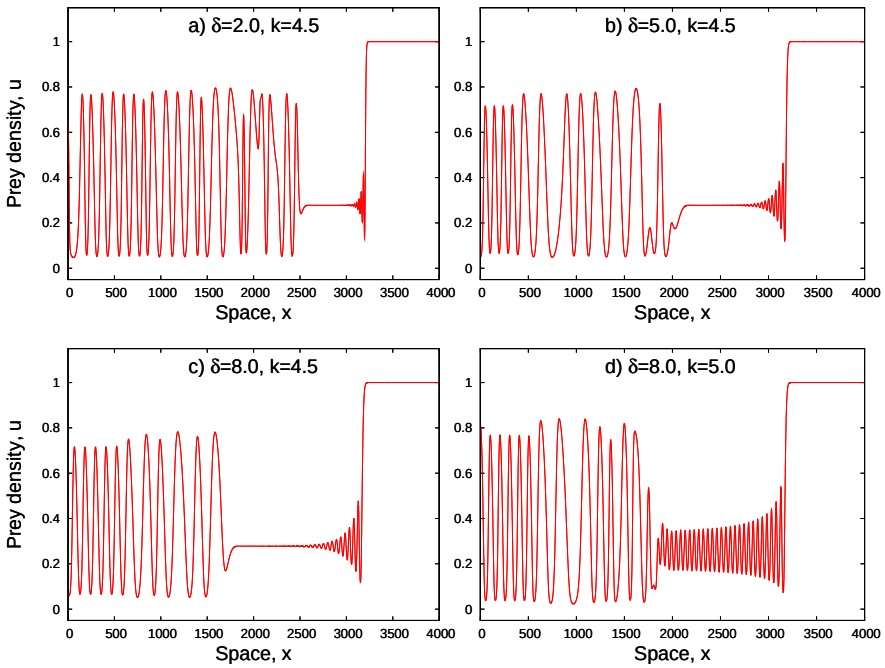

Figure 3.17: PDE simulations for various values of δ. For panels (a)-(c), the parameter k is fixed at 4.5 while δ is respectively 2, 5 and 8. These pictures show that the width of the stabilised region grows with the dispersal ratio δ, as predicted by Figure 3.16a. Panel (d) corresponds to a simulation for $\delta = 8$ with $k = 5$ which is slightly above the upper limit of the extent of stabilisation ($k_{HB} = 4.945$); the slow decay seen on Panel (c) behind the invasion front has now given way to oscillations of relatively bigger amplitude. Initial conditions, boundary conditions and the numerical method are the same as in Figure 3.2.

stabilisation.

3.7 Future Mathematical Challenges

We have focussed on the existence and extent of the coexistence steady state as a spatiotemporal transient. The invasion of a prey population by predators can also involve other spatiotemporal transients. In many cases, periodic travelling waves develop, moving in the opposite direction to the invasion, and in some cases these appear in a moving band (Figure 3.2c, d). Additionally the periodic travelling waves moving with the invasion for $k > k_{HB}$ typically occur in a spatiotemporally transient band (Figures 3.11d and 3.17d). We expect that both of these phenomena could be investigated using the same methodology as in this chapter. However, there is one very fundamental practical difficulty: there is currently no systematic algorithm for computing the absolute spectrum for

a non-constant solution of a partial differential equation. There is no particular difficulty in performing a numerical continuation of the absolute spectrum; the problem lies in the identification of appropriate starting parts (Rademacher et al. 2007). Our work highlights the importance of research on the calculation of the absolute spectrum for non-constant solutions.

Part III

Stability of a Nonhomogeneous Steady State

Chapter 4

Pattern Formation in Arid Landscapes

4.1 Introduction

Vegetation patterns are widespread in semi-deserts. They can be found all over the world (in particular Sub-Saharan Africa, Australia and Mexico) and are detectable through aerial photography. Aerial photographs of arid and semi-arid ecosystems exhibiting these patterns have shown several kilometers square of bare soil with the presence of spots of vegetation; spots are best described as round-shaped groups of vegetation within bare soil. 'Gaps' are another type of patterns and can be considered as the complements of spots as they consist of round-shaped bare soil areas surrounded by vegetated areas (see Figure 4.1). 'Labyrinths' of bare soil alternating with vegetation have also been observed. These patterns can arise on various soil types and many vegetation species, including grasses, shrubs and trees (See Table 2 in Valentin et al. (1999)). One of the most widely reported types of organised vegetation is the 'tiger bush' which is characterised by patterns that seem to mimic the pelt of tiger. It was first described in Niger (Clos-Arceduc 1956) and Sudan (MacFadyan 1950*b*, Worrall 1960).

Spatial patterns on the landscape scale are observed not only in vegetated semi-deserts. They have been noticed in a variety of other ecosystems. Examples include patterns consisting of regular strings in wetland ecosystems in Labrador and Northern Minnesota (Foster et al. 1983), and regular and isolated spots of trees and shrubs in savanna with scarce nutrients (Lejeune et al. 2002, Belsky 1994). In the Wadden Sea, the Netherlands, mussel beds lying on sediments have been found to exhibit regular stripes (Bertness & Grosholz 1985, Wang et al. 2009, Liu et al. 2012). Also in western North America, some alpine trees in the Rocky Mountains are organised in narrow parallel rows perpendicular to the direction of the winter wind. These stripe patterns are called 'ribbon forests' and are the result of the interaction between the wind, the trees and snow accumulation

Figure 4.1: Aerial photograph of a gaped vegetation pattern in the W National Park of Niger. The distance between two neighboring gaps is 50 m in average. *Source Wikipedia.*

(Hiemstra et al. 2002, 2006).

The study of patterned landscapes has attracted the attention of many scientists in recent decades. In fact, human activities have caused soil degradation and a decline in fertility, which tends to promote patterns rather than uniform vegetation. Before the invention of aerial photography, these patterns were often viewed as a type of landscape degradation. However, research on vegetation patterns over the last past years has shed some light on the phenomenon and brought a better understanding of the underlying mechanisms. As a result, changes have been made to the way vegetation patterns are managed (Tongway et al. 2001).

The width of banded patches increases with annual rainfall. For example, regions like Nigeria and Somalia have higher average rainfall and hence wide vegetated patches. These landscapes are seasonal. On the other hand, Jordan and eastern Australia, for example, have lower rainfall and display aseasonal patterns with smaller vegetated patches (Tongway & Ludwig 1990). Furthermore, previous research has shown that vegetation patterns adapt very well to rainfall variation and suggest that the type of pattern could even change as a result of climate change. This research has included both field studies and mathematical modelling. In this study, we will focus on banded vegetation patterns in arid and semi-arid ecosystems. Banded landscapes consist alternating bands of vegetation

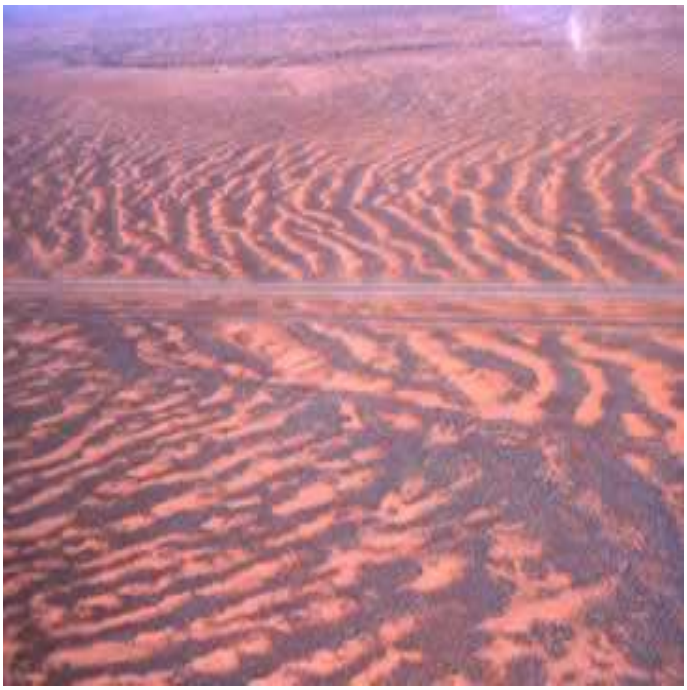

Figure 4.2: Aerial view of a banded vegetation in New South Wales, Australia. This vegetation consists of Mitchell grass, a plant that is mainly found in the North of Australia where summer rainfall is dominant with annual rainfall ranging from 250-550 mm. The plant is very well adapted to these harsh conditions and lives for 20-30 years. The darker pixel on the picture represents vegetation while the lighter pixel shows bare soil and the horizontal line in the middle of the photograph is a road.

and bare ground aligned along the contours in arid and semi-arid regions (50-750 mm rainfall) on very gentle and uniform slopes (0.2-2%). Many mathematical models have been used in the study of this particular type of vegetation patterns. The main ones are those first introduced by Lefever & Lejeune (1997), Klausmeier (1999), HilleRisLambers et al. (2001), Gilad et al. (2007) and have many variants. Recall that Klausmeier's (1999) model was used as an example in Chapter 2. In this study, we will use a variant of the HilleRisLambers et al.' (2001) model introduced by Rietkerk et al. (2002).

The Rietkerk model is an extension of a model first presented in HilleRisLambers et al. (2001) and describes three state variables: plant density P (g/m^2), soil water density W (mm) and surface water density O (mm).

• plant growth is a function of W and will be described by a Holling function of type II. Plant death is proportional to P and plant dispersal is represented by a diffusion term;

• soil water gain occurs through the infiltration of surface water which is a function of surface water and plant density. The rate of this infiltration increases to a maximum as P increases. Soil water loss through water uptake by plants is proportional to plant growth (Holling type II function of P and W). Loss also occurs during evaporation and will be represented through a single term proportional to W. We add diffusion to model water dispersal;

• rainfall provides surface water O which is lost through infiltration into the soil. Surface water flows downhill due to the slope of the soil's surface and this flow is described by an advection term.

Therefore the model consists of the following system of partial differential equations:

$$P_t = D_P P_{xx} + f(P, W, O) \tag{4.1a}$$
$$W_t = D_W W_{xx} + g(P, W, O) \tag{4.1b}$$
$$O_t = \nu O_x + h(P, W, O) \tag{4.1c}$$

with

$$f(P, W, O) = c g_{max} \frac{W}{W + k_1} P - dP,$$
$$g(P, W, O) = \alpha O \frac{P + k_2 W_0}{P + k_2} - g_{max} \frac{W}{W + k_1} P - r_w W,$$
$$h(P, W, O) = R - \alpha O \frac{P + k_2 W_0}{P + k_2}$$

We use the following parameter values:

$$c = 10,\ g_{max} = 0.05,\ k_1 = 5,\ D_p = 0.1,\ \alpha = 0.2,\ k_2 = 5,\ W_0 = 0.2,$$

$$r_w = 0.2,\ D_w = 0.1,\ d = 0.25,\ \nu = 10.$$

All these parameter values except for d are taken directly from (Rietkerk et al. 2002). According to Rietkerk et al. (2002), d ranges between 0 and 0.5. Throughout this study, we fix d at 0.25; the rainfall R on the other hand will be varied. In the remainder of this study, we will study periodic travelling wave solutions of the system (4.1) using the software package `WAVETRAIN` (Sherratt 2012*a*,*b*). In Section 4.2, we briefly discuss simulation results of the model (4.1) and we give a short introduction to `WAVETRAIN` in Section 4.3. Sections 4.4 and 4.6 consist of the investigation in `WAVETRAIN` of the

existence and the stability of pattern solutions, and in Section 4.7, we focus on the effects that rainfall variations have on banded vegetation patterns.

4.2 The Rietkerk Model for Arid Landscapes

The system (4.1) has the following equilibria:

a 'desert' steady state

$$(P_1, W_1, O_1) = (0, R/r_w, R/(\alpha W_0)) \tag{4.2}$$

and a 'vegetated' steady state (P_2, W_2, O_2) where

$$W_2 = \frac{dk_1}{cg_{max} - d},\ P_2 = \frac{R - r_w W_2}{g_{max} W_2}(W_2 + k_1),\ O_2 = \frac{R}{\alpha}\frac{P_2 + k_2}{P_2 + k_2 W_0} \tag{4.3}$$

For $R > 1$ the vegetated steady state is unstable to homogeneous perturbations while the desert steady state is stable. For $R < 1$ the desert steady state is unstable while the vegetated steady state is stable; also $P_2 < 0$ for $R < 1$ so that this state is not ecologically relevant.

The goal of this study is to investigate pattern solutions of the system (4.1). First we explore the existence of banded vegetation pattern solutions of the Rietkerk model in a two-dimensional space. To do this, we rewrite 4.1 to obtain the 2-dimensional Rietkerk model

$$P_t = D_P(P_{xx} + P_{yy}) + f(P, W, O) \tag{4.4a}$$
$$W_t = D_W(W_{xx} + W_{yy}) + g(P, W, O) \tag{4.4b}$$
$$O_t = \nu(O_x + O_y) + h(P, W, O) \tag{4.4c}$$

We then did PDE simulations of (4.4) for $R = 1.05, 1.1, 1.25$ on the domain $0 < x < 500, 0 < y < 500$ using periodic boundary conditions. Our initial solutions were set at the steady state (P_2, W_2, O_2) with a slight perturbation through random numbers no more than 5% of (P_2, W_2, O_2) in amplitude. In all three cases, simulations were run over a period $t = 125000$ and banded vegetation patterns were found (Figure 4.3 left column). These patterns move in the positive x and the positive y directions. We see this in Panel (b) where we compare the solution at $t = 125000$ (left) and the solution at $t = 125400$ (right) for $R = 1.1$. Note that for $R = 1.05$, the patterns obtained at $t = 125000$ are regular (Figure 4.3a) while the patterns for $R = 1.1$ (Figure 4.3b) and $R = 1.25$ (Figure 4.3c) are not. However, with longer run times, we can obtain regular patterns for these

R values too; for example for $R = 1.25$, the PDE solution obtained at $t = 200000$ (Panel (c) right) is more regular than that obtained at $t = 125000$ (Panel (c) left).

In the remainder of this study, we will view banded vegetation patterns as periodic travelling wave solutions; therefore we will be studying periodic travelling wave solutions in the one-dimensional Rietkerk model (4.1). Our main tool in investigating the existence and stability of such solutions is the software package `WAVETRAIN`. This package requires the selection of one of the ecological parameters of the PDE system, and the investigation of periodic travelling wave solutions in `WAVETRAIN` will then be done for various values of this parameter which we call the control parameter. Since in a semi-arid ecosystem, plant density is highly related to annual rainfall, we choose R as our control parameter. Our first step is to perform numerical simulations of (4.1) for various values of R. It has been very useful to do these simulations before starting up in `WAVETRAIN` as they offered an insight into R values at which to expect pattern solutions. These simulations were run on the domain $0 < x < 500$ using periodic boundary conditions at both ends. Starting solutions were set at the steady state (P_2, W_2, O_2) with a slight perturbation through random numbers no more than 5% of (P_2, W_2, O_2) in amplitude. Our computations yielded a periodic travelling wave solution at time $t = 200000$ for $R = 1.05$ and for $R = 1.1$ and $R = 1.25$, periodic travelling wave solutions were found much later at $t = 800000$. We found that pattern solutions exist at $R = 1.05$, $R = 1.1$ and $R = 1.25$ but not at $R \geq 1.28$ and at $R \leq 1$ (note that $P_2 \leq 0$ for $R \leq 1$). Estimates of the wave speed are $c = 0.053$, $c = 0.052$ and $c = 0.039$ and the wavelength was 83.33 in all three cases. These results suggest that pattern solutions exist when the steady state (4.3) is unstable to inhomogeneous perturbations. Figure 4.4 shows a plot, against the space variable x, of the plant density, and the soil and surface water densities found at each of these R values. Having located a few pattern solutions through PDE simulations, we would like to identify the range of (R, c) values for which these patterns exist. To do this, we will need the software tool `WAVETRAIN` that helps calculate these patterns in a more systematic way. First, we give a short introduction on the software in the next section.

4.3 Getting Started with `WAVETRAIN`

A travelling wave solution of (4.1) is any solution of the form $u(x,t) = \tilde{u}(x - ct)$, where c is constant and is called the speed of the wave. Let z denote the variable $x - ct$. Then the existence of periodic travelling waves can be studied using the travelling wave equations which are obtained by substituting the solution forms $P(x,t) = \tilde{P}(z)$, $W(x,t) = \tilde{W}(z)$ and $O(x,t) = \tilde{O}(z)$ into (4.1). The corresponding travelling wave equations are given by

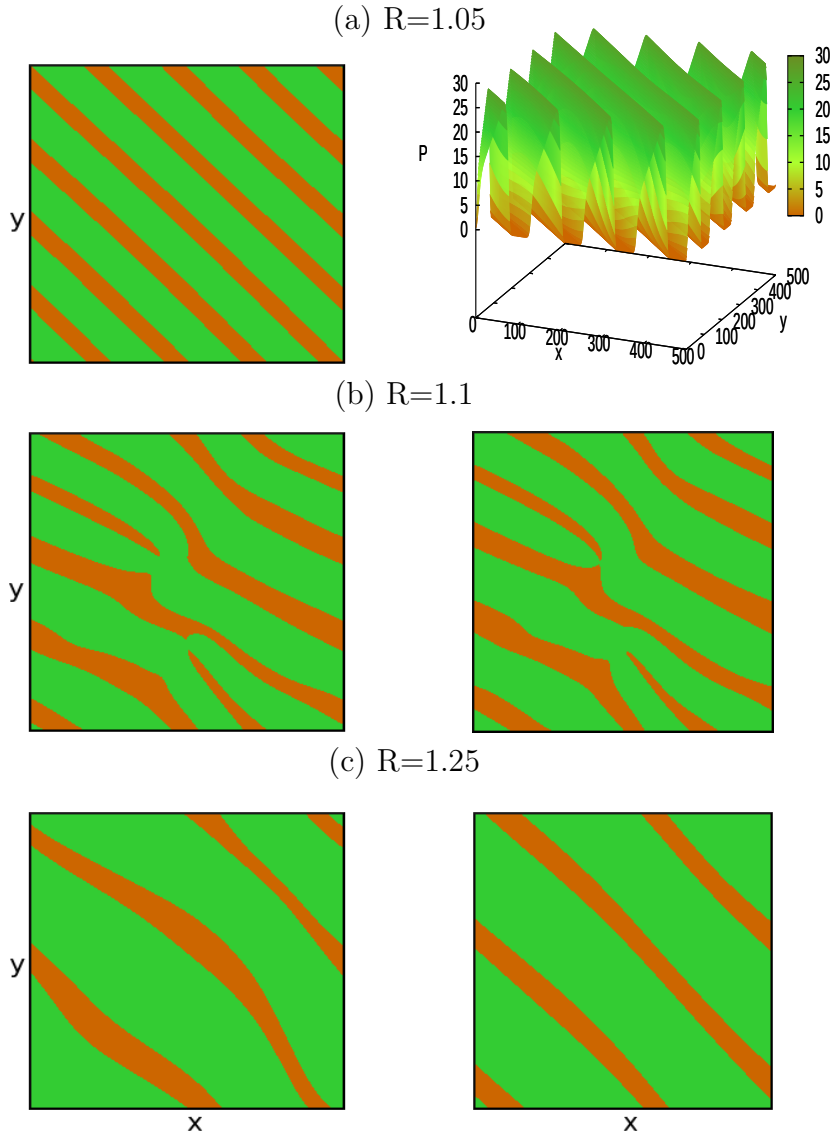

Figure 4.3: Spatial patterns for the rainfall amounts $R = 1.05,\ 1.1,\ 1.25$ on panels (a), (b) and (c) respectively. The domain range is 500×500. Green represents vegetation bands and tan represents bare soil. On the left column of each panel, we show vegetation patterns after $t = 125000$. On the right column of Panel (a) is a 3D plot of the PDE solution at $t = 125000$ for $R = 1.05$. Each of these patterns move in both the positive x and the positive y directions; we see an illustration of this on Panel (b) where we show spatial patterns for $R = 1.1$ after $t = 125000$ (left) and $t = 125400$ (right) respectively. Note that the spatial patterns for $R = 1.05$ exhibit regular stripes. As t is increased above 125000, the patterns for $R = 1.1,\ 1.25$ become more and more regular; compare the solutions for $R = 1.25$ at $t = 125000$ (Panel (c) left) and that at $t = 200000$ (Panel (c) right). Equations (4.4) were solved numerically using a semi-implicit finite difference method with periodic boundary conditions; the grid spacing on both $x-$ and $y-$axis was $dx = dy = 2$ with a time step of $dt = 0.05$ so that the CFL number $2\nu dt/dx$ equals 0.5. The grid points for our starting solutions were set at the steady state (4.3), perturbed randomly by $\pm 5\%$.

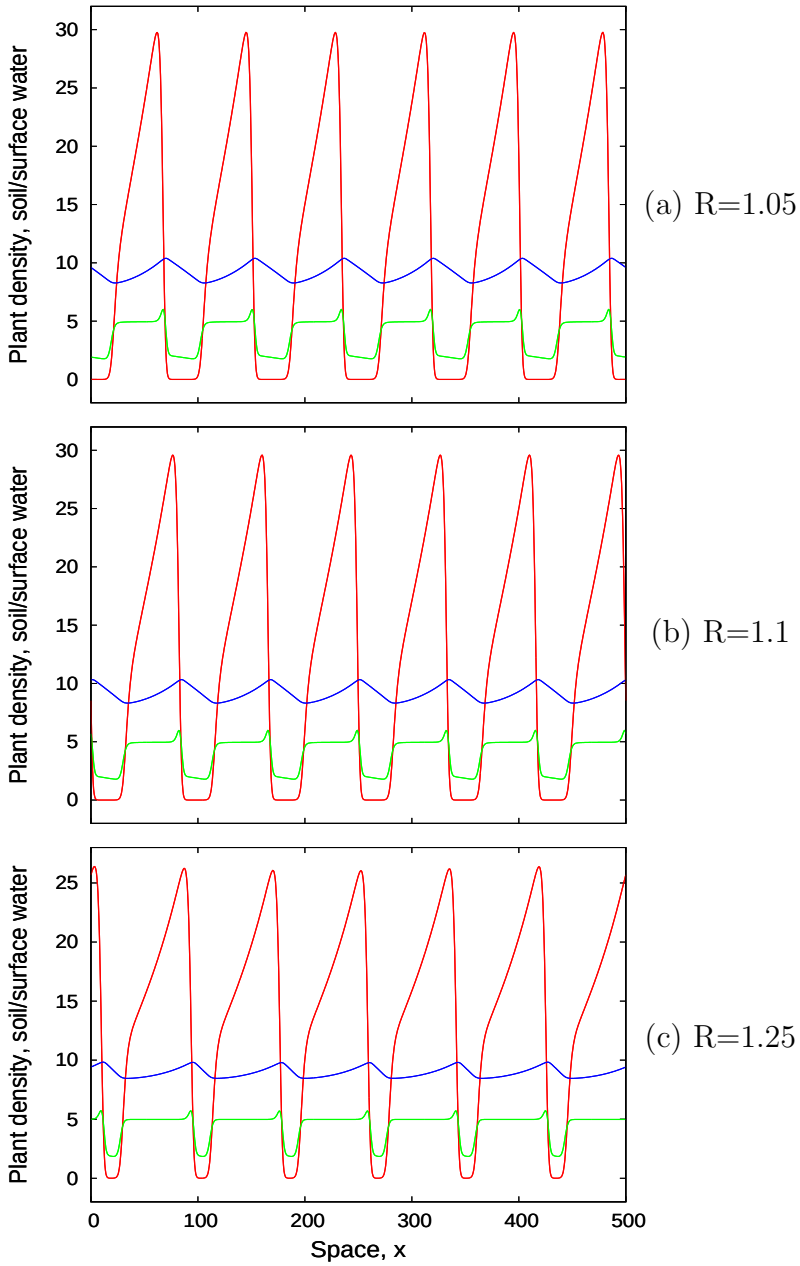

Figure 4.4: Plots against x of periodic travelling wave solutions of (4.1) for $R = 1.05$, 1.1 and 1.25 found through PDE simulations. We plot plant density in red, soil water in green and surface water in blue. These wave solutions show that the vegetation on the domain consists of regions covered with plants alternating with bare soil. As R increases from 1.05 to 1.25, the width of these vegetation bands grows larger and the bare interbands become narrower. The grid points for our starting solutions were set at the steady state (4.3), perturbed randomly by $\pm 5\%$. The system was solved on the domain $0 < x < 500$ for a time range of $t = 200000$ for $R = 1.05$ and of $t = 800000$ for $R = 1.1,\ 1.25$. Estimates of the wave speed are $c = 0.053$, $c = 0.052$ and $c = 0.039$ and the wavelength is 83.33 for all three values. These equations were solved numerically using a semi-implicit finite difference method with periodic boundary conditions at both ends; we chose a grid spacing of $dx = 0.5$ and a time step of $dt = 0.025$ so that the CFL number $\nu dt/dx$ equals 0.5.

the following ODE system:

$$0 = D_P \frac{d^2\tilde{P}}{dz^2} + c\frac{d\tilde{P}}{dz} + f(\tilde{P}, \tilde{W}, \tilde{O}) \tag{4.5a}$$

$$0 = D_W \frac{d^2\tilde{W}}{dz^2} + c\frac{d\tilde{W}}{dz} + g(\tilde{P}, \tilde{W}, \tilde{O}) \tag{4.5b}$$

$$0 = (c+\nu)\frac{d\tilde{O}}{dz} + h(\tilde{P}, \tilde{W}, \tilde{O}). \tag{4.5c}$$

Periodic travelling waves are limit cycle solutions of these equations.

`WAVETRAIN` is a software package for investigating periodic travelling wave solutions of partial differential equations and is freely available for download at `www.ma.hw.ac.uk/wavetrain`. To explore periodic travelling wave solutions for the PDE system (4.1), we enter into `WAVETRAIN` the steady state (4.3) as well as three sets of differential equations:

• the travelling wave equations (4.5). These will be needed for various operations, for instance in locating limit cycles and loci such as a Hopf bifurcation locus or a contour of constant period;

• the linearised partial differential equations. Determining whether a travelling wave solution is stable involves the calculation of the eigenvalue spectrum. The linear partial differential equations given by linearising (4.1) about a periodic travelling wave solution are needed in the first steps of this calculation;

• the eigenfunction equations are another set of equations that `WAVETRAIN` uses during the calculation of the eigenvalue spectrum and they correspond to the periodic travelling wave equations derived from the linearised partial differential equations mentioned above.

`WAVETRAIN` also requires some computational inputs from the user. This includes the number of mesh intervals used for discretisation of periodic travelling waves, eigenfunctions and their derivatives. Another required computational value is the various step sizes used in numerical continuations of loci, spectra, bifurcation diagrams etc.

The user also needs to specify a wave search method for existence and stability calculation of waves. The wave search method specifies the solution branch along which waves should be searched for. There are three different types of wave search method which we will briefly discuss later in Section 4.5. Now, given an (R, c) pair, `WAVETRAIN` can investigate whether the corresponding pattern solution exists. More generally, it also has the ability to investigate whether waves exist in a particular region; to do this the user will

need to define that region through a set of grid points and the software will perform a wave search over this grid investigating each individual grid point. In the next section, we will investigate in WAVETRAIN the existence of pattern solutions of (4.1) for a range of (R, c) values.

4.4 Locating Periodic Travelling Wave Solutions in WAVETRAIN

We find periodic travelling wave solutions of (4.1) by computing limit cycles in the ODEs (4.5). Steady states give birth to small limit cycles in the neighbourhood of a Hopf bifurcation point. Hence intuitively, our starting point for computing limit cycles in WAVETRAIN is to find the locus of Hopf points. Note that this does not mean that the existence of a limit cycle is necessarily related to a Hopf bifurcation point; for example, we show on Figure 4.17 an example of a solution branch starting and ending at homoclinic solutions. Since previous PDE simulations have shown the existence of pattern solutions for $R = 1.05,\ 1.1,$ and 1.25 (Figure 4.4) we use WAVETRAIN to search the range $[1, 1.3]$ for Hopf bifurcation points in the (R, c) plane. Once one such point is found, WAVETRAIN uses numerical continuation to compute the entire locus of Hopf bifurcation points to which the point belongs. We found two loci: one containing Hopf points with $c \leq 0$ and the other containing Hopf points with $c \geq 0$ (see Figure 4.5). Note that the plant steady state P_2, defined in (4.3), is negative for all values of R less than 1; in addition we intuitively expect to find periodic travelling wave solutions with positive wave speed; this is because past research has shown vegetation moving uphill. This can be explained by the fact that plants compete for the space on the uphill side of a vegetation band which has higher moisture. Hence in the remainder of this study, we will focus on the existence and stability of periodic travelling wave solutions that originate from the second Hopf bifurcation locus.

The next step is to choose a domain containing part of (or all of) the Hopf locus through which WAVETRAIN will check for the existence of periodic travelling waves. We then define this domain in the software as a grid of (R,c) parameters. For a better understanding of the existence of periodic travelling wave solutions of (4.1), we start with the relatively small domain $[0.9, 1.3] \times [0.16, 0.7]$ with 21×19 grid points. Because of the numerical cost of this type of search, it is important, before starting a loop through these 399 grid points, to make sure our numerical parameters are suitable; these include values such as the number of intervals used in the discretisation of solutions and the step size used during numerical continuations (see Section 4.3). A natural way to check this is to

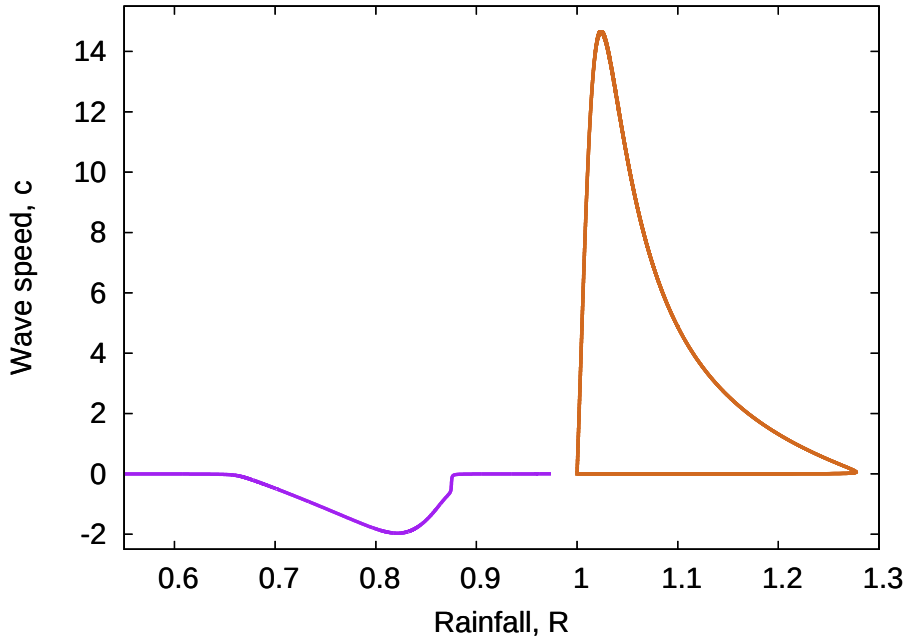

Figure 4.5: Two loci of Hopf bifurcation points computed in `WAVETRAIN`. The first one we found lies below the $c = 0$ axis (purple) and was calculated by doing a Hopf point search in the (R,c) domain $[0, 1] \times [-1, 5]$. A second search of the range $[1, 2] \times [-1, 5]$ yielded the second one (orange) which is above the axis.

confirm the existence of the three periodic travelling waves found previously through our PDE simulations at the (R,c) locations $(1.05, 0.053)$, $(1.1, 0.052)$ and $(1.25, 0.039)$ (see Figure 4.4). We enter these pairs in `WAVETRAIN` and at each of them we found periodic travelling waves of periods approximately equal to 83.333(500/6). See Figure 4.6 for a plot of the periodic travelling wave found at $(1.25, 0.039)$. Note that this solution is very similar to that of the solution in Figure 4.4(c); a slight difference is expected because there will be numerical errors in the calculation of the speed in the simulations used for Figure 4.4(c).

Periodic travelling wave regions

Having confirmed the suitability of our various computational constants, we can now proceed in `WAVETRAIN` by investigating each grid point previously defined on the domain $\mathcal{D} = [0.9, 1.3] \times [0.16, 0.7]$. `WAVETRAIN` loops through the grid and for each corresponding pair of rainfall and wave speed, the search starts at a specified Hopf bifurcation point and follows along the solution branch by numerical continuation, looking for the existence of

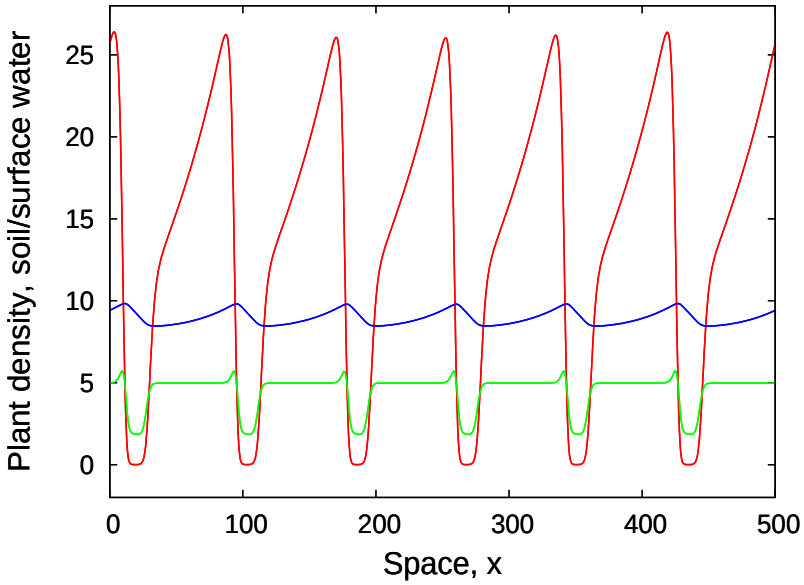

Figure 4.6: A plot of the periodic travelling wave found at $(1.25, 0.039)$ in `WAVETRAIN`. It has a period of 0.8297 which is close to the value of 83.333 previously estimated by simulations of the PDEs (4.1). To be compared with Figure 4.4c.

a wave at the current (R, c) pair. When the search is complete, we can use `WAVETRAIN`'s integrated plotting package to explore the result. The result for our search is shown on Figure 4.7a. Grid points corresponding to parameter values at which a periodic travelling wave has been found are marked with orange dots; `WAVETRAIN` also records the period of the limit cycles located at these points. Notice there are two purple points on the grid. These indicate parameter values (R, c) where a wave solution has not been found even though convergence was successfully reached; this simply means that a periodic travelling wave does not exist at this location. A green dot indicates that the software failed to find a periodic travelling wave at the corresponding coordinates due to the occurrence of a convergence problem during the run. Convergence failures usually occur when the solution branch terminates at a homoclinic solution before the specific (R, c) point has been reached.

Figure 4.7a shows two regions of orange coloured grid points separated by green coloured ones. This suggests that there are two wave regions on our chosen domain $\mathcal{D}$. Assuming this is the case, we can investigate how these regions are bounded. Let Region I denote the upper wave region and Region II, the lower. In theory, such regions are bounded by either a locus of Hopf bifurcation points, a locus of homoclinic solutions or a locus of folds or some combination of the three. This is because Hopf bifurcation points

correspond to limit cycles of zero amplitude; the period grows along the solution branch born at the Hopf bifurcation point. If the period tends to infinity along the branch, the periodic travelling wave tends toward a homoclinic solution. Alternatively the solution may connect two different Hopf bifurcation points. For these reasons, Hopf bifurcation loci and homoclinic solution loci are usual wave boundaries. However, a solution branch that originated from a Hopf point may fold at a certain value of R; hence loci of folds in solution branches can also constitute a boundary between regions of waves. See Figure 4.10 for an example of such folds.

The boundaries of Region II were fairly easy to find. Figure 4.7a shows that it is bounded below by the Hopf bifurcation locus. One advantage in finding the upper boundary was the fact that `WAVETRAIN` recorded the wavelengths of all periodic travelling waves that have been found during the previous wave search loop; this allowed us to quickly notice that the wavelengths for periodic travelling waves near the upper boundary are very large: close to 1000. This suggests that Region II is bounded above by a locus of homoclinic solutions. The way to find a locus of homoclinic solutions in `WAVETRAIN` is to calculate the locus of solutions with a fixed (relatively) big wavelength. These solutions are an approximation to homoclinic solutions. In the case of Region II's upper boundary, we use the contour of period fixed at 1000 as the locus of homoclinic solutions (see Figure 4.7b).

While searching for the lower boundary of Region I, we noticed that this region is characterised by periodic travelling waves of big wavelengths in general; in fact less than 2.5% of the wave solutions in this region have a period less than 1000. This period increases rapidly as R decreases and the highest period we recorded is 35000. Plotting a network of period contours of this region shows that each contour intersect the upper boundary of Region II at a single point. Since Region I is made of an infinite number of such period contours, we take the upper boundary of Region II (homoclinic set) as the lower boundary of Region I. Figure 4.7b shows a few of these loci of homoclinic solutions. Note that only the lower parts of these loci are featured on the plot. This reveals that our chosen domain is too small to investigate the upper boundary of Region I. For this purpose we extend the domain $\mathcal{D}$ to $[0.9, 1.3] \times [-0.5, 15]$ so that the whole locus of Hopf bifurcation points is included, and we notice that Region I is in fact bounded above by the Hopf locus.

Remark In Figure 4.7(a) we see that `WAVETRAIN` failed to find wave solutions at some grid points in Region I. This is because the homoclinic solutions in this region caused convergence failures in `WAVETRAIN`. As we mentioned earlier, for a fixed value of the speed

c, the period of the pattern solutions gets bigger as rainfall R decreases; this explains the fact that more convergence failures occurred for the smaller values of R. The upper region (Region I) contains the majority of the periodic travelling wave solutions we found. See Figure 4.8 for a representation of the proportion that the two regions occupy within the set of all computed periodic travelling solutions.

Folds in the Solution Branch Note that on Figure 4.8, the period contours of values 2000 (blue) and 1400 (green) extend to the right of the Hopf bifurcation locus. This suggests that there is a region of periodic travelling waves at the right hand side of the Hopf locus. This region is very thin and is bounded by the Hopf locus on the left and by a locus of folds on the right. Computing bifurcation diagrams in `WAVETRAIN` for fixed R values and varying c (and vice versa) helps in understanding the location of these folds. See Figure 4.9 for an example of the bifurcation diagram for $c = 0.025$ with varying rainfall. There are two Hopf bifurcation points for that c value. The solution branch shown on Figure 4.9 is the one emanating from the Hopf bifurcation with the largest R value and folds occur several times on this branch. `WAVETRAIN` can be used to compute the locus of folds; one simply enters two pairs of (R, c) values (with either the same R values or the same c values) between which the software will search for a fold and when such a point is found, it is used as a starting point to numerically trace the whole locus of folds. The choice of the (R, c) pairs is made easy by bifurcation diagrams such as that on Figure 4.9. We will discuss the computation of loci of folds further in Section 4.5.

4.5 Wave Search Method

The search in `WAVETRAIN` for a periodic travelling wave for a certain (R_s, c_s) pair can be done in three different ways. The 'direct' method consists of searching for a Hopf point for a range of R values with c fixed at c_s. When such point is found for an R value R_{HP}, a solution branch is traced from (R_{HP}, c_s) to (R_s, c_s). In complicated cases, an 'indirect' method can be helpful. It consists of starting from a certain Hopf point located at (R_i, c_i), and then the solution branch is traced out in two steps: first c is varied from c_i to c_s with R fixed at R_i and then R is varied from R_i to R_s. There is a third method, 'the file' method, where `WAVETRAIN` numerically continues the solution branch starting from a user-specified solution saved into an input file. This method differs from the other two in the fact that it can help compute periodic travelling waves belonging to a solution branch that does not contain a Hopf bifurcation point.

(a)

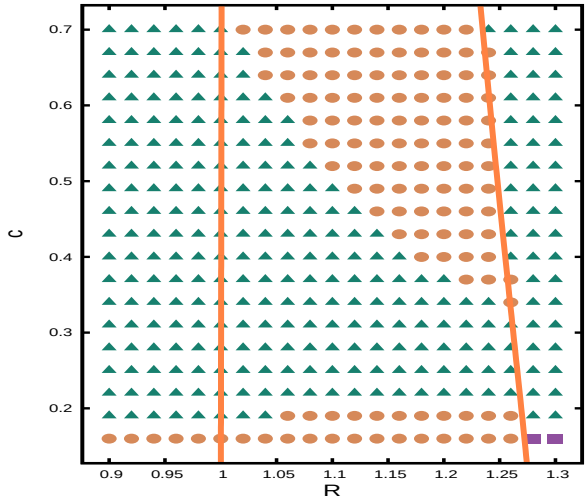

(b)

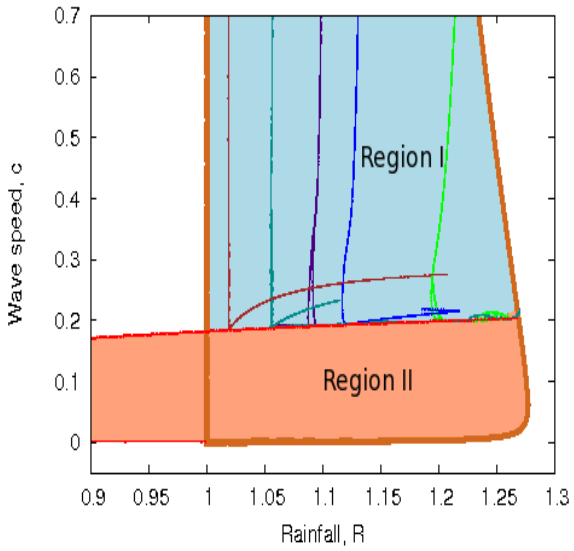

Figure 4.7: Panel (a) shows the sections of the domain $\mathcal{D} = [0.9, 1.3] \times [0.16, 0.7]$ in which periodic travelling wave solutions have been detected. Such solutions are indicated by dark orange grid points. Green indicates that a periodic travelling wave has not been detected at the corresponding location due to a convergence failure. At the few grid points shown in purple, no periodic travelling wave was found even though convergence occurred along the whole solution branch. On both panels, the Hopf bifurcation locus is plotted in orange. Panel (b) shows the actual boundaries of the two wave existence regions. Inside Region I (shown in light blue) we plot a few loci of solutions with large periods; in the increasing R direction, these are the contours of period fixed at 11000, 4000, 2500, 2000 and 1400 respectively. Note that these do not intersect Region II which is bounded by the Hopf bifurcation locus and the contour of period fixed at 1000 (shown in red).

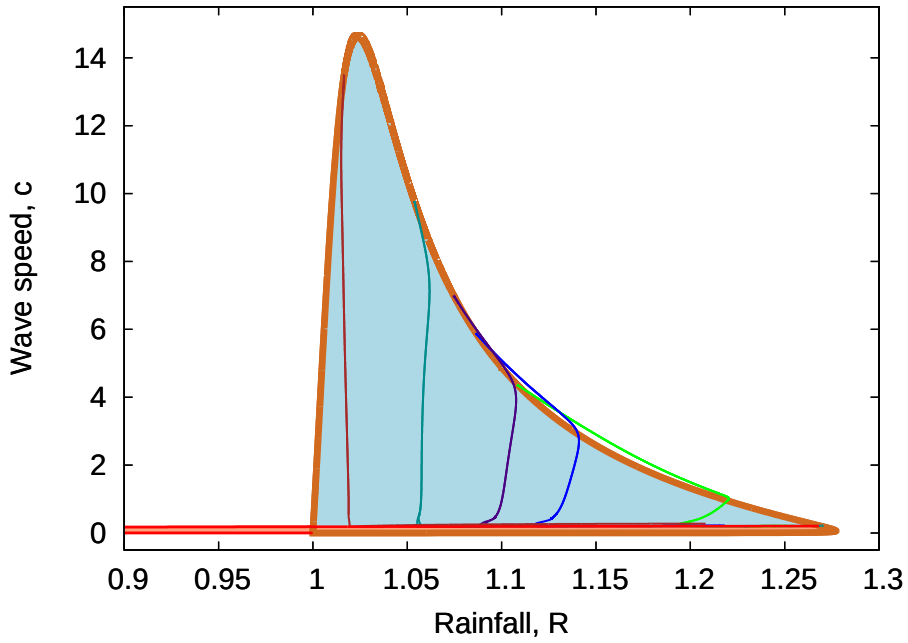

Figure 4.8: Plot of Region II as well as the entire Region I. The latter is bounded above by the Hopf bifurcation locus (plotted in orange). The remaining boundary is the union of the lower part of various contours of (large) fixed period; in the increasing R direction, these are the contours of period fixed at 11000, 4000, 2500, 2000 and 1400 respectively. Region II is bounded by the Hopf bifurcation locus and the contour of period fixed at 1000 (shown in red).

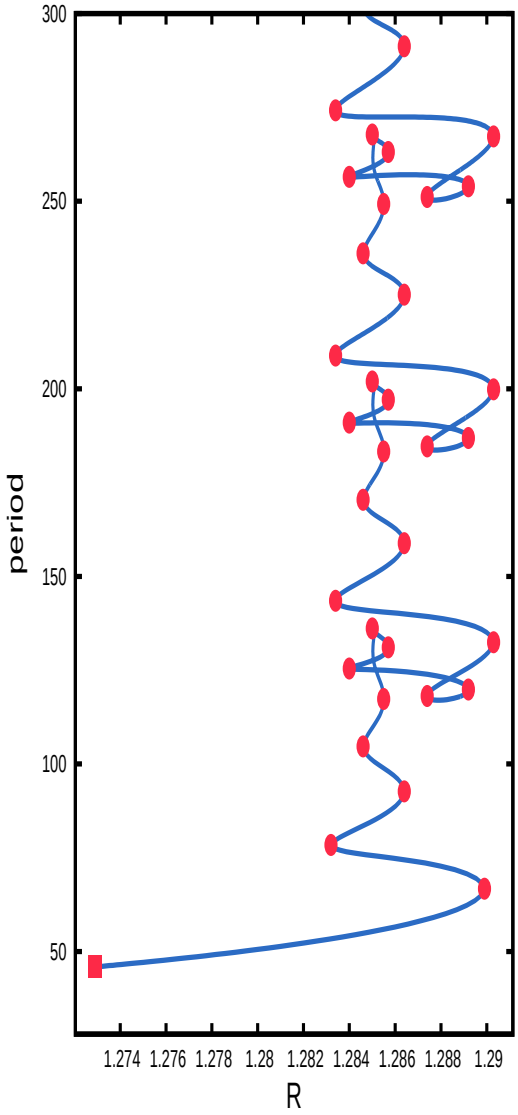

Figure 4.9: Bifurcation diagram for $c = 0.025$; this diagram has been truncated at period= 30 on purpose for better picture quality. The filled red square represents a Hopf bifurcation point while the filled red circles are folds.

4.5.1 Direct method

When we do a stability calculation for a grid representing Region II, waves seem not to exist for some small values of c (Figure 4.14a). Computing bifurcation diagrams for some of those c values reveals that the corresponding solution branches fold multiple times over a thin range of R values at the right of the Hopf bifurcation locus (see Figure 4.10). This explains the absence of periodic travelling waves for $c \in [0.01, 0.04]$ in Figure 4.14a. To overcome this problem, we can use an indirect or a file search method for $c < 0.04$.

The existence of folds in the solution branch means that for some (R,c) pairs, multiple waves will exist. `WAVETRAIN` offers the tools to calculate stability for these multiple waves. In some cases, wave stability changes at the fold. We show an example of this in Figure 4.11. Figure 4.11a shows a plot of the bifurcation diagram for $c = 0.04$; there is a fold in the solution branch such that there are two waves located at $(R, c) = (1.29, 0.04)$. The first one has wavelength 133 and is unstable and the other has wavelength 104 and is stable (see Figure 4.11b for a plot of the respective eigenvalue spectra). The (truncated) bifurcation diagram for $c = 0.02$ shows a solution branch that folds in multiple points (Figure 4.12a); for this value of c and for the rainfall value $R = 1.286$ for example, there are six different waves and stability calculations showed that they are all unstable (Figure 4.12b).

These folds lay at the right of the Hopf bifurcation locus. This means that there exist a thin region of waves at the right of the Hopf bifurcation locus and this region is bounded on the right by a locus of folds. Next we compute this locus using the direct method. To do this, we enter into `WAVETRAIN` to pairs of (R, c) values where either the rainfall values or the wave speed values are the same. The software then searches this range for a fold to use as starting point in the continuation of the locus of folds. Since the solution branches in thin region have several folds, `WAVETRAIN` takes the first fold to occur in the solution branch starting from the Hopf point. Continuation then proceeds, tracing out the locus of folds. See Figure 4.13 for a picture of the fold locus obtained through the direct search. This locus extends between 0.015 and 0.04 on the c-axis. Hence, in order to avoid situations where `WAVETRAIN` fails to find an existing wave (Figure 4.14a), we need to amend the search method for wave speed values between 0.015 and 0.04.

4.5.2 Indirect method

We use the indirect method to compute waves with wave speed between 0.015 and 0.04. Specifically, when computing for waves with speed in this range, we started from the Hopf point located at $(R, c) = (1.1, 0.001)$. Then c is varied while the rainfall stays fixed at 1.1

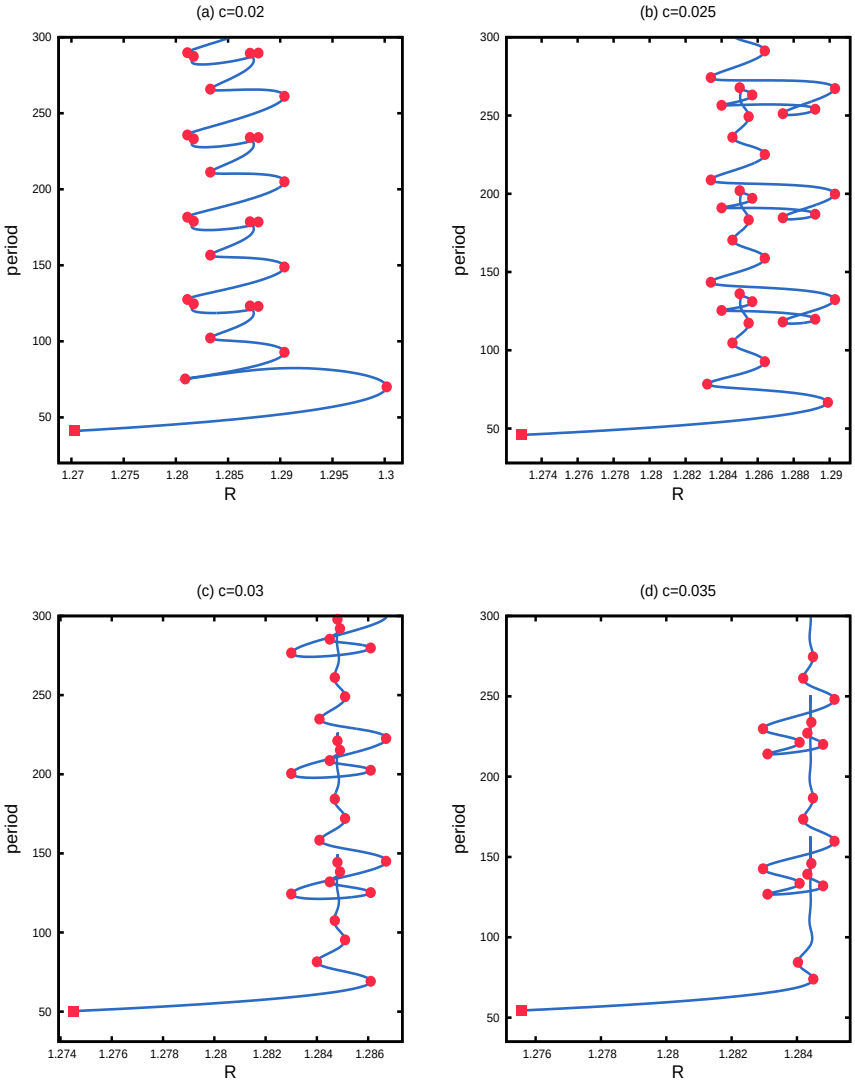

Figure 4.10: Bifurcation diagrams for wave speed values in the range $[0.01, 0.04]$; (a) $c = 0.02$, (b) $c = 0.025$, (c) $c = 0.03$ and (d) $c = 0.035$. These diagrams have been truncated on purpose for better picture quality and we see that the corresponding solution branches fold multiple times over a thin range of R values to the right of the Hopf bifurcation locus. This explains the absence of periodic travelling waves for $c \in [0.01, 0.04]$ in Figure 4.14a. The filled red squares represent Hopf bifurcation points while the filled red circles are folds.

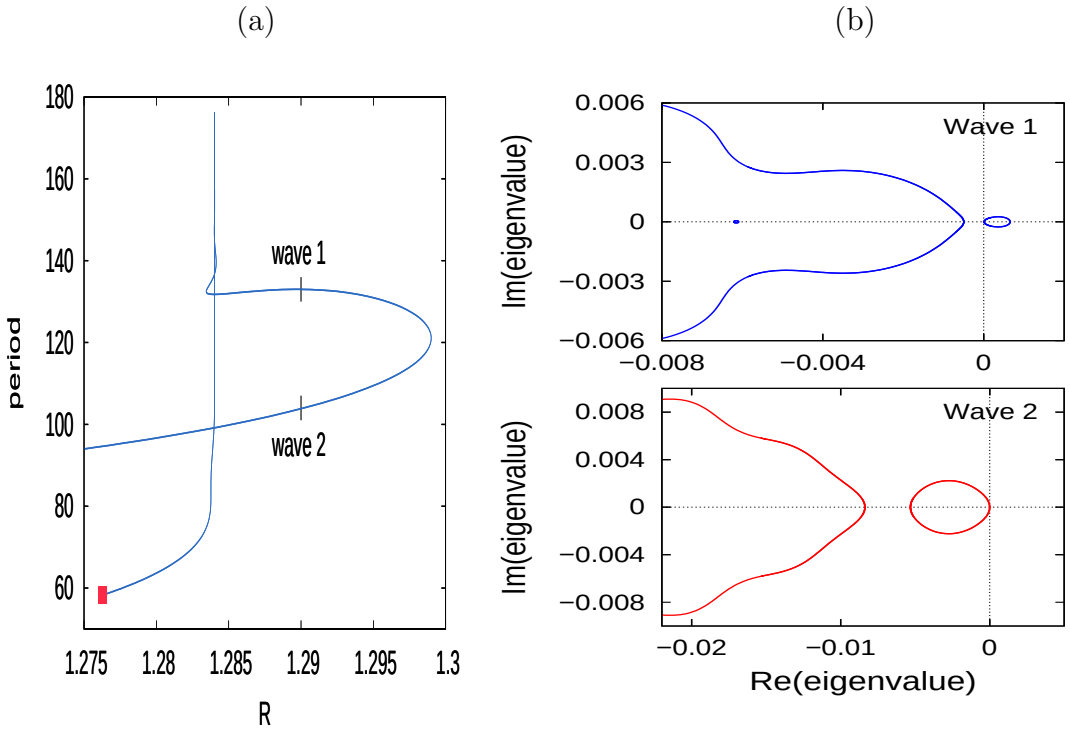

Figure 4.11: Panel (a) shows the bifurcation diagram at $c = 0.04$; the filled red square is a Hopf bifurcation point. There is a fold in the solution branch such that for the rainfall amount $R = 1.29$ for example, there are two different waves, $wave1$ (wavelength = 133) and $wave2$ (wavelength = 104). The eigenvalue spectra of $wave1$ and $wave2$ are shown on Panel (b); the first is unstable (blue curve) while the the second is stable (red curve).

until the required speed is attained. Next, the rainfall will be varied and the search stops when the appropriate R value is reached. This solves the problem of the 'missing waves' seen on Figure 4.14(a). Figure 4.14(b) shows the results of a combination of the direct and indirect methods.

The bifurcation diagram in Figure 4.17c indicates that there is a region of waves at the right of the Hopf bifurcation locus with rainfall value as high as $R = 1.376$. To find the boundary at the right of this region, we attempt to compute the locus of folds using the indirect method. We computed this locus in three different parts due to continuation problems. First, we used the two (R, c) pairs $(1.27, 0.017)$ and $(1.4, 0.017)$ as a search range for the starting solution. `AUTO` found a fold at $(1.317, 0.017)$, and starts tracing out the locus but then drifts away into joining homoclinic solutions. When the wavelength gets increasingly big, it then changes direction but again it ends up computing homoclinic solutions. It is understandable how this 'error' could have occurred: indeed, there are homoclinic solutions in the region where we are performing the fold locus search (see

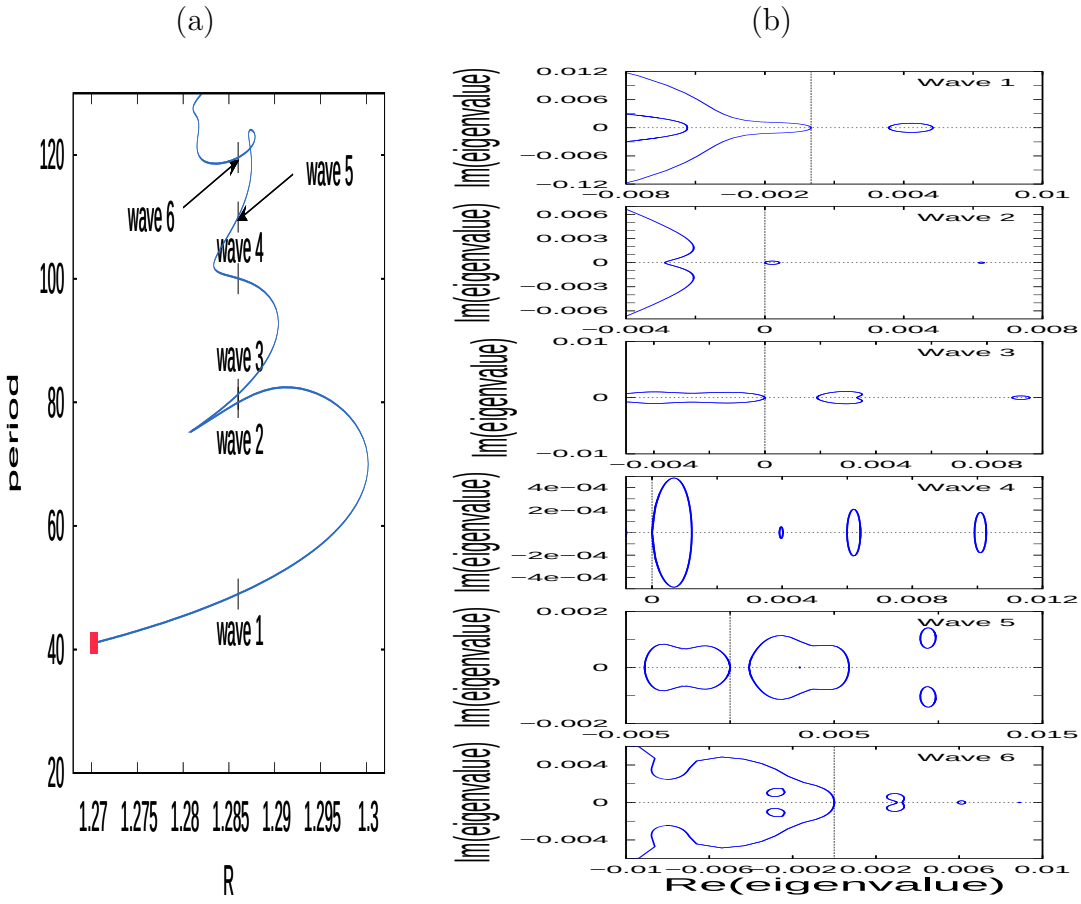

Figure 4.12: Panel (a): bifurcation diagram at $c = 0.02$. We truncated the solution branch to show waves of wavelength between 20 and 130 and in this range, there are six different waves $wave1$, $wave2$, ..., $wave6$ at the R value 1.286. Panel (b): eigenvalue spectra of $wave1$, $wave2$, ..., $wave6$; these spectra indicate that all six waves are unstable.

Figure 4.17c). It is possible that a solution branch containing such homoclinic solutions folds slightly at some point. While continuing the fold locus, `AUTO` might have detected such a point; continuation would have then carried on from that point, thus tracing the locus of homoclinic solutions. The result of this computation is shown by the purple curve on 4.16a. Using the file method described below, we have been able to calculate the set of homoclinic solutions in this wave region and it is similar to this purple curve. A genuine portion of the actual locus of folds we are looking for is included in this curve; to obtain the whole locus, we just need to do two more fold locus searches on either side of the previously obtained portion (green and pink curves on 4.16a). With the three search results, we obtain a connected curved from which we eliminate the homoclinic parts to obtain the locus of folds, which is shown on Figure 4.16b.

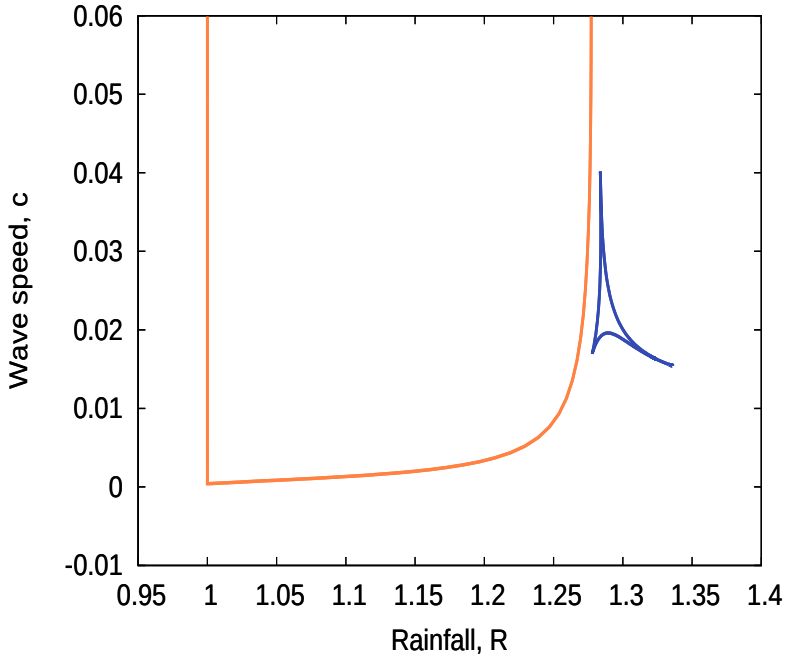

Figure 4.13: Fold locus computed with the direct search method (blue curve). We also show part of the Hopf bifurcation locus (orange curve).

4.5.3 File method

The file method computes solution branches starting from a specified pattern solution. The latter can be a solution obtained from previous PDE simulations or a solution previously computed in `WAVETRAIN`. The advantage with this method is that it can find waves even when a Hopf point has not been found. The search for a bifurcation diagram for $c = 0.02$ using the file method starting with a periodic travelling wave solution at $(R, c) = (1.22, 0.02)$ yields two bifurcation diagrams; one is the same as the diagram on Figure 4.10a (and the same as Figure 4.12) obtained through the direct search. The second one does not contain any Hopf bifurcation point and joins two homoclinic solutions (Figure 4.17).

We have previously seen that there are multiple waves corresponding to the (R, c) value $(1.286, 0.02)$ and we have shown that the first six of these waves along the solution branch are all unstable (Figure 4.12). Taking a close look at Figure 4.17b, we see that there is another periodic travelling wave at $(1.286, 0.02)$ which belongs to the solution branch joining the two homoclinic solutions. We calculate stability for this new wave and found that it is stable. See Figure 4.18 for the eigenvalue spectra of this solution.

(a)

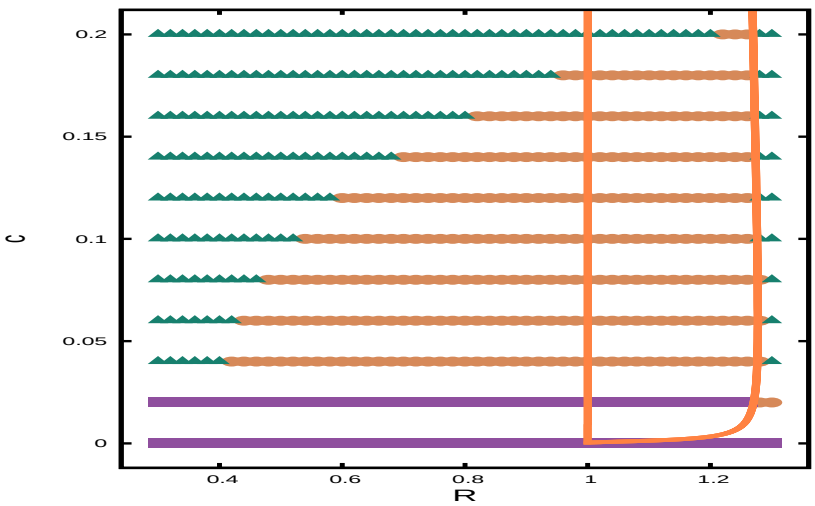

(b)

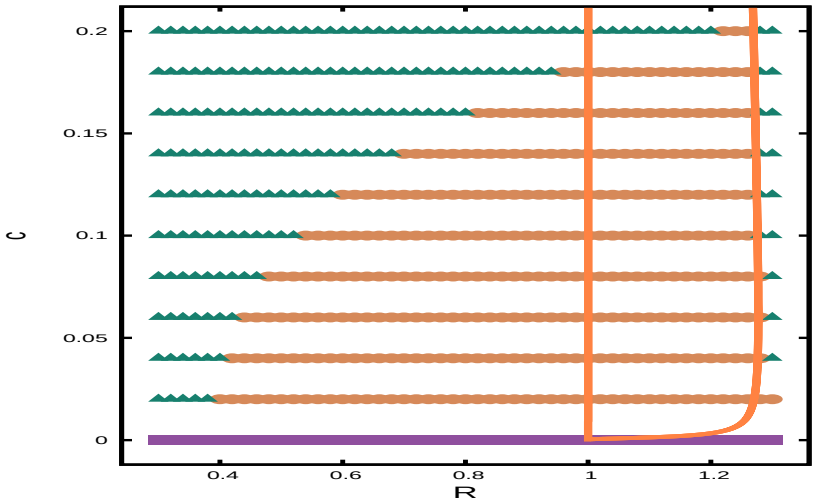

Figure 4.14: Panel (a): a grid of 51×11 points on the domain $[0.3, 1.3] \times [0, 0.2]$ showing results of a wave search run on Region II using the direct method only. The filled dark orange circles indicate the existence of periodic travelling waves at the corresponding (R, c) locations. Green triangles indicate that a periodic travelling wave has not been detected at the corresponding location due to a convergence failure. Purple squares correspond to locations where no periodic travelling wave was found even though convergence occurred along the whole solution branch. `WAVETRAIN` could not find waves around $c = 0.02$ due to the fact that for some values of c below 0.04, the solution branch starts from the Hopf point with the biggest R value and continues into a thin region of waves to the right of this Hopf point (see Figure 4.10). This is fixed on Panel (b) using a combination of both direct and indirect methods: the direct method was used at locations with $c \leq 0.04$ and the indirect method (illustrated in Figure 4.15), elsewhere. A portion of the Hopf bifurcation locus is plotted with a thick orange curve.

(a) Step 1

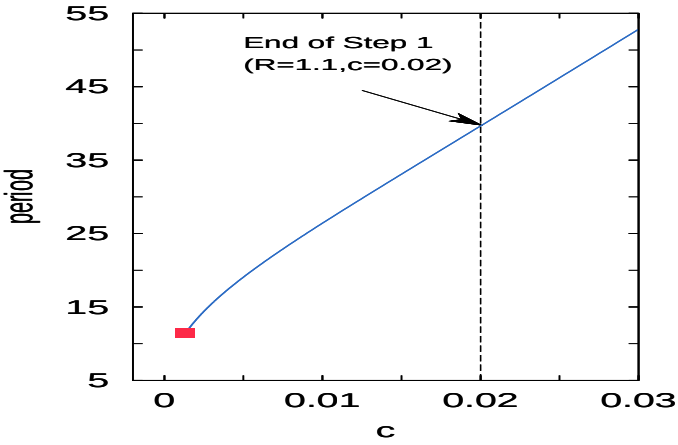

(b) Step 2

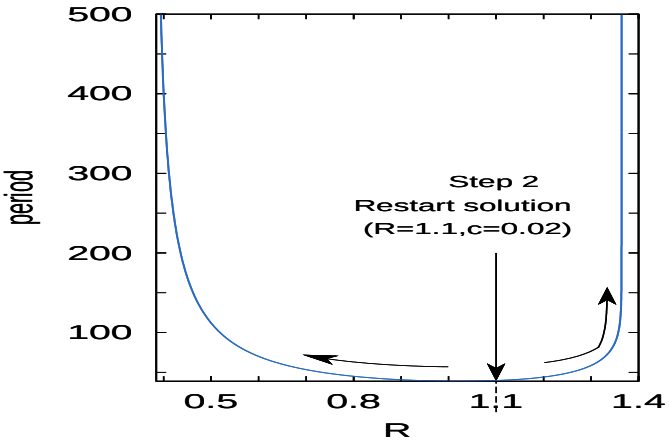

Figure 4.15: Illustration of the indirect wave search method. First, we specify in `WAVETRAIN` a Hopf point to start from; we fix the rainfall value at $R = 1.1$ and choose the Hopf point at $c = 0.001$ as starting point. When searching for a wave of speed $c = 0.02$ and a certain rainfall value R_i with this indirect method, `WAVETRAIN` firstly increases c from 0.001 until it reaches $c = 0.02$ while R is kept constant at 1.1 (Panel (a)). The second step, illustrated by Panel (b), then consist of either increasing or decreasing R starting from 1.1 (see arrows) until the required rainfall value R_i is reached; the search stop at this point.

(a)

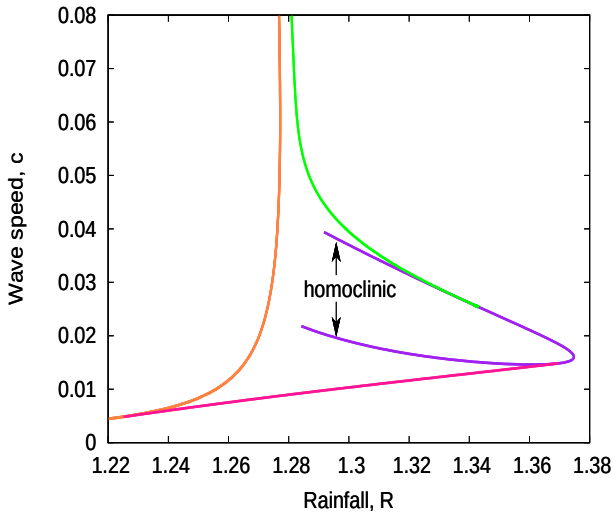

(b)

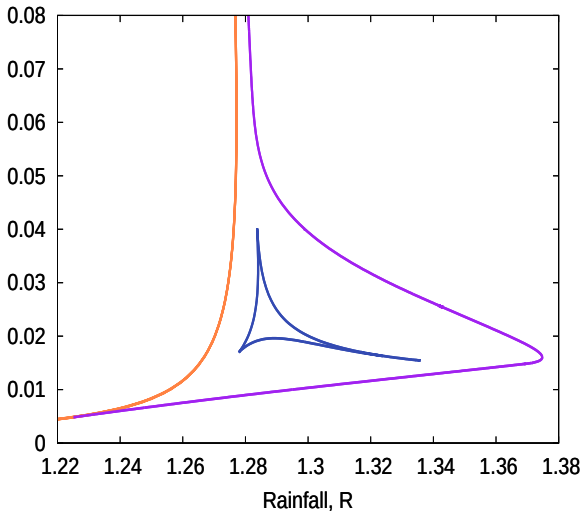

Figure 4.16: Panel (a) shows results of the fold locus computation using the indirect method. We had to compute this locus in three different steps shown in purple, green and pink curves. The green and pink curves are genuine portions of the fold locus while the purple curve starts as part of the fold locus but then drifts away into continuing homoclinic solutions. On Panel (b), we show the two fold loci side by side: in blue, we plot the locus obtained through the direct method and in purple we show the locus computed with the indirect search. We have removed the homoclinic parts from this locus to obtain a continuous curve. On both panels, we show part of the Hopf bifurcation locus in orange.

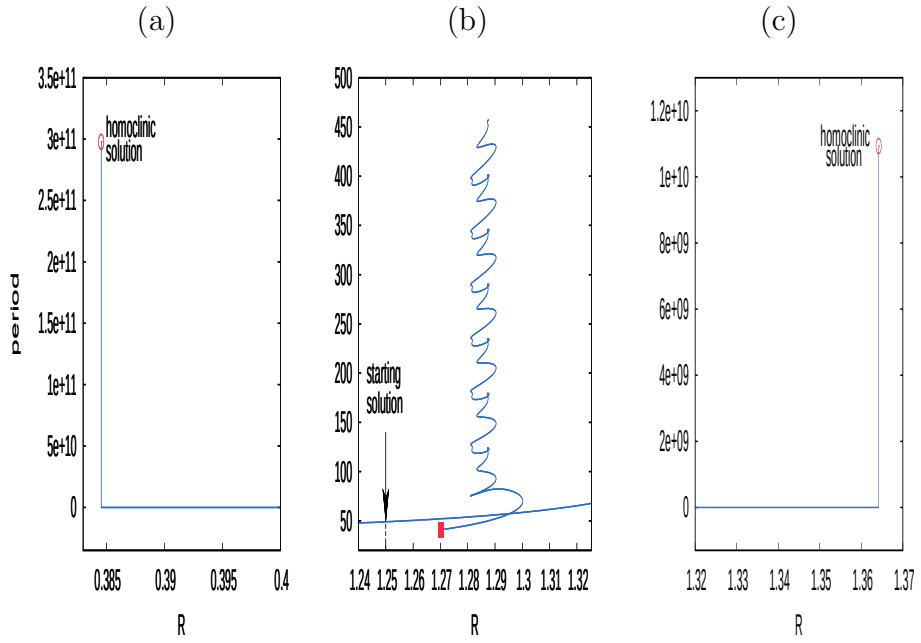

Figure 4.17: Portions of the bifurcation diagram for $c = 0.02$ computed using the file method with starting solution at $1.25, 0.02$. In fact, two bifurcation diagrams have been computed; one is the same as the diagram obtained for $c = 0.02$ using the direct search. The second one does not contain any Hopf bifurcation point and joins two homoclinic solutions; we include panels (a) and (c) to show the solution branch near these end points. On Panel (b), we can see the two different solution branches. The filled red square indicates a Hopf bifurcation point, the empty red circles indicate homoclinic solutions and the filled red circles are folds in the solution branch.

4.6 Stability Calculation of Periodic Travelling Wave solutions

Given a rainfall value R and a wave speed c, through a single command (the stability command) in `WAVETRAIN` we can check for the existence of a periodic travelling wave and if a wave is found, its stability will be calculated. Hence just like in the investigation of existence in the previous section, we can investigate wave stability on a domain using the stability command and a grid of points.

To determine stability for a periodic travelling wave, `WAVETRAIN` calculates the eigenvalue spectrum via numerical continuation. For a periodic travelling wave, eigenfunctions are solutions of a system of equations with coefficients that are periodic in the travelling wave coordinate. The eigenfunctions themselves do not need to be periodic: their amplitude needs to be periodic but there is no constraint on their phase shift γ across one

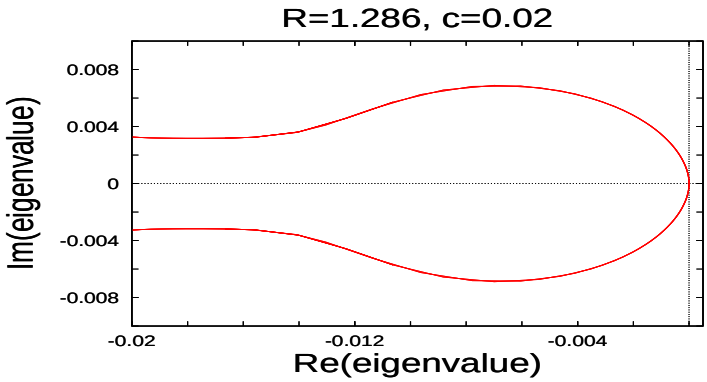

Figure 4.18: Eigenvalue spectrum for the stable wave obtained at $(R, c) = (1.286, 0.02)$ through the file search method. This result is to be compared with Figure 4.12b where we show the eigenvalue spectra of six waves obtained at the same location through the direct search method; in that case, all the waves were unstable.

period. Starting points for the numerical continuation of the spectrum are eigenvalues corresponding to periodic eigenfunctions; those correspond to $\gamma = 0$. Calculation of each eigenvalue is done by replacing derivatives with respect to R in the eigenvalue equation with $\gamma = 0$ by finite difference approximations. `WAVETRAIN` then uses incorporated linear algebra packages such as `LAPACK` and `BLAS` to solve the resulting matrix eigenvalue problem. However, while computing the eigenvalues, errors are made in the calculation of matrix eigenvalues and in the discretisation of eigenfunction equations. `WAVETRAIN` then provides for information purposes the error bounds in the calculation of the matrix eigenvalues. This information helps the user in choosing a suitable number of discretisation points (also called mesh points). This suitable number is found through a convergence test which consists of calculating eigenvalues for various numbers of mesh points and monitoring their convergence. Usually, increasing the number of mesh points helps to reduce the error in the discretisation of the eigenvalue equation. Once the periodic eigenfunctions and their corresponding eigenvalues are computed, `WAVETRAIN` uses each eigenfunction as a starting point to numerically continue the spectrum in the phase shift γ; completing this continuation for all eigenfunctions traces out the eigenvalue spectrum. Note that errors in matrix eigenvalues do not lead to errors in the computed spectra. Rather, they lead to poorer quality starting points which may prevent the numerical continuation of the spectrum from succeeding.

4.6.1 Stability of Periodic Travelling Waves in Region II

Convergence tests on Region II were all successful and having found a suitable mesh value, we calculated the (existence and) stability of periodic travelling waves. We use the domain size $[0.3, 1.3] \times [0, 0.2]$ and 51×11 grid points. Figure 4.23a shows two distinct regions: one is the set of stable solutions which are represented with filled red triangles on the grid; Figure 4.19a shows pictures of eigenvalue spectra corresponding to waves from this region. The other region represented by filled blue triangles is the set of unstable solutions; see Figure 4.19b for unstable eigenvalue spectra from this region.

4.6.2 Stability of Periodic Travelling Waves in Region I

We did a variety of convergence tests on Region I and in most cases, the matrix eigenvalues did not converge. This makes it difficult to choose a mesh number to use in investigating stability in Region I. These convergence failures suggest that Region I may be composed entirely of unstable waves. We were able to compute eigenvalue spectra at 27 different (R, c) pairs throughout the region and each spectrum crossed the c-axis meaning the corresponding periodic travelling waves are unstable. On Figure 4.20, we indicate with blue dots the location of the waves that tested unstable in Region 1. See Figures 4.21 and 4.22 for a picture of parts of the eigenvalue spectra at 24 of these locations. Due to convergence problems, these 27 waves are the only waves in Region I for which `WAVETRAIN` was able to calculate stability and they are all unstable. We are not interested in unstable solutions because they cannot be 'seen'; in other words, unstable periodic travelling wave solutions of (4.1) do not represent vegetation patterns. In addition to the fact that we were not able to locate any stable wave in wave region I, the three periodic travelling waves initially found through PDE simulations of (4.1), all belong to Region II. We will therefore focus on Region II in the remainder of this study.

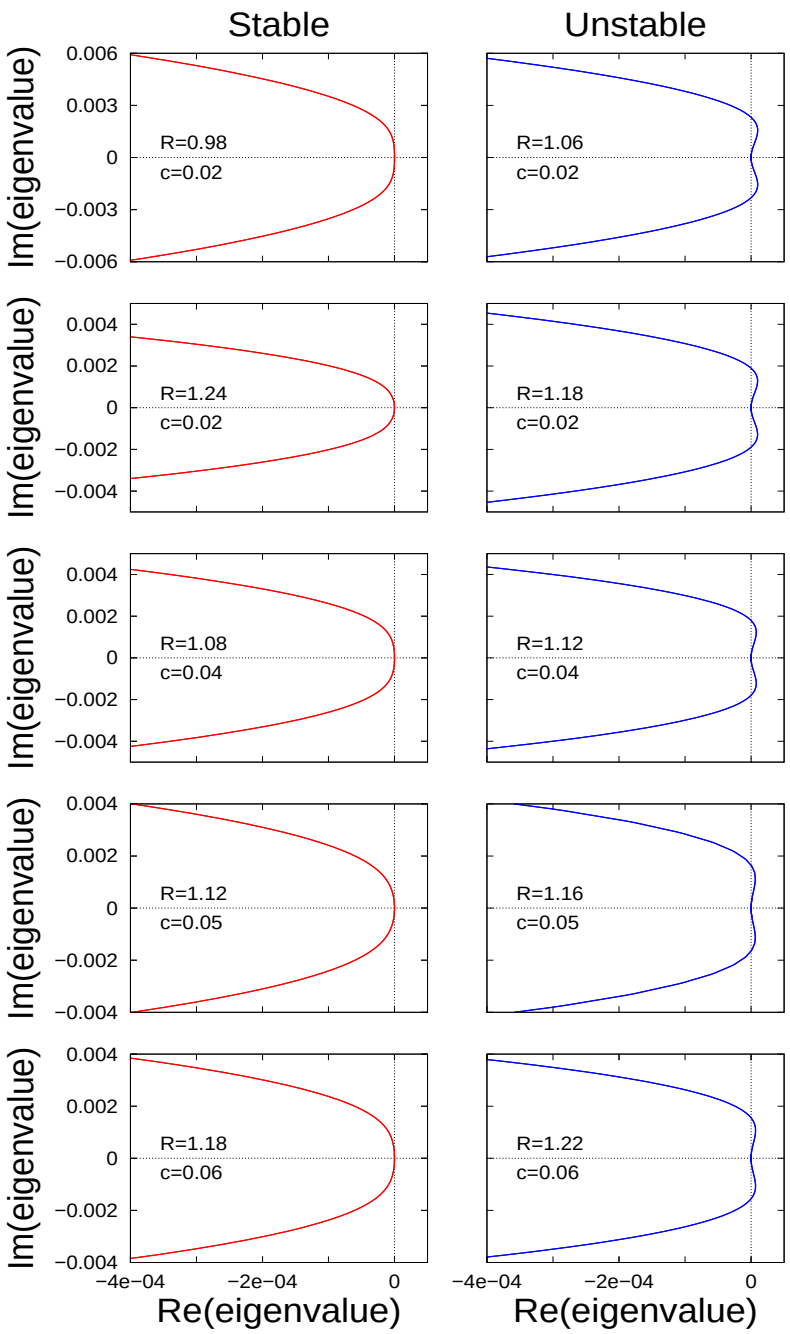

Figure 4.19: Eigenvalue spectra for ten periodic travelling wave solutions belonging to Region II. Panel (a) corresponds to five stable waves and Panel (b) shows the eigenvalue spectra of five unstable waves. In each of these cases, the change in stability occurs via a change in the sign of the curvature of the spectrum at the origin. Such a stability change is referred to as being of Eckhaus type.

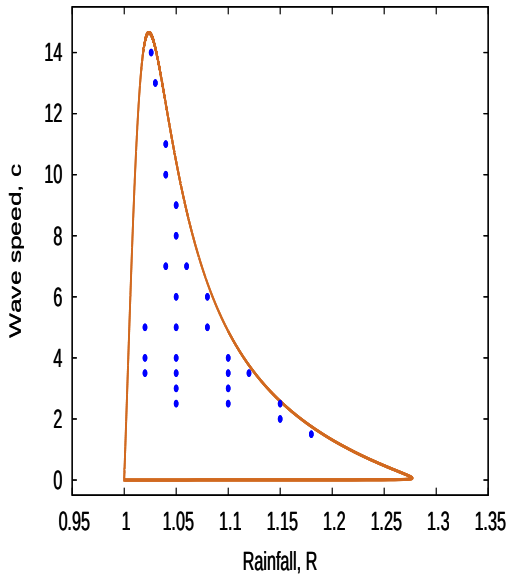

Figure 4.20: Plot showing various locations of unstable periodic travelling waves in Region I. The orange curve is the Hopf bifurcation locus and blue dots represent 27 different periodic travelling waves in Region I. Despite convergence problems during the continuation of eigenvalue spectra of waves in this region, we were able to compute portions of the spectra for these 27 waves and found that they are all unstable.

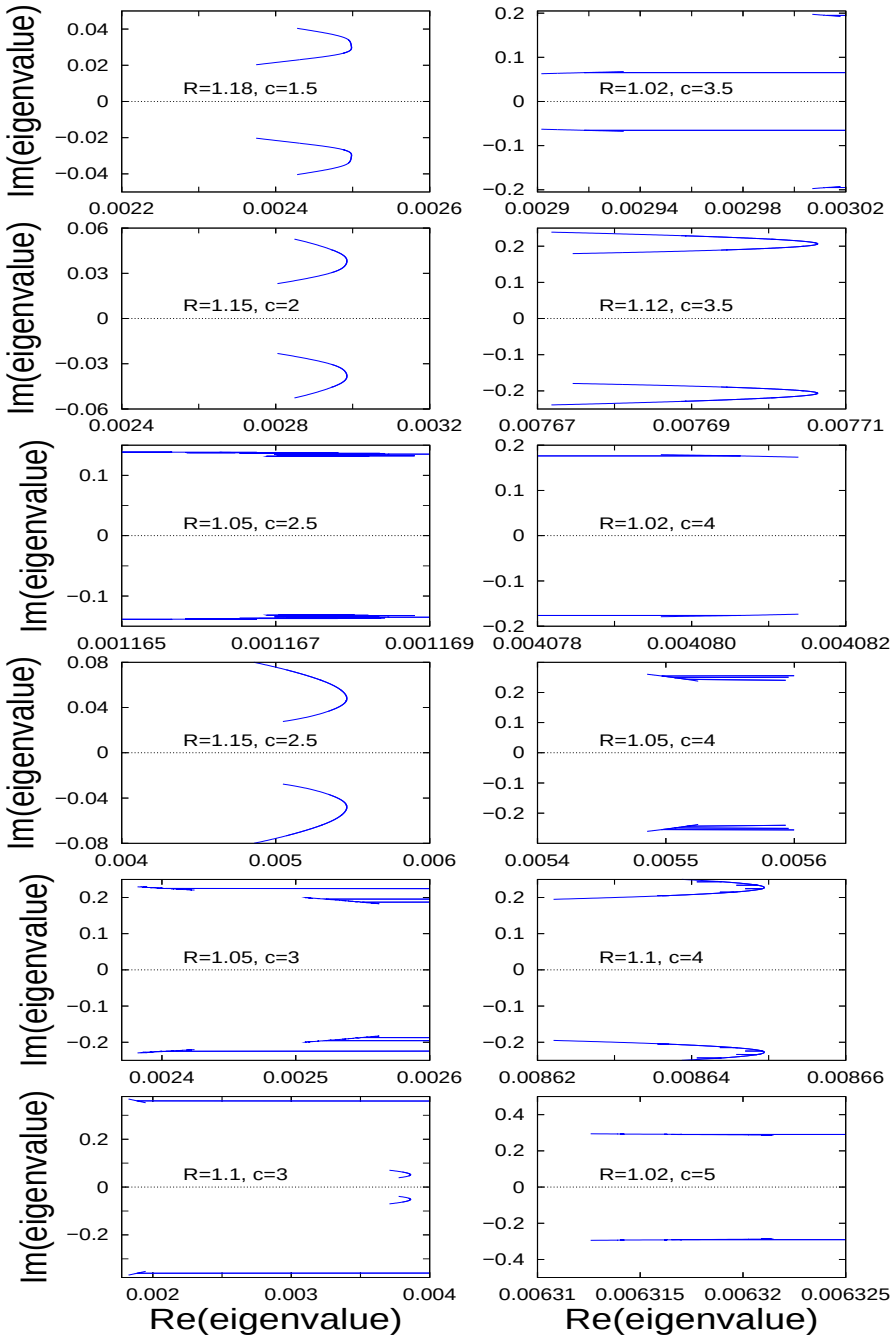

Figure 4.21: Parts of various spectra calculated for 12 different (R, c) locations within Region I. In each plot, the real part of the eigenvalue is positive. The entire spectra could not be obtained due to convergence failures, nevertheless each of these portions shows that the corresponding pattern solutions are unstable.

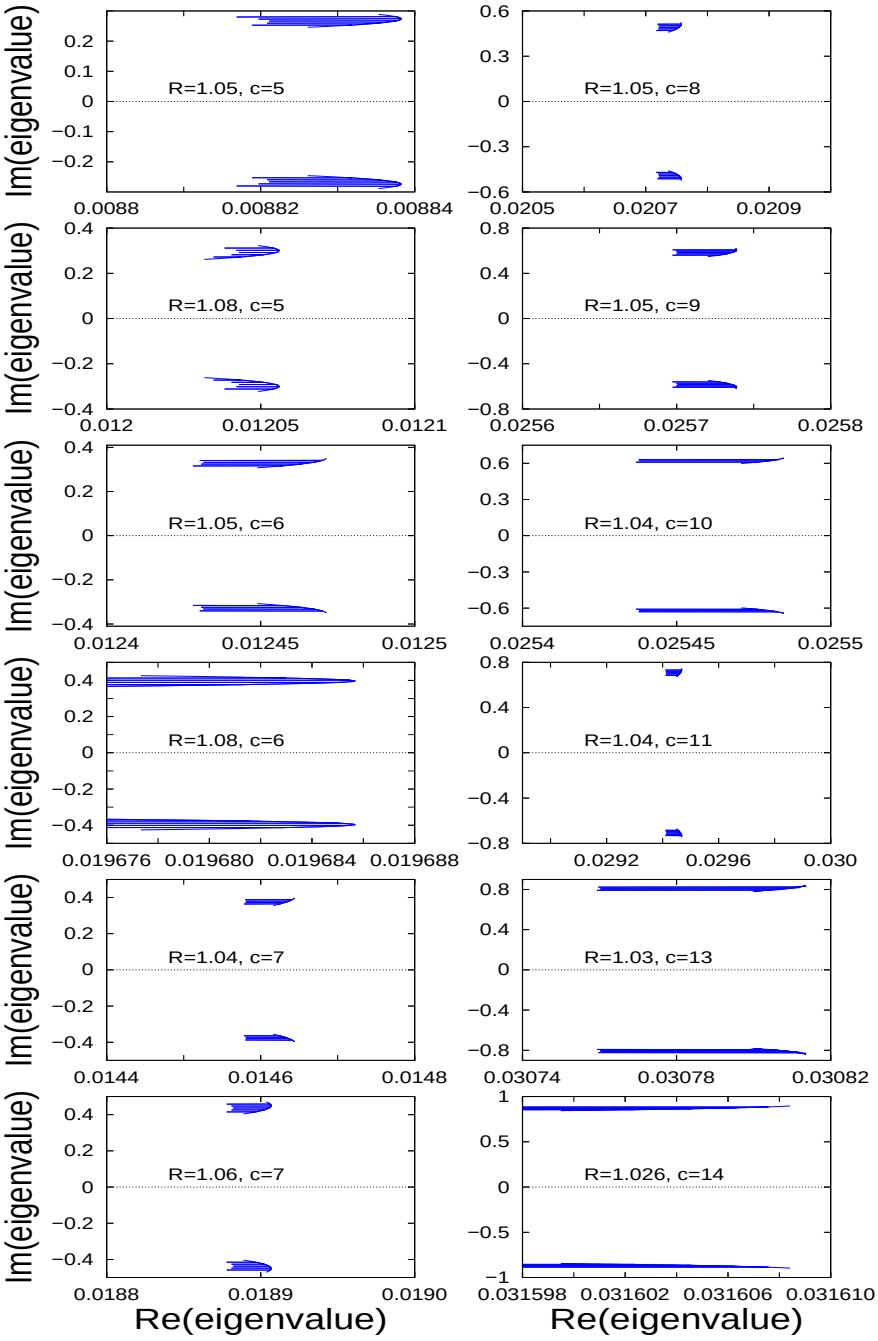

Figure 4.22: Parts of various spectra calculated for 12 different (R, c) locations within Region I. In each plot, the real part of the eigenvalue is positive. The entire spectra could not be obtained due to convergence failures, nevertheless each of these portions shows that the corresponding pattern solutions are unstable.

4.6.3 Calculation of the Stability Boundary

There are two different types of stability change in periodic travelling wave solutions: a change of Eckhaus characterised by the change of sign in the curvature of the spectrum at the origin; then there is the stability change of Hopf type where the spectrum passes through the imaginary axis away from the origin. The algorithm used by `WAVETRAIN` to calculate the stability boundary involves many steps. At first, the user enters two pairs of rainfall and wave speed values (R_1, c_1) and (R_2, c_2), where either $R_1 = R_2$ or $c_1 = c_2$. The software starts by computing the periodic travelling wave corresponding to the first pair (R_1, c_1). For the same parameter pair, the eigenfunction corresponding to the zero eigenvalue is calculated, and this is followed by the calculation of the first and second derivatives of this eigenvalue and of the corresponding eigenfunction with respect to γ. Here γ denotes the phase difference in the eigenfunction across one period of the periodic travelling wave. Next, `WAVETRAIN` continues numerically the periodic travelling wave in the travelling wave equations; eigenfunction equations will also be used to continue the eigenfunction for the zero eigenvalue, as will the first and second derivatives of this eigenvalue and eigenfunction with respect to γ by varying R and c values between (R_1, c_1) and (R_2, c_2), the two pairs entered by the user. During this continuation, the value of the real part of the second derivative of the eigenvalue with respect to γ is monitored in the search of a zero. If such a zero is found, this corresponds to a stability change of Eckhaus type and this zero will be used as a starting point for tracing the entire stability boundary. See Figure 4.23 for an example of the stability boundary computed using these steps.

If a stability change of Eckhaus type is not found, then `WAVETRAIN` proceeds to look for a stability change of Hopf type. First, the eigenvalue spectrum for wave (R_1, c_1) is computed; provided that (R_1, c_1) is sufficiently close to the stability change, this spectrum will fold at a point λ with strictly positive imaginary part. The fold with largest real part is then computed and tracked between R_1 and R_2 (c_1 and c_2) if $c_1 = c_2$ ($R_1 = R_2$). During this computation, the real part of the fold is monitored for its zero, which corresponds to a stability change of Hopf type. This zero is then continued numerically, tracing out the stability boundary.

In summary, to investigate in WAVETRAIN the existence of pattern solutions of (4.1) in a domain $\mathcal{D}$ of R, c values, it is helpful to firstly locate a few of these solutions through PDE simulations of (4.1) using perturbations of the unstable steady state (P_2, W_2, O_2) as starting solutions. Having obtained a rough idea of the location of pattern solutions through these simulations, and given that these pattern solutions might belong to a solution branch emanating from a Hopf bifurcation point, we can then define a region in which a Hopf bifurcation locus search is performed. Once this locus is found, we define grid points on the domain $\mathcal{D}$ and we run a loop through these points to investigate wave existence using the direct method in simple cases and the indirect/file method in more complicated cases. The completion of this loop will reveal a region or regions of waves in the domain $\mathcal{D}$ (see Figure 4.7) and we will calculate the boundaries of of this/these region(s); these boundaries can be either a Hopf bifurcation locus, a locus of folds or a locus of homoclinic solutions (see Figure 4.23). Once wave regions are found and delimited, we then proceed to investigating the stability of the waves in each region. When both stable and unstable waves are found in a region, we calculate the stability boundary (see Figure 4.23b). In the next section, this stability boundary will play a key role as we investigate the effects of environmental changes on pattern solutions.

4.7 The Effect of Variations in Rainfall on Pattern Solutions

Patterns that are observed in aerial photographs and satellite images of arid ecosystems in reality change slowly over time due to environmental changes. In this section, we take a closer look at the effects of environmental changes on the way vegetation patterns form. We do this by studying how variations in the rainfall parameter R affect PDE solutions of (4.1). We compute numerical solutions of (4.1) with periodic boundary conditions for (R,c) pairs in Region II, using the results from WAVETRAIN to guide and explain our simulations.

With the domain fixed at 500, we undertook a simulation study of how pattern solutions of initial wave numbers 7, 8, 9 and 10 (Figures 4.24-4.27 respectively) evolve as we slowly change R. On each figure, contours of constant pattern wavelength are shown in red (initial wavelength), blue and purple (other wavelengths). The green curve shows the stability boundary. In each case, the period contour intersects the stability boundary at four points which represent stability thresholds; here we focus on the thresholds at the smallest and the largest rainfall values. To study the behaviour of patterns as rainfall decreases/increases below or above a particular threshold, we start PDE simulations with

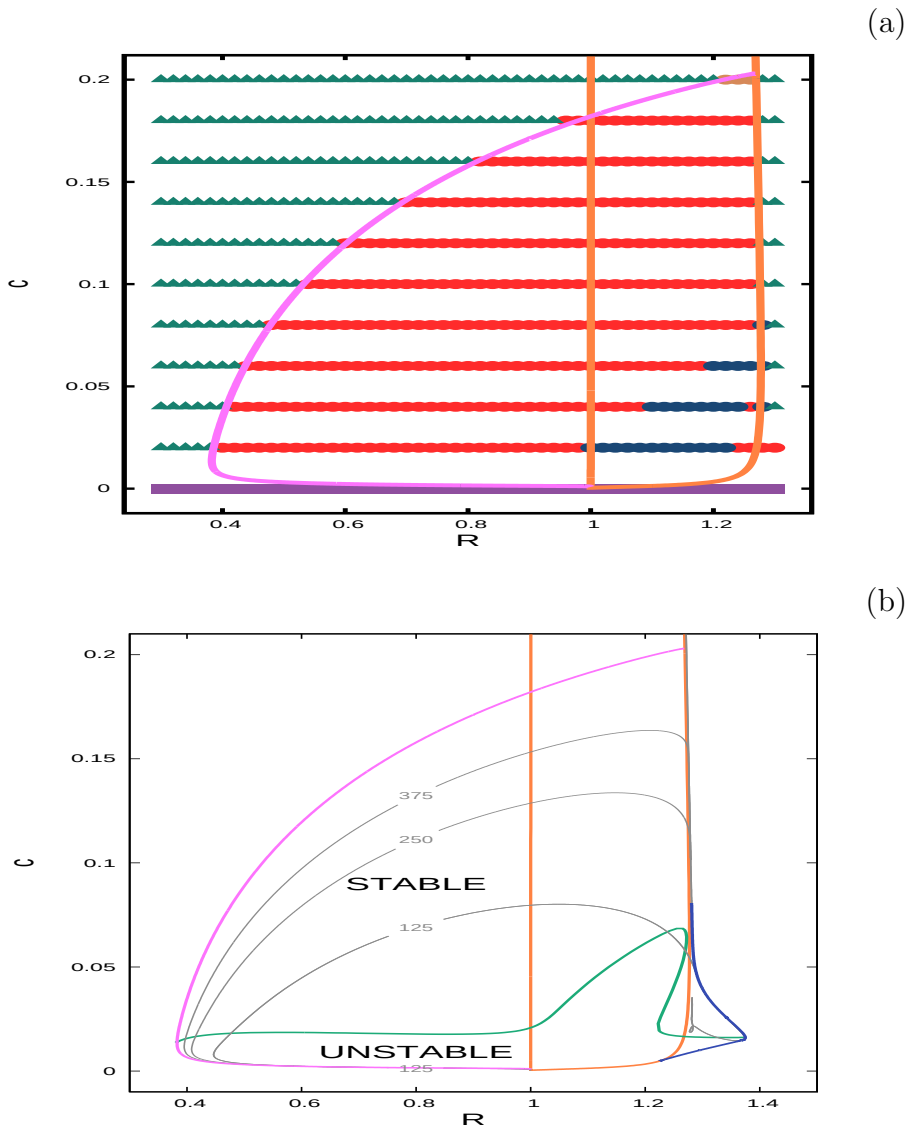

Figure 4.23: Panel (a): a grid of 51×11 points on the domain $[0.3, 1.3] \times [0, 0.2]$ showing the stability calculation results. The filled red circles are stable wave solutions while the filled blue circles are unstable solutions. Green triangles indicate that a periodic travelling wave has not been detected at the corresponding location due to a convergence failure. Purple squares correspond to locations where no periodic travelling wave was found even though convergence occurred along the whole solution branch. We show the stability boundary in green and the pink curve is the set of homoclinic solutions; the locus of folds and a portion of the Hopf locus are shown in blue and orange respectively. Panel (b) shows the same stability calculation results without the grid points; contours of constant periods 125, 250 and 375 have been added (grey curves). Here the R range has been extended to $[0.3, 1.4]$ in order to display the entirety of stability boundaries and loci of folds.

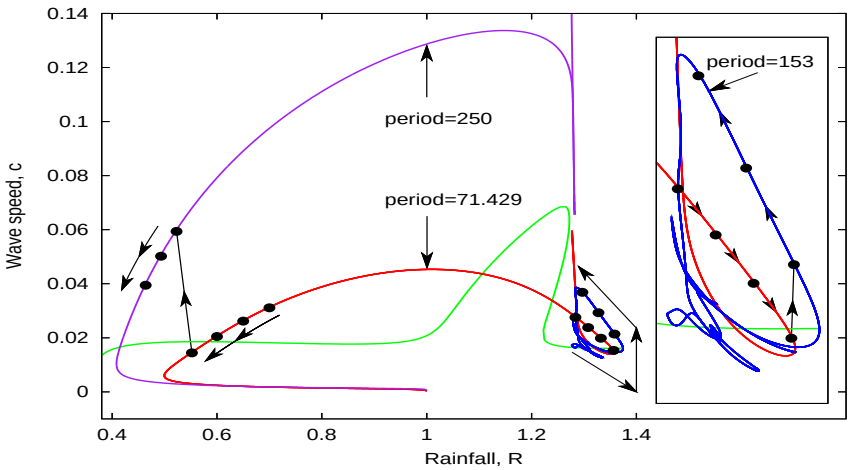

Figure 4.24: Numerical solutions of (4.1) solved with a wave initially on the period contour of period 71.429 (= 500/7). The insert shows details of how patterns are affected as the rainfall increases above the stability threshold; the range on the vertical axis is $0.01 < c < 0.04$ while that on the horizontal axis is $1.27 < R < 1.38$. As R is increased through a change in wave stability, the wavelength switches to 153; the contour of constant wavelength 153 was calculated through the file method (blue curve). The black dots represent the wavelength and speed obtained as R is varied, and arrows indicate the direction of this variation. The PDE solutions were computed using a finite difference scheme with periodic boundary conditions. We used a spatial grid spacing of 0.25 and fixed the CFL number at 0.8 by using a time step of 0.04.

a stable solution belonging to the period contour. We can easily obtain these starting stable solutions from `WAVETRAIN`. Then R is changed slowly and as the corresponding threshold is crossed, the wave becomes unstable as a PDE solution. Before each change of R value, the wave speed and wavelength are recorded. There is an abrupt change in the speed of the pattern as the wave stability changes; and the form of the pattern also changes abruptly. For example, in the case of periodic travelling waves of initial wavelength 71.428 (= 500/7), the two stability thresholds considered are located at $R = 0.583$ and $R = 1.354$. As R is decreased below $R = 0.583$, the wavelength shifts from 71.428 to 250; similarly, as R increases above $R = 1.354$, we see a shift in wavelength from 71.428 to 150 (Figure 4.24).

We do not know how to predict the value of the new wavelength after these shifts occur; calculating basins of attraction for different periodic travelling waves could help answer this question but this would be very difficult. However, we have noticed that the new wavelength value depends closely on the gap between the R values used right before and right after the rainfall value at the stability threshold. For example, in the case of the

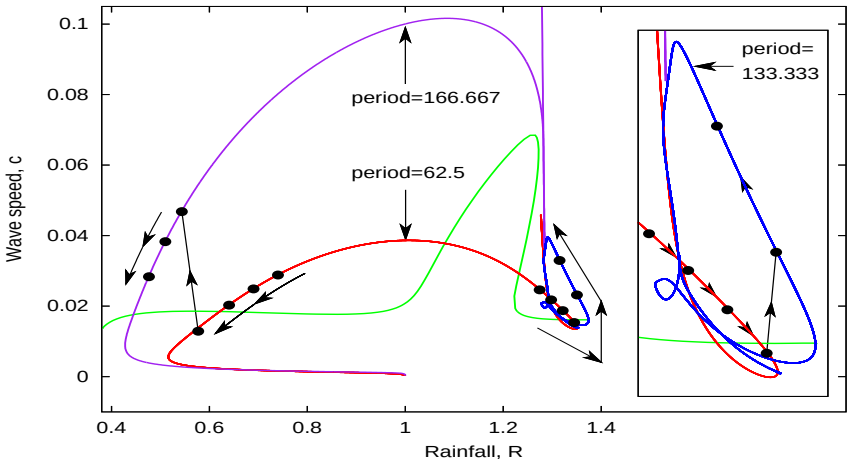

Figure 4.25: Numerical solutions of (4.1) solved with a wave initially on the period contour of period 62.5 (= 500/8). The insert shows details of how patterns are affected as the rainfall increases above the stability threshold; the range on the vertical axis is $0.012 < c < 0.04$ while that on the horizontal axis is $1.268 < R < 1.381$. The black dots represent the wavelength and speed obtained as R is varied and arrows indicate the direction of this variation. The numerical details for the PDE simulations are the same as in the case of Figure 4.24

contour of pattern wavelength 50, we have a stability threshold at $R = 0.705$. When we go from one side of the stability boundary to the other by changing R from 0.73 to 0.64, at first there is no shift in wavelength (Figure 4.28a shows a plot of the PDE solution at $R = 0.64$). It takes a second change in R to see a shift in wavelength from 50 to $500/3 \simeq 166.667$ (Figure 4.27). However, when a bigger change in R is done from 0.73 to 0.61, the shift in wavelength from 50 to 166.667 (= 500/3) occurs immediately. See Figure 4.28b for a picture of the the PDE solution at $R = 0.61$. When we attempted an even bigger change going from 0.73 to 0.57, the computations yield the desert state (Figure 4.28c).

Also, the value of the new wavelength is highly influenced by the period of time over which a change in rainfall occurs. We investigated this through PDE simulations with the pattern solution for rainfall value $R = 0.73$ (with wavelength 50) as starting solution. In each case, we vary R from 0.73 to 0.64 then to 0.61 and finally to 0.57 over different decreasing time intervals. Our results show that if environmental changes occur quickly, then vegetation patterns do not change. Table 4.1 shows simulations results for time intervals decreasing from 20000 to 100.

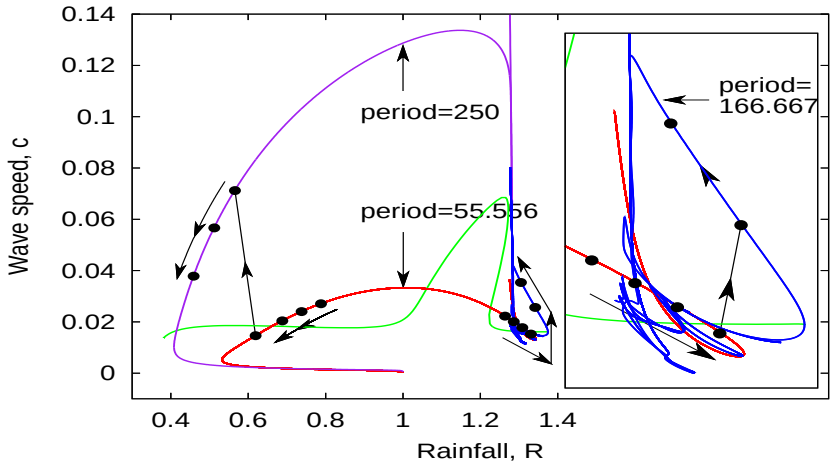

Figure 4.26: Numerical solutions of (4.1) solved with a wave initially on the period contour of period 55.556 (= 500/9). The insert shows details of how patterns are affected as the rainfall increases above the stability threshold; the range on the vertical axis is $0.01 < c < 0.044$ while that on the horizontal axis is $1.25 < R < 1.381$. When R is increases until a change in wave stability, the wavelength switches to 166.667; the contour of constant wavelength 166.667 was calculated through the file method (blue curve). The black dots represent the wavelength and speed obtained as R is varied and arrows indicate the direction of this variation. The numerical details for the PDE simulations are the same as in the case of Figure 4.24

A variety of other results from simulations of variations in rainfall R are shown in Figures 4.29-4.34. In the next section, we briefly look at the dynamics of system (4.1) when diffusion is added to the surface water equation and soil gradient is varied.

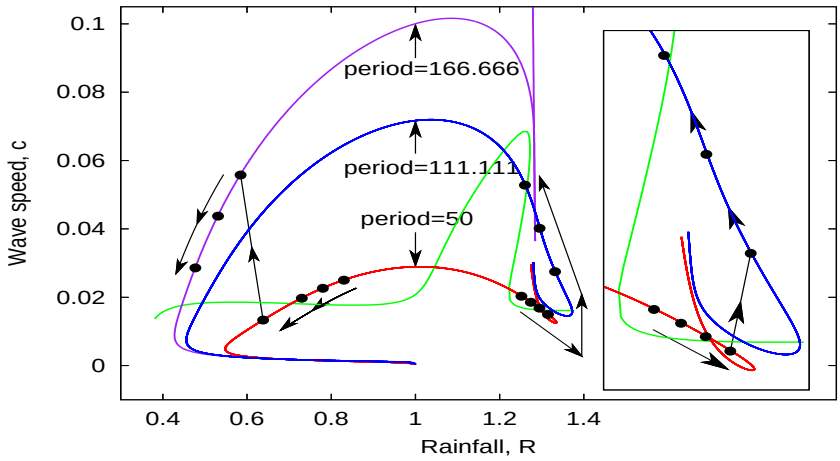

Figure 4.27: Numerical solutions of (4.1) solved with a wave initially on the period contour of period 50. The insert shows details of how patterns are affected as the rainfall increases above the stability threshold; the range on the vertical axis is $0.01 < c < 0.056$ while that on the horizontal axis is $1.21 < R < 1.38$. The black dots represent the wavelength and speed obtained as R is varied and arrows indicate the direction of this variation. The numerical details for the PDE simulations are the same as in the case of Figure 4.24

R	**time= 20000**	**time= 10000**	**time= 5000**	**time= 200**	**time= 100**
0.64	50	50	50	50	50
0.61	166.67	166.67	50	50	50
0.57	166.67	166.67	166.67	166.67	50

Table 4.1: Table showing that depending on how quickly environmental changes occur, vegetation patterns may or may not change. We start with the wave of period 50 at $R = 0.73$ as initial solution and compute PDE solutions of 4.1 gradually decreasing R through 0.64, 0.61 and 0.57. This is done in a single run and we use a fixed time interval at each of these rainfall values. These PDE solutions are highly influenced by the width of the time interval. The tabulated values are the wavelengths of the PDE solutions obtained at the different amounts of rainfall using time intervals fixed between 50 and 20000.

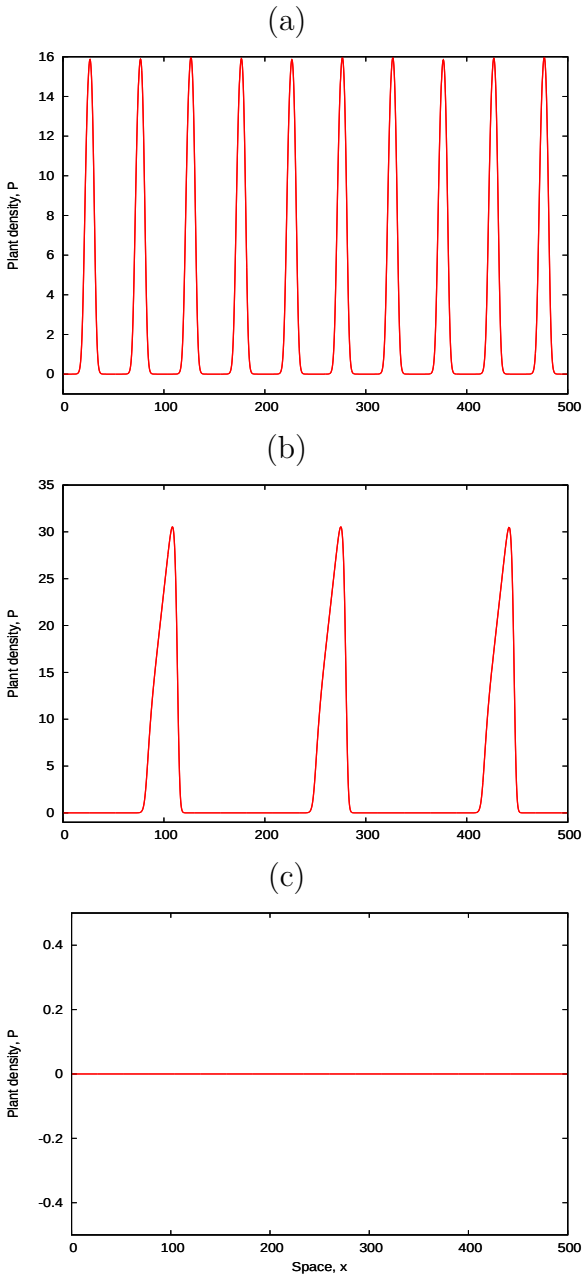

Figure 4.28: PDE solutions showing how the gap between rainfall values while crossing the stability threshold can affect vegetation patterns. We start with a PDE solution for rainfall value $R = 0.73$ with wavelength 50. This solution is stable and the change in stability occurs when R falls below 0.705. When we change R from 0.73 to 0.64, hence switching to an unstable pattern solution, the wavelength stays the same; see Panel (a) for the PDE solution for rainfall value $R = 0.64$ with wavelength 50. However, when we take a bigger step from 0.73 to 0.61, the wavelength changes from 50 to 166.667; this solution is shown on Panel (b). When we attempted an even bigger change going from 0.73 to 0.57, the computations yield the desert state shown on Panel (c).

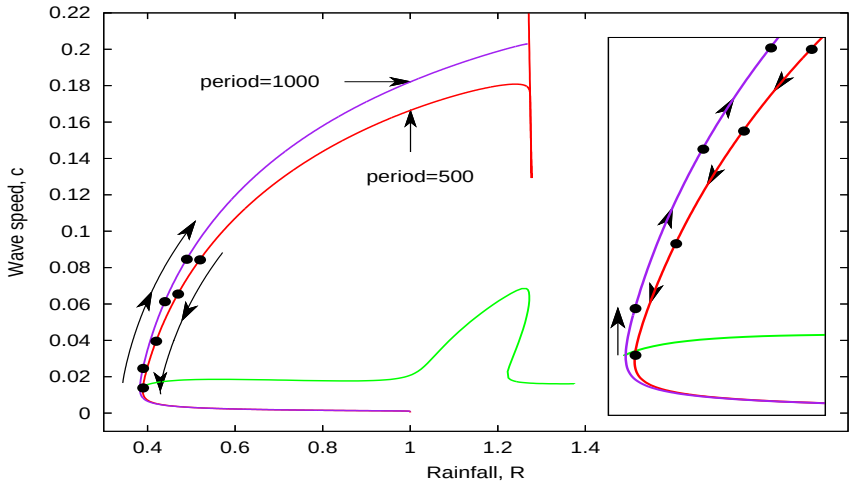

Figure 4.29: Numerical solutions of (4.1) solved with a wave initially on the period contour of period 500. The insert shows details of how patterns are affected as the rainfall decreases until falling below the stability threshold; the range on the vertical axis is $0 < c < 0.087$ while that on the horizontal axis is $0.37 < R < 0.53$. The black dots represent the wavelength and speed obtained as R is varied and arrows indicate the direction of this variation. The numerical details for the PDE simulations are the same as in the case of Figure 4.24.

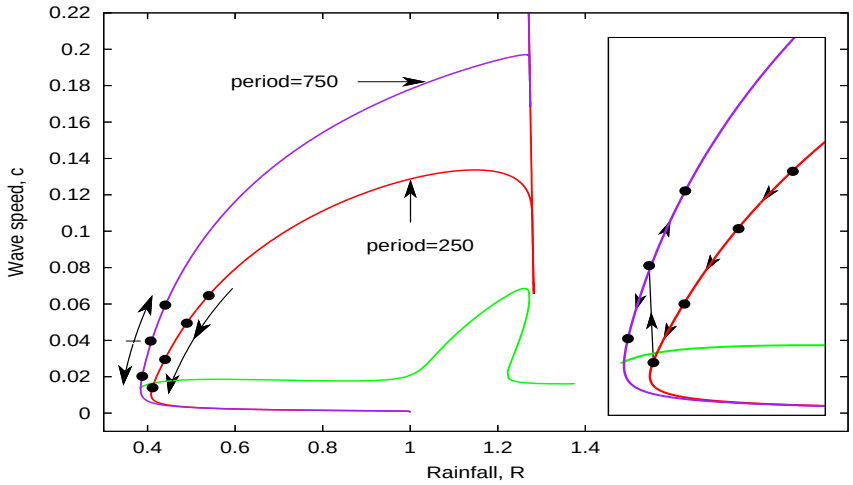

Figure 4.30: Numerical solutions of (4.1) solved with a wave initially on the period contour of period 250. The insert shows details of how patterns are affected as the rainfall decreases until falling below the stability threshold; the range on the vertical axis is $0 < c < 0.1$ while that on the horizontal axis is $0.37 < R < 0.57$. The black dots represent the wavelength and speed obtained as R is varied and arrows indicate the direction of this variation. The numerical details for the PDE simulations are the same as in the case of Figure 4.24.

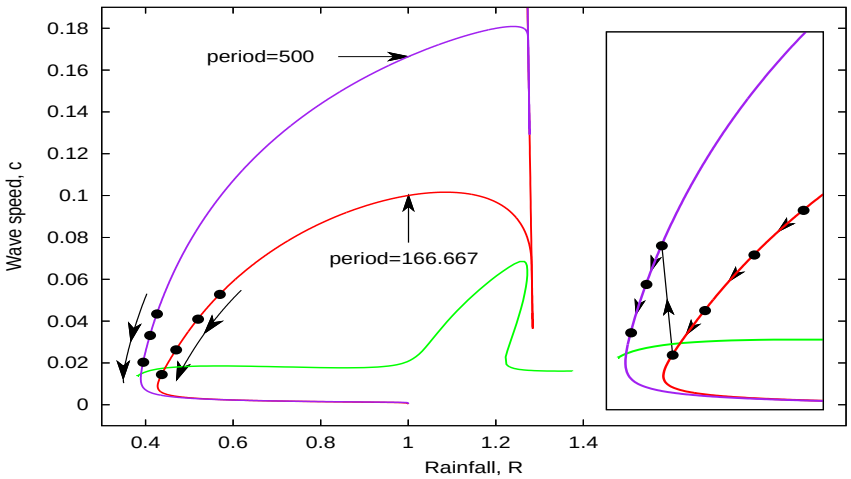

Figure 4.31: Numerical solutions of (4.1) solved with a wave initially on the period contour of period 166.667 (= 500/3). The insert shows details of how patterns are affected as the rainfall decreases until falling below the stability threshold; the range on the vertical axis is $0 < c < 0.1$ while that on the horizontal axis is $0.37 < R < 0.59$. The black dots represent the wavelength and speed obtained as R is varied and arrows indicate the direction of this variation. The numerical details for the PDE simulations are the same as in the case of Figure 4.24.

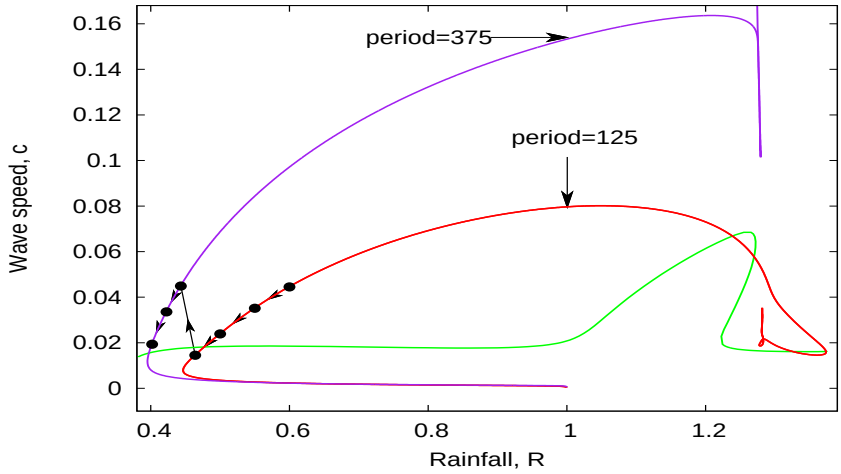

Figure 4.32: Numerical solutions of (4.1) solved with a wave initially on the period contour of period 125. The black dots represent the wavelength and speed obtained as R is varied and arrows indicate the direction of this variation. The numerical details for the PDE simulations are the same as in the case of Figure 4.24.

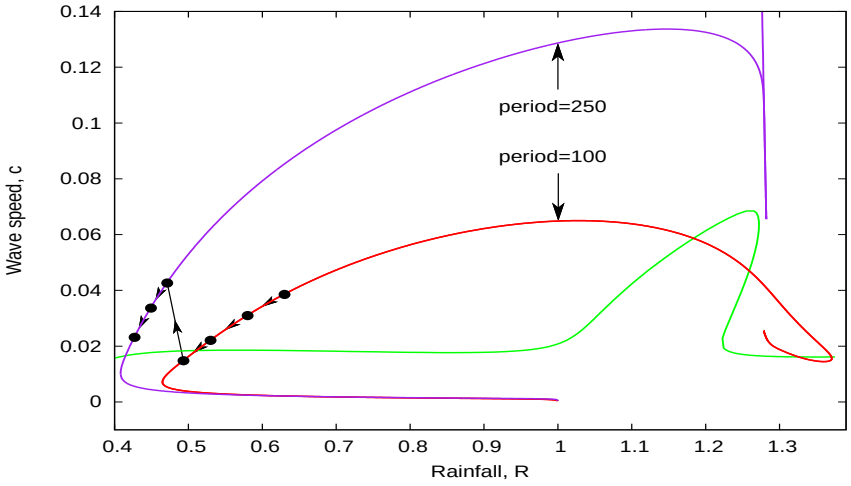

Figure 4.33: Numerical solutions of (4.1) solved with a wave initially on the period contour of period 100. The black dots represent the wavelength and speed obtained as R is varied and arrows indicate the direction of this variation. The numerical details for the PDE simulations are the same as in the case of Figure 4.24.

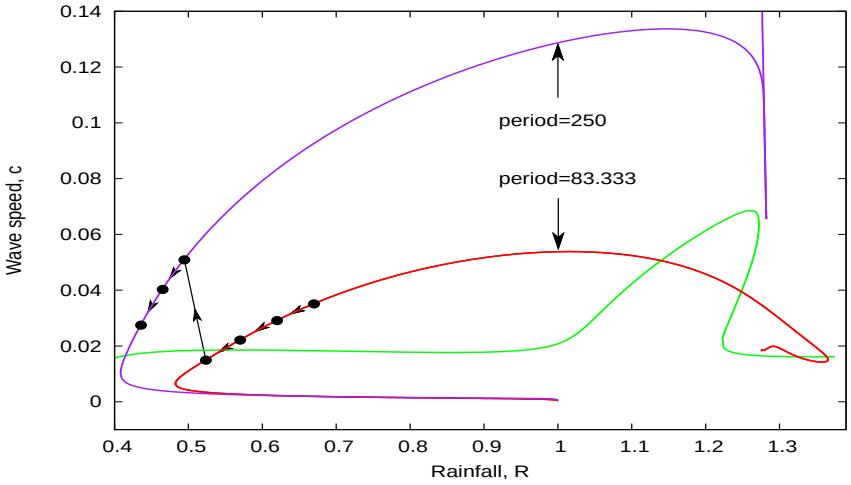

Figure 4.34: Numerical solutions of (4.1) solved with a wave initially on the period contour of period 83.333 ($= 500/6$). The black dots represent the wavelength and speed obtained as R is varied and arrows indicate the direction of this variation. The numerical details for the PDE simulations are the same as in the case of Figure 4.24.

4.8 Diffusion in Surface Water

The Rietkerk model (4.1) is a variant of the HilleRisLambers' (2001) model in which propagation of surface water O was originally modelled with a diffusion term $D_O O_{xx}$. Rietkerk et al. (2002) extended this model by replacing the diffusion by the flow downhill νO_x. Here we reintroduce the diffusion term so that surface water motion is a result of both diffusion and downhill flow. In other words, Equation (4.1) becomes:

$$P_t = D_P P_{xx} + f(P, W, O) \tag{4.6a}$$

$$W_t = D_W W_{xx} + g(P, W, O) \tag{4.6b}$$

$$O_t = D_O O_{xx} + \nu O_x + h(P, W, O) \tag{4.6c}$$

where $D_O O_{xx}$ represents surface water diffusion; Rietkerk et al. (2002) suggest $D_O = 100$ although there is no conclusive empirical data on which the value can be based. In this section, both ν and D_O will be varied while all the other parameter values are fixed as in Section 4.1.

4.8.1 Gradually Increasing D_O

Firstly, we keep $\nu = 10$ and investigate periodic travelling wave existence and stability using this extended model 4.6 for $D_O = 1,\ 25,\ 50$ and 100. In all four cases, use of `WAVETRAIN` as described previously reveals two wave regions Region I and Region II similar to those discussed in Section 4.4 (see Figure 4.7). For each D_O value, `WAVETRAIN` again experienced convergence failures in Region I but managed to calculate stability for a few waves and they were all unstable; in Region II, both stable and unstable waves were found and we traced the stability boundaries. Here we show only results in each Region II and these are presented in Figures 4.35 and 4.36. On one hand, the stability change is of Eckhaus type for $D_O = 1$ and $D_O = 25$ and the region of stable/unstable waves (Figure 4.35(a) for $D_O = 1$ and Figure 4.35(b) for $D_O = 25$) looks similar to the region of stable/unstable waves previously obtained in the $D_O = 0$ case (Figure 4.23). On the other hand, the stability boundary for $D_O = 50$ (Figure 4.36(a)) looks slightly similar to that for $D_O = 100$ (Figure 4.36(b)), however the stability change is of Eckhaus type in the first case and of Hopf type in the second. We also investigated wave stability for $D_O = 34$; the results show that the stability boundary is pinching (Figure 4.37). This helps understand how the change in shape of the stability boundary occurs between $D_O = 25$ (Figure 4.35b) and $D_O = 50$ (Figure 4.36). See Figure 4.38 for illustration of various eigenvalue spectra for both $D_O = 50$ and $D_O = 100$.

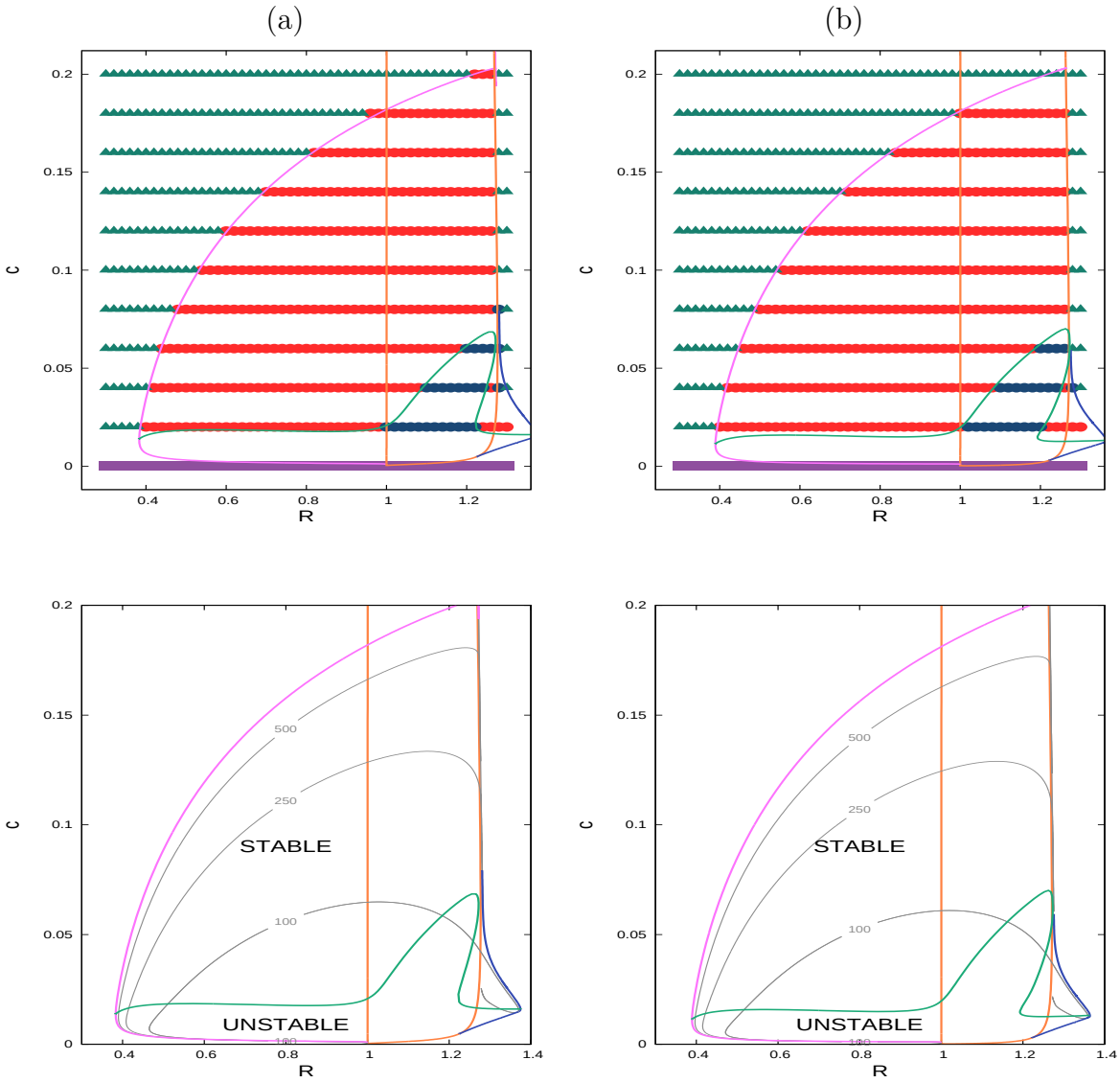

Figure 4.35: Top row: a grid of 51×11 points on the domain $[0.3, 1.3] \times [0, 0.2]$ showing the stability calculation results for $D_O = 1$ (a) and $D_O = 25$ (b). The filled red circles are stable wave solutions while the filled blue circles are unstable solutions. Green triangles indicate that a periodic travelling wave has not been detected at the corresponding location due to a convergence failure. Purple squares correspond to locations where no periodic travelling wave was found even though convergence occurred along the whole solution branch. The stability change is of Eckhaus type in both cases and stability boundaries are shown in green. In pink, we plot the set of homoclinic solutions; the locus of folds and a portion of the Hopf locus are shown in blue and orange respectively. The bottom row shows the same stability calculation results without the grid points; contours of constant periods 100, 250 and 500 have been added (grey curves). Here the R range has been extended to $[0.3, 1.4]$ in order to display the entirety of stability boundaries and loci of folds.

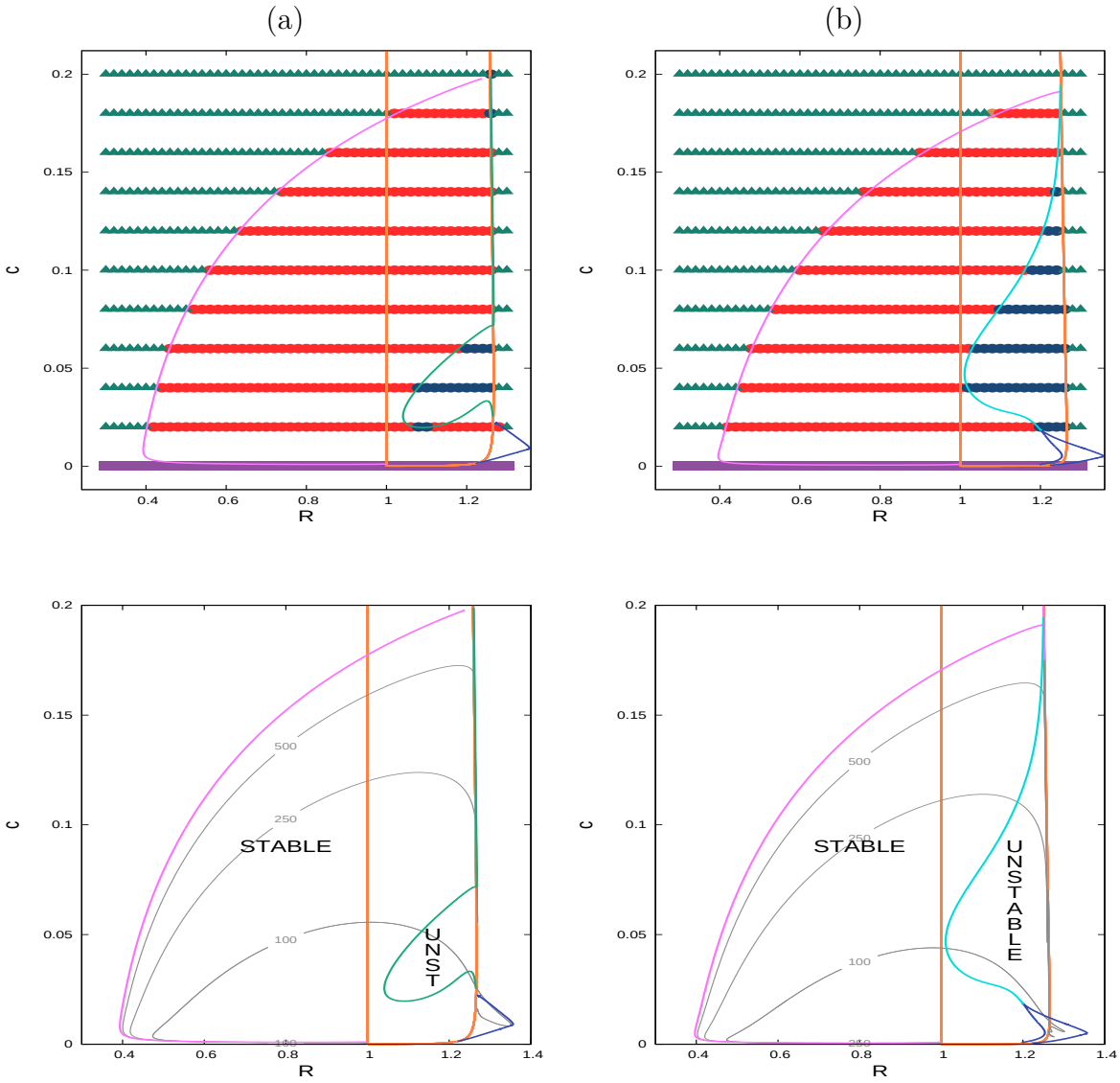

Figure 4.36: Top row: a grid of 51×11 points on the domain $[0.3, 1.3] \times [0, 0.2]$ showing the stability calculation results for $D_O = 50$ (a) and $D_O = 100$ (b). The filled red circles are stable wave solutions while the filled blue circles are unstable solutions. Green triangles indicate that a periodic travelling wave has not been detected at the corresponding location due to a convergence failure. Purple squares correspond to locations where no periodic travelling wave was found even though convergence occurred along the whole solution branch. The stability change is of Eckhaus type in the $D_O = 50$ case; we show the stability boundary in green. In the $D_O = 100$ case, we plot the stability boundary in cyan to indicate that it is of Hopf rather than Eckhaus type. In pink, we plot the set of homoclinic solutions; the locus of folds and a portion of the Hopf locus are shown in blue and orange respectively. The bottom row shows the same stability calculation results without the grid points; contours of constant periods 100, 250 and 500 have been added (grey curves). Here the R range has been extended to $[0.3, 1.4]$ in order to display the entirety of stability boundaries and loci of folds.

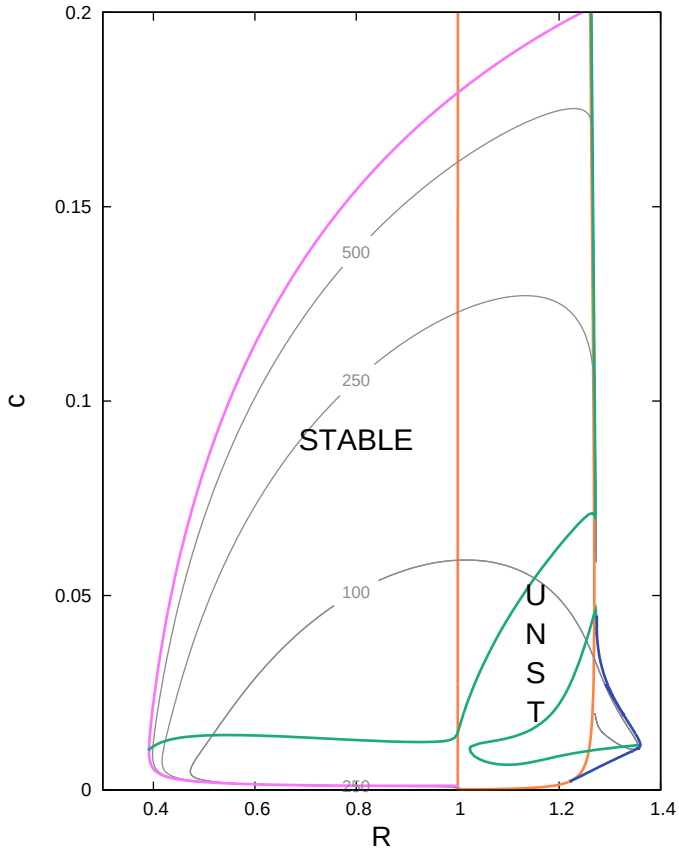

Figure 4.37: Stability calculation results for $D_O = 34$. The meaning of the curves is the same as in Figure 4.36. Here the stability boundary is pinching; this helps understand how the change in shape of the stability boundary occurs between $D_O = 25$ (Figure 4.35b) and $D_O = 50$ (Figure 4.36a).

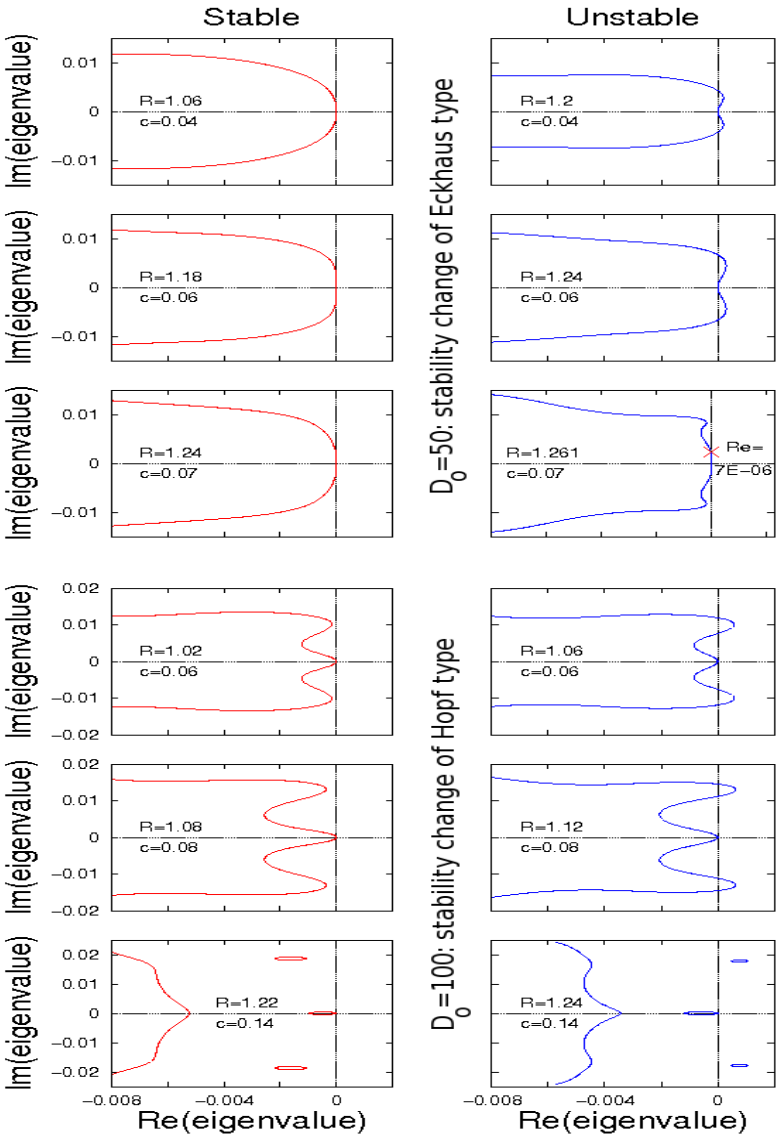

Figure 4.38: Eigenvalue spectra of waves near the stability boundary in the cases $D_O = 50$ and $D_O = 100$. Panel (a) displays stable spectra and Panel (b), unstable spectra. The first three rows represent waves at $c = 0.04,\ 0.06$ and 0.07 for $D_O = 50$; each time, a change of sign in the curvature of the spectrum at the origin occurs (stability change of Eckhaus type). In the last three rows, $c = 0.06,\ 0.08$ and 0.14 for $D_O = 100$ and we see the spectrum passing through the imaginary axis away from the origin: the stability change is of Hopf type.

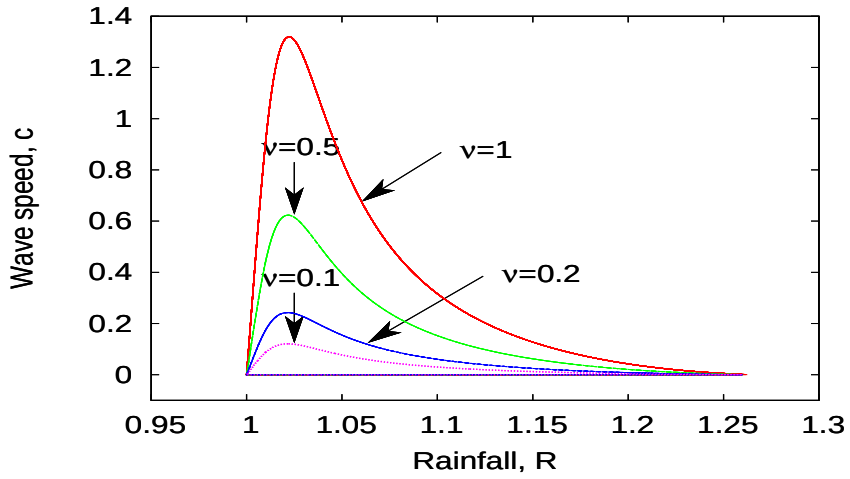

Figure 4.39: Hopf bifurcation loci for $\nu = 0.1,\ 0.2,\ 0.5$ and 1 with D_O fixed at 100. The region enclosed by these loci decreases in area as ν decreases.

In summary, we investigated, in Sections 4.4 and 4.6, periodic travelling wave existence and stability when the exchange of surface water with surrounding areas occurs only through its flow downhill; in this section, we have done the same investigation, this time with added diffusion in surface water. A natural question now is: what happens when there is diffusion of surface water but on either a very slight slope or bare ground, so that the advection coefficient ν is small or zero?

4.8.2 Gradually Decreasing ν

With D_O now fixed at 100, we investigate how wave regions vary as ν decreases. First we compute various Hopf bifurcation loci as ν is decreased between 10 and 0. The region enclosed by these loci decreases in area as ν is decreased. This suggests that wave regions become smaller as ν decreases, though a more detailed study would be required to confirm this. See Figure 4.39 for a plot of the Hopf bifurcation loci for $\nu = 0.1,\ 0.2,\ 0.5$ and 1

To explore how patterns are affected as advection becomes small, we investigate wave existence for $\nu = 0.01$. The wave search loop reveals, contrary to previous results, a single wave region much bigger in size than the region enclosed by the Hopf bifurcation locus; see Figure 4.40a for the wave search results on the domain $[0.55, 1.27] \times [0, 0.1]$ represented with a 19×26 grid. A stability loop reveals that all the waves in this wave region are unstable (see Figure 4.40b)

When $\nu = 0$, we are unable to find a Hopf bifurcation locus in `WAVETRAIN`. PDE

(a)

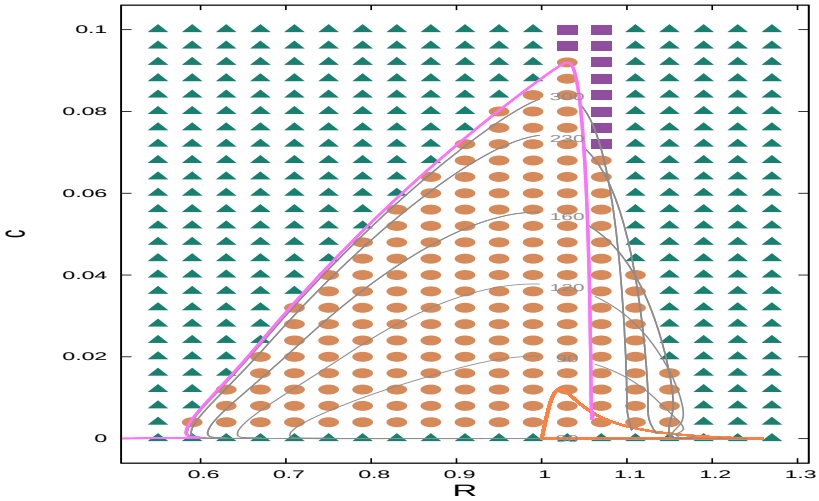

(b)

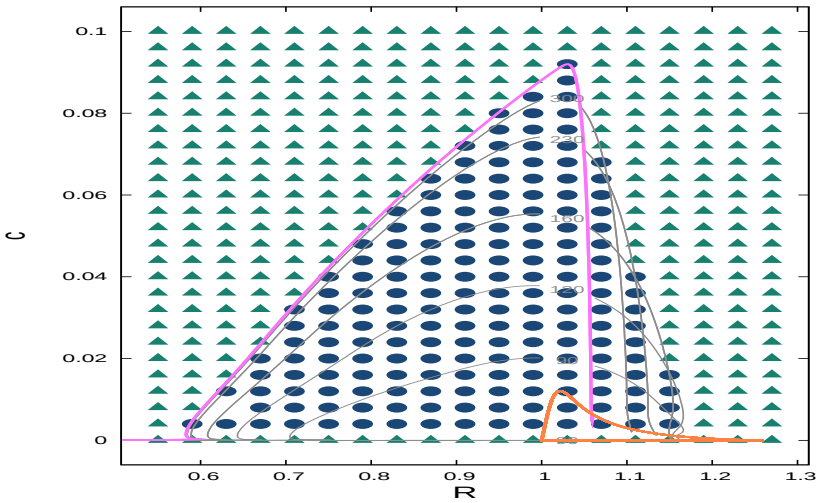

Figure 4.40: Results of the wave search (a) and stability (b) loops for $D_O = 100$ and $\nu = 0.01$ on the domain $[0.55, 1.27] \times [0, 0.1]$ defined as a grid of 19×26 points. Green triangles indicate that a periodic travelling wave has not been detected at the corresponding location due to a convergence failure. Purple squares correspond to locations where no periodic travelling wave was found even though convergence occurred along the whole solution branch. On Panel (a), filled orange circles indicate the existence of periodic travelling waves at the corresponding (R, c) locations; we see a single wave region that extends far beyond the Hopf bifurcation locus shown in its entirety in the orange curve. On Panel (b), filled blue circles indicate unstable periodic travelling waves: all the waves we found are unstable. The pink curve is the set of homoclinic solutions while the grey curves are contours of constant period, with period = 90, 120, 160, 230 and 300 from bottom to top.

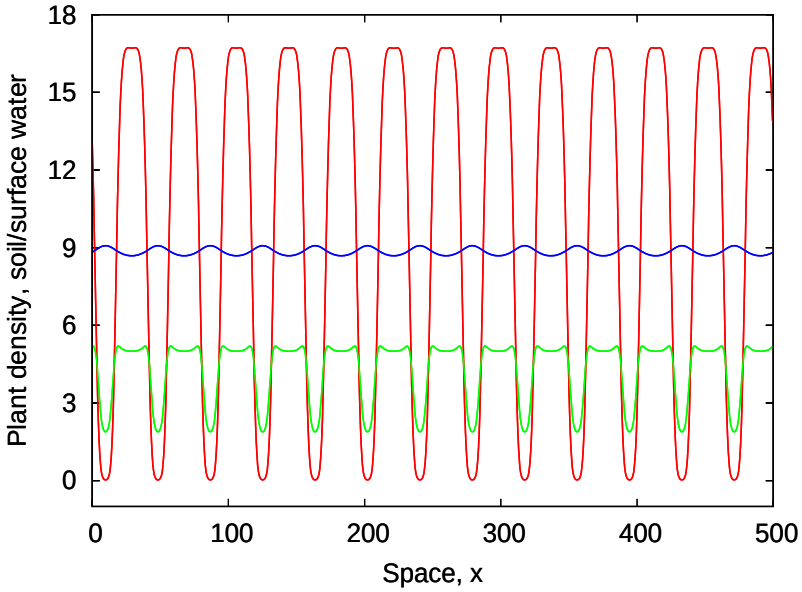

Figure 4.41: Periodic stationary solution of the extended Rietkerk model (4.6) for $R = 1.1$, $D_O = 100$ and $\nu = 0$ at time $= 12000$. We plot plant density in red, soil water in green and surface water in blue. The grid points for our starting solutions were set at the steady state (4.3), perturbed randomly by $\pm 5\%$. The system was solved numerically on the domain $0 < x < 500$ using a semi-implicit finite difference method with periodic boundary conditions at both ends; we chose a grid spacing of $dx = 0.5$ and a time step of $dt = 0.001$ so that the CFL condition $dt \leq dx^2/(2D_O)$ is satisfied.

simulations did not yield periodic travelling waves; however, (stationary) spatial patterns were found. These stationary patterns occur via a Turing bifurcation (see Section 1.1 for a discussion on Turing patterns). In Figure 4.41, we plot the stationary spatial pattern obtained for $R = 1.1$ through PDE simulations.

4.9 Discussion

In this chapter, we have investigated banded vegetation patterns in semi-deserts. We have studied the existence and stability of these patterns by using the Rietkerk model (2002). Since the limiting resource in these ecosystems is water, these pattern solutions depend greatly on annual rainfall and we have seen how they vary when rainfall changes. These results indicate that environmental changes affect vegetation patterns. As one would expect, as rainfall changes, the average plant density also changes; vegetation patterns however conserve their wavelength until the rainfall value crosses a stability threshold. This means

that the wavelength and other properties of the vegetation patterns seen around the world vary in a history dependent manner. This dependence has been previously reported in other studies of patterns in semi-arid vegetation and in other landscape-scale patterns; for example, Sherratt (2013), Sherratt & Lord (2007) demonstrated the existence of history-dependence for patterns in banded vegetation in semi-arid environments using the simpler Klausmeier model and also for patterns in young mussel beds. A possible future project would be to investigate history-dependence in other models for semi-arid vegetation patterns. Two main such models are those introduced by Lefever & Lejeune (1997) and Gilad et al. (2007). Gilad et al.'s (2007) model consists of PDE equations corresponding to the three dynamical variables P (plant density), W (soil water density) and O (surface water density); the main difference with the Rietkerk model is that, here, the rate of plant growth and that of soil water infiltration are nonlocal functions of the model variables. The Lefever & Lejeune's (1997) model consists of a single kinetic equation for plant density where both the rates of plant growth and of plant death are nonlocal functions of the model variables. These integro-differential equations make the Gilad et al.'s model, and the Lejeune and Lefever's model difficult to study: analytical investigation would be complicated and numerical integration is costly in terms of computer time. However, Lejeune and Lefever provide an approximation of their model by a partial differential equation (Lefever & Lejeune 1997); this could be investigated in PDE simulations and `WAVETRAIN`.

Vegetation patterns in semi-deserts have arisen in many different parts of the globe. One potential application of studying these patterns is that lessons could be learnt from this 'survival mechanism' seen in vegetation that grows in difficult environmental conditions. These patterns could possibly form the basis for improved approaches to growing crops in regions affected by droughts or could possibly be used to improve harvest even in regions with relatively favourable environmental conditions. For instance, farmers might obtain better results by growing crops in a patterned way instead of uniform planting.

Part IV

Absolute Instability vs Convective Instability of a Nonhomogeneous Steady State and Conclusion

Chapter 5

On the Absolute and Convective Instabilities of Spatially-Varying Solutions

5.1 Introduction

The mathematical concept of stability is the same in both temporal and spatiotemporal systems: a solution is locally stable when any small perturbation decays. However in spatiotemporal systems, the story does not end there: an unstable solution can either be convectively unstable or absolutely unstable. In the first case, the perturbation may decay at which it is applied, even though it is growing over all. In contrast, a solution is absolutely unstable when there are perturbations growing at the location at which they are applied. Using the classical example of Turing pattern formation, we first started this thesis by introducing the concept of stability of homogeneous steady states in spatiotemporal systems (Chapter 1). We investigated the homogeneous steady state case further in Chapters 2 and 3 where we explore absolute and convective instabilities arising in a predator-prey invasion scenario. Then in Chapter 4, we move on to investigate the stability of periodic travelling wave solutions of a PDE system for banded vegetation patterns in arid/semiarid ecosystems, the Rietkerk et al.'s (2002) model. In this brief chapter, we revisit periodic travelling wave solutions of the Rietkerk model (4.1), and we discuss absolute and convective instabilities.

5.2 Absolute and Convective Instabilities of a Periodic Travelling Wave

Let us consider a reaction-diffusion system

$$U_t = DU_{xx} + F(U), \tag{5.1}$$

with $U \in \mathbb{R}^N$. With a change of variable $z = x - ct$, (5.1) becomes

$$U_t = DU_{zz} + cU_z + F(U) \tag{5.2}$$

Solutions to the ODE

$$DU_{zz} + cU_z + F(U) = 0 \tag{5.3}$$

are steady states of (5.2) and are called periodic travelling waves if $U(z + L) = U(z)$ for all z and some $L > 0$. In this chapter, we are interested in the absolute and convective instabilities of such solutions.

5.2.1 Calculation of the Generalised Absolute Spectrum

Let U^* be a periodic travelling wave solution of (5.1). Linearising (5.2) about U^*, we obtain the operator

$$\mathcal{L} := D\partial_{zz} + c\partial_z + a(z), \tag{5.4}$$

where $a(z) = \partial_U F(U^*)$. The eigenvalue problem

$$\mathcal{L}U = DU_{zz} + cU_z + a(z)U = \lambda U \tag{5.5}$$

is equivalent to

$$V_z = A(z, \lambda)V, \tag{5.6}$$

where $V = (U, U_z)$ and

$$A(\lambda) = \begin{pmatrix} 0 & Id \\ D^{-1}\lambda - D^{-1}a(z) & -D^{-1}c \end{pmatrix} \tag{5.7}$$

Since U^* is a periodic travelling wave, this matrix has periodic coefficients. Floquet theory states that the evolution of linear time-varying differential equations with periodic coefficients can be represented as the product of a periodic matrix and an exponential matrix containing the so-called 'Floquet exponents'. Let $\phi_\lambda(z,t)$ denote the evolution of (5.6). Then it has a Floquet representation with L-periodic matrix $S_\lambda(z)$ ($S_\lambda(0) = Id$) of the form

$$\phi_\lambda(z,0) = S_\lambda(z)e^{(R(\lambda)z)}. \tag{5.8}$$

Definition Similarly to the homogeneous steady state case (Chapters 2 and 3), we need the dispersion relation in order to compute the generalised absolute spectrum. Here this relation is defined by

$$d(\lambda,\nu) = \det(R(\lambda) - \nu) = 0. \tag{5.9}$$

- A branch point $\lambda \in \mathbb{C}$ at $\nu \in \mathbb{C}$ satisfies $d(\lambda,\nu) = \partial_\nu d(\lambda,\nu) = 0$.
- Eigenvalues $\nu(\lambda)$ of $R(\lambda)$ are called spatial Floquet exponents.
- The essential spectra $\sum_{ess}$ is the set of λ's such that $\exists k \in \mathbb{R} : d(\lambda, ik) = 0$
- The generalised absolute spectrum of Morse index j is

$$\sum\nolimits_{abs}^{j} := \{\lambda \in \mathbb{C} | Re(\nu_j) = Re(\nu_{j+1})\}.$$

- The absolute spectrum is the generalised absolute spectrum of Morse index N, where N is the number of equations.

The calculation of the generalised absolute spectrum as defined above is very complicated; the problem lies in the fact that branch points (starting solutions) are hard to find. Recall that in the case of homogeneous steady states in the Rosenzweig & Macarthur (1963) model, we showed through examples that to determine absolute stability in the, we do not need to compute the entire absolute spectrum and absolute stability is then easily determined only by considering the real parts of the branch points. Luckily, for spatially varying steady states, Rademacher (2006) discusses a special case where we can determine absolute instability without computing the absolute spectrum. Indeed, let Ω_∞ denote the connected component of $\mathbb{C} \setminus \sum_{ess}$ that contains an unbounded interval of $\mathbb{R}_+$. Let us assume that the essential spectrum contains an isola ι. Then according to Rademacher (2006), if $\iota \in \partial\Omega_\infty$ then ι contains parts of the absolute spectrum. The steady state is then absolutely stable if $Re(\lambda) < 0,\ \forall\lambda \in \iota$ and is absolutely unstable if $Re(\lambda) > 0,\ \forall\lambda \in \iota$. In the previous chapter, we have shown various pictures of essential

spectra for different periodic travelling wave solutions of the Rietkerk model. Based on the results in Rademacher (2006), a few of these waves are absolutely unstable; that is the case, for example, of the six waves *wave*1, *wave*2, ..., *wave*6 shown in Figure 4.12a along with their essential spectra in Figure 4.12b. We recall these pictures below in Figure 5.1.

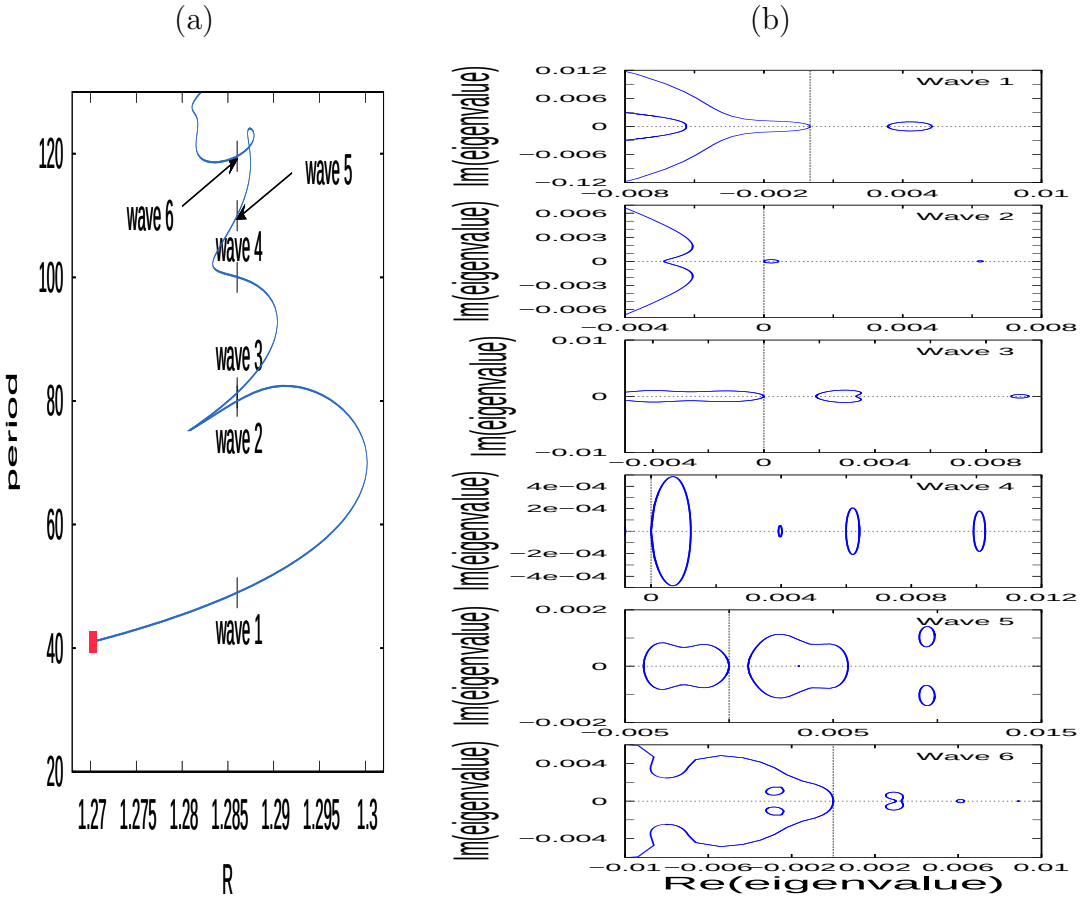

Figure 5.1: Panel (a): bifurcation diagram at $c = 0.02$. We truncated the solution branch to show waves of wavelength between 20 and 130 and in this range, there are six different waves *wave*1, *wave*2, ..., *wave*6 at the R value 1.286. Panel (b): eigenvalue spectra of *wave*1, *wave*2, ..., *wave*6. Each of these spectra has at least one isola in $\partial\Omega_\infty \cap \mathbb{R}_+ \times \mathbb{R}$; therefore, *wave*1, *wave*2, ..., *wave*6 are all absolutely unstable.

In the next section, we investigate the dynamics of an absolutely unstable periodic travelling wave.

5.2.2 Perturbing an Absolutely Unstable Periodic Travelling Wave

Here we would like to explore how an absolutely unstable periodic travelling wave is affected by small perturbations. The fact that all six waves shown on the bifurcation diagram in Figure 5.1 are absolutely unstable suggests that all the waves along this solution branch are absolutely unstable. We would like to run simulations on the domain $(0, 200)$ and we choose the wave $U_{abs} = (P_{abs}, W_{abs}, O_{abs})$ along this solution branch that has period 50 so that the wave number is four; it corresponds to the rainfall parameter $R = 1.287$ and is also absolutely unstable (Figure 5.2).

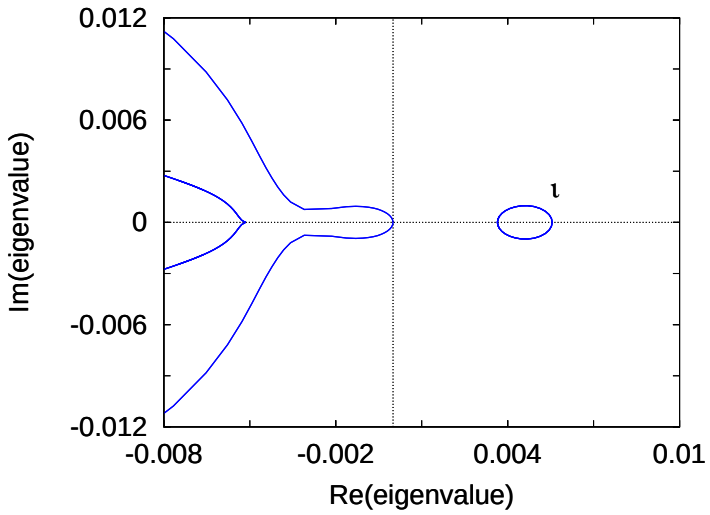

Figure 5.2: Essential spectra $\sum_{ess}$ of an unstable wave at $(R, c) = (1.287, 0.02)$. One of the curves in $\sum_{ess}$ is the isola ι which is included in $\partial\Omega_\infty$, therefore it contains absolute spectrum. Moreover $\forall\lambda \in \iota$, $Re\lambda \in \mathbb{R}_+$, hence the wave is absolutely unstable.

Setting the initial solution at U_{abs}, we first run PDE simulations of the Rietkerk equations (4.1) without adding any perturbation to U_{abs} and we notice that the amplitude of the PDE solution slowly decreases over time and collapses at the steady state (P_2, W_2, O_2) after $t = 6000$; for this reason, to study how perturbations vary as time increases, we limit our simulations to the time range $(0, 100)$. We denote by U_{unpert} the PDE solution obtained in the absence of perturbations. For t in the same time interval, we then perturbed the initial solution by an increase of 10% in the water densities W_{abs} and O_{abs} for $x \in (95, 105)$ and we denote the PDE result of this simulation by U_{pert}. Results for the plant density are shown in Figure 5.3 and illustrate how perturbations vary as the time t variable increases. The PDE solutions U_{unpert} and U_{pert} are shown in

the first and second columns respectively. The difference $U_{pert} - U_{unpert}$ gives the perturbations to the absolutely unstable solution U_{abs} (third column). Solutions are shown for $t = 0,\ 5,\ 10,\ 20,\ 40,\ 70$ and 100 and we see that without moving the initial perturbation grows.

To see the long-term behaviour of the solution U_{pert}, we carried our PDE simulations with perturbations for longer time intervals; solutions are shown on Figure 5.4. On panels (e)-(g), we see that the homogeneous steady state P_2 exists as long-term transients of the solution. We obtain similar results when we perturb the water densities W_{abs} and O_{abs}: the unstable steady state (P_2, W_2, O_2) becomes dynamically stabilised.

The above results show that perturbing an absolutely unstable spatially varying solution can yield dynamical stabilisation of an unstable homogeneous steady state; this is similar to the homogeneous steady state case studied in Chapters 2 and 3. Next, we would like to know if perturbed convectively unstable waves also exhibit any form of stabilisation.

5.2.3 Perturbation a Convectively Unstable Periodic Travelling Wave

Contrary to the absolutely unstable case, we do not know how to tell, from looking at the spectrum of an unstable wave, if the wave is convectively unstable or not. For our simulations in this section we simply chose an unstable solution U_{conv} with no isola in its essential spectrum; it has a period = 50 and is located at $(R, c) = (1.08, 0.028)$ (see Figure 5.5 for the spectrum).

We define U_{unpert} and U_{pert}, and calculate the perturbations as described in the previous section; here the water densities are pertubed by an increase of 10% at the location $x = 100$. In the absence of perturbations, U_{conv} travels across the domain as time increases and does not collapse at U_2, as U_{abs} did. We first run our simulations for increasing time ranges $t \in (0, 10000)$ and the solutions show that the initial perturbation moves away from $x = 100$: this means that the solution U_{conv} is convectively unstable. We then did simulations for bigger t values and at time 1500000, we obtained a periodic travelling wave solution of period 63.333 (200/3) (Figure 5.7); its speed is estimated about 0.0385. Further PDE simulations reveal that this new wave is stable; moreover, computations in `WAVETRAIN` confirm that the wave located at $(R, c) = (1.08, 0.0385)$ is stable and its period is 63.36.

We conclude that perturbing an unstable pattern solution could yield a stable pattern of different wavelength and speed. We have seen many examples of this switch from

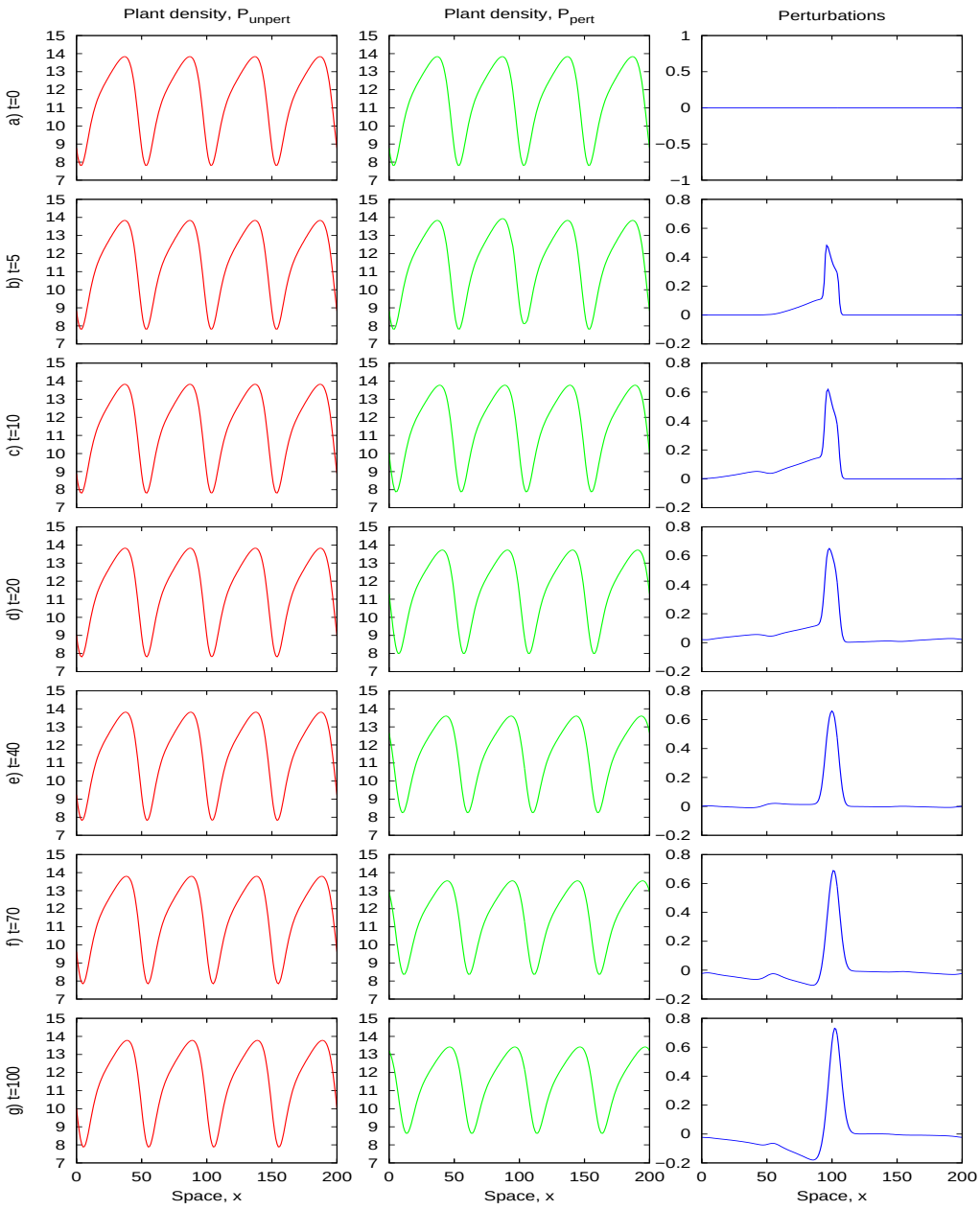

Figure 5.3: Illustration of the dynamics of the perturbations in the plant density P_{abs}. The absolutely unstable solution $U_{abs} = (P_{abs}, W_{abs}, O_{abs})$ at $(R, c) = (1.287, 0.02)$ was perturbed by an increase of 10% in the water densities W_{abs} and O_{abs} for $x \in (95, 105)$. The first column shows solutions in the absence of perturbations while the second column shows solutions after perturbations have been added. The third column, which is the difference between the first two, represents the perturbations. As time increases, the initial perturbations grow at the site of perturbation. Similar simulations results were obtained for the water densities W_{abs} and O_{abs}. These results confirm that the wave U_{abs} is absolutely unstable.

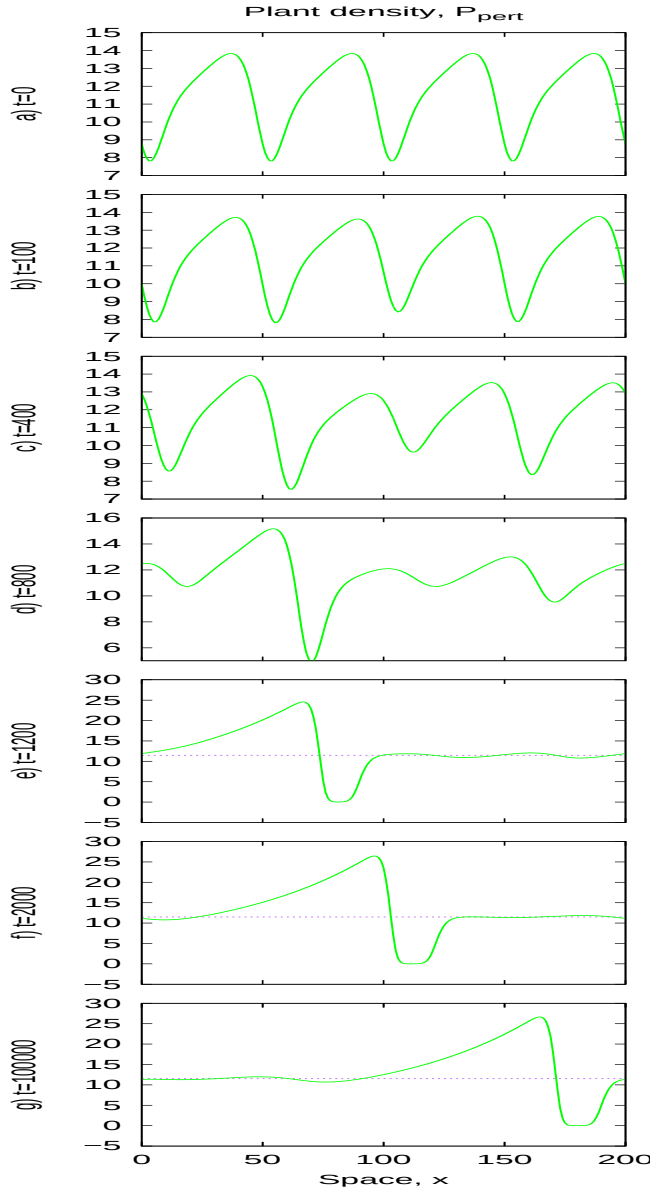

Figure 5.4: Numerical simulations of the Rietkerk model (4.1) for the plant density P_{abs} following a small perturbation to the absolutely unstable wave $U_{abs} = (P_{abs}, W_{abs}, O_{abs})$ at $(R, c) = (1.287, 0.02)$. We plot in purple the line $P = P_2 \simeq 11.5$; on panels (e)-(g), we see that the homogeneous steady state P_2 exists as long-term transients of the solution. We obtained similar results when we perturbed the water densities W_{abs} and O_{abs}: the unstable steady state (P_2, W_2, O_2) became dynamically stabilised. The initial condition was $U_0 = 110\% U_{abs}$ for $x \in (95, 105)$ and $U_0 = U_{abs}$ otherwise. The equations were solved numerically with a finite-difference scheme, on $0 < x < 200$ with periodic boundary conditions at both ends.

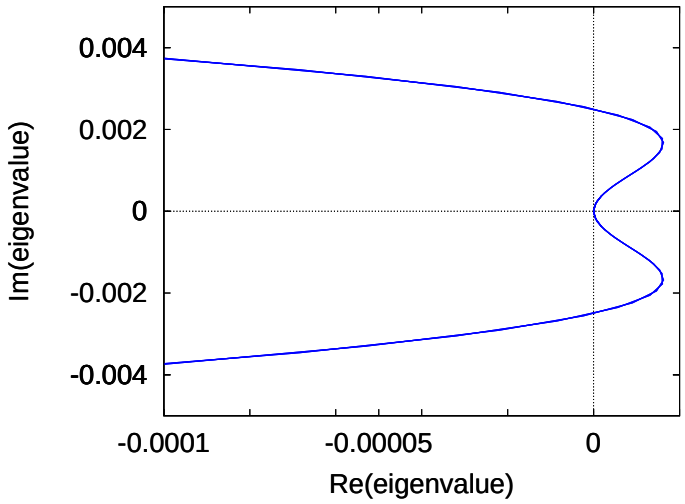

Figure 5.5: Essential spectra $\sum_{ess}$ of the unstable wave of period 50 at $(R, c) = (1.08, 0.028)$.

unstable solution to stable solution earlier in Chapter 4 when we investigated the effect that a change in rainfall could have on vegetation patterns (Figures 4.24-4.27 and 4.29-4.34).

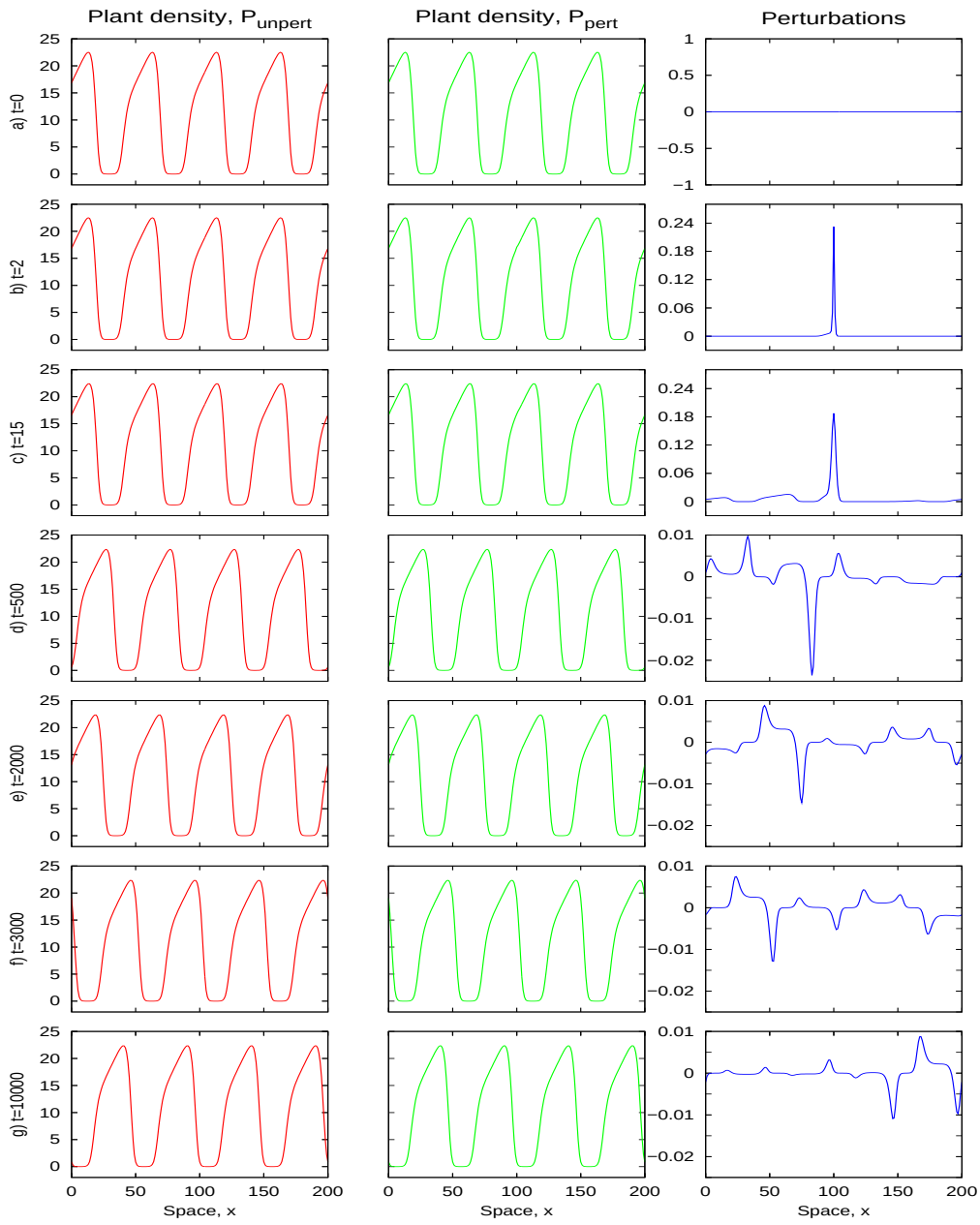

Figure 5.6: Numerical simulations of the Rietkerk model (4.1) for the plant density following a small perturbation to the unstable wave U_{conv} of period 50 at $(R, c) = (1.08, 0.028)$ which spectrum is shown on Figure 5.5. This wave is locally perturbed by an increase of 10% in the water densities at $x = 100$. The first column shows PDE solutions in the absence of perturbations, the second column shows solutions in the presence of perturbations while the third shows the dynamics of the perturbations; these perturbations move away from the site of perturbation $x = 100$ implying that the solution U_{conv} is convectively unstable. The equations were solved numerically with a finite-difference scheme, on $0 < x < 200$ with periodic boundary conditions at both ends.

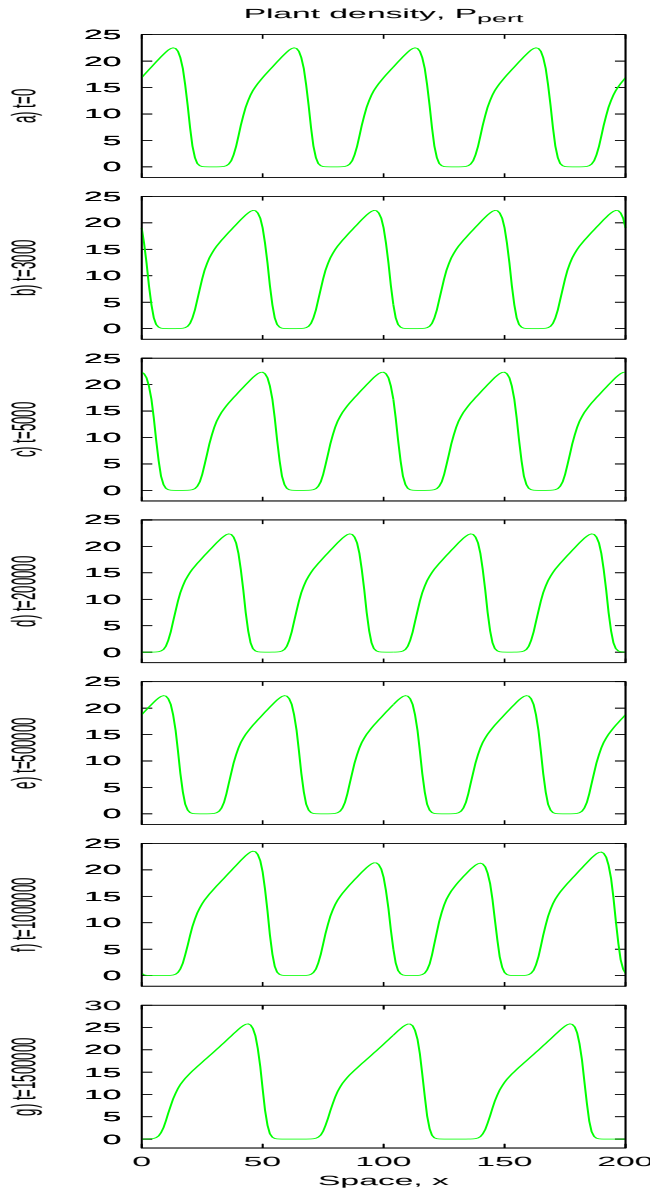

Figure 5.7: Numerical simulations of the Rietkerk model (4.1) for the plant density P_{conv} following a small perturbation to the convectively unstable wave $U_{conv} = (P_{conv}, W_{conv}, O_{conv})$ at $(R, c) = (1.08, 0.028)$. As perturbations grow throughout the domain, P_{conv} evolves into a stable periodic travelling wave at time 1500000. The equations were solved numerically with a finite-difference scheme, on $0 < x < 200$ with periodic boundary conditions at both ends.

5.3 Conclusion

In this chapter, we defined the concept of absolute and convective instability for periodic travelling waves. We then selected and perturbed two periodic travelling wave solutions; one, absolutely unstable and the other, convectively unstable. In the absolutely unstable case, dynamical stabilisation of the unstable homogeneous steady state U_2 occurred while in the convectively unstable case, we obtained a new pattern solution that is stable.

Chapter 6

Conclusion

Our mathematical journey in the course of this thesis work took us through two important real life ecological phenomena: the invasion of a population by its predators and self-organisation of vegetation in water-limited ecosystems into banded patterns. Even though these may sound like two different topics, all the results in this research work point to one conclusion: unstable solutions to a given PDE are not automatically insignificant. We have investigated unstable PDE solutions in each of the previous chapters as follows:

• In Chapters 2 and 3, we used the Rosenzweig & Macarthur (1963) model for predator-prey interaction to study ecological invasion. We focussed on the existence of the coexistence steady state as spatiotemporal transient (dynamical stabilisation). We used the concepts of absolute and convective instabilities to understand this type of stabilisation and calculated its extent; we then studied the effect that variations in ecological parameters have on the width of the stabilised region.

• In Chapter 4, we investigated banded vegetation patterns in semi-deserts using the Rietkerk et al. (2002) model. We performed a systematic study of the existence and stability of pattern solutions. Investigating the effects of rainfall variation on vegetation patterns showed that a small change in rainfall at an unstable periodic travelling wave can yield a stable periodic travelling wave; this result is very significant ecologically as it suggests that unstable vegetation patterns can become stable thanks to environmental changes. We also classified patterns into those that are unstable/stable for different values of the soil gradient and of the surface water dispersion.

• It would have been interesting to classify the unstable patterns into those that are

convectively unstable/absolutely unstable. Unfortunately the numerical procedures currently available to distinguish convective and absolute instabilities for spatially-varying solutions apply only to very special types of partial differential equations that do not include the Rietkerk model. However, it is known that if the spectrum of the pattern contains an isola to the right of its unbounded part and in the right-hand half of the complex plane, then the solution is absolutely unstable Rademacher (2006). We found that both types of instability do occur in the Rietkerk model.

In Chapter 5, we see that perturbations to an absolutely unstable pattern solution of the Rietkerk model can yield a solution where the (homogeneous) vegetated steady state exists as long-term transient; this dynamical stabilisation result is similar to that for the homogeneous steady state case seen in Chapters 2 and 3.
We also perturbed a convectively unstable pattern solution of the model and this evolved into a stable pattern with new characteristics (wavelength, speed, amplitude). This is similar to the results we obtained in Chapter 4 when we investigated the history-dependence of the patterns.

Future Directions In our investigation of dynamical stabilisation in Chapters 2 and 3, we have focussed on the existence and extent of the coexistence steady state as a spatiotemporal transient. The invasion of a prey population by predators can also involve other spatiotemporal transients. For example, periodic travelling waves may develop and move in the opposite direction to the invasion. In the future, we could investigate this phenomena using the same methodology as in Chapters 2 and 3. However, there is one very fundamental practical difficulty: identifying appropriate starting points for the numerical continuation of the absolute spectrum for non-constant solutions is very complicated.

In the case of vegetation patterns, a project of interest would be to investigate history-dependence in the Lefever & Lejeune (1997) and Gilad et al. (2007) models. Also the results in Sections 5.2.2 and 5.2.3 raised an interesting question: in our results on the effects of varying rainfall on pattern solutions in Section 4.7, we saw that a small change in rainfall can make an unstable pattern solution evolve into a stable pattern solution. In the figure below, we recall simulation results for the case where the initial solution has a wavelength $= 50$. This solution is stable and corresponds to $(R, c) = (0.83, 0.025)$. As R decreases, the pattern solutions maintain the same wavelength until an unstable solution is found at the location $(R, c) = (0.64, 0.0133)$ (shown with a blue dot).

A change in rainfall at this location yields a stable pattern solution. This is similar to the results in Section 5.2.3 where local perturbations to a convectively unstable periodic

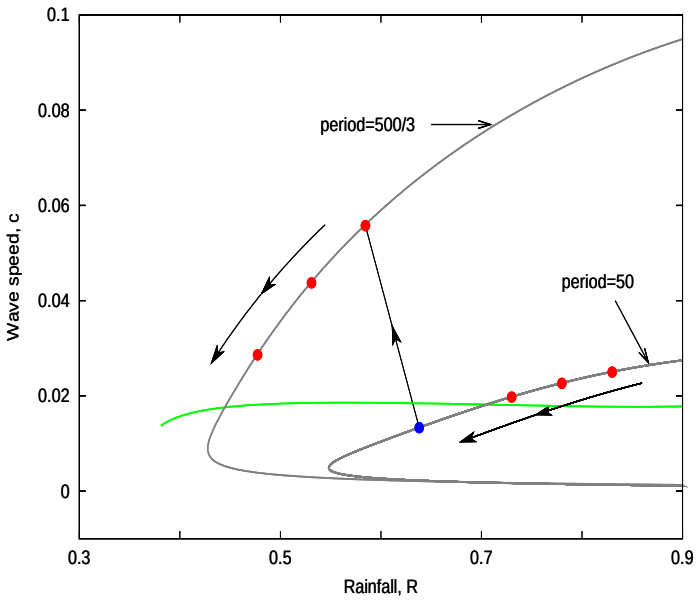

Numerical solutions of (4.1) solved with a wave initially on the period contour of period 50. The red dots represent the wavelength and speed of stable pattern solutions while the blue dot represents the wavelength and speed of an unstable pattern solution. Arrows indicate the direction of variations in rainfall. A change in rainfall at the unstable wave yields a stable wave.

travelling wave yield a stable periodic travelling wave. This suggests that the unstable periodic travelling waves in the rainfall variation investigation (see Figures 4.24-4.27 and 4.29-4.34) might all be convectively unstable. Furthermore, the essential spectrum of each of these waves is similar to that in Figure 5.5. A topic of interest for the future is to investigate the type of instability in these waves. If indeed they are all convectively unstable, a question then is how an absolutely unstable pattern solution evolves after a change in rainfall; and if (similarly to the example in Section 5.2.2) it does not yield a new pattern solution, what are the ecological implications for banded vegetation patterns in water-limited ecosystems?

References

Anderson, K. E., Hilker, F. M. & Nisbet, R. M. (2012), 'Directional Dispersal and Emigration Behavior Drive a Flow-Induced Instability in a Stream Consumer-Resource Model', *Ecol. Lett.* **15**, 209–217.

Anderson, K. E., Nisbet, R. M., Diehl, S. & Cooper, S. D. (2005), 'Scaling Population Responses to Spatial Environmental Variability in Advection-Dominated Systems', *Ecol. Lett.* **8**, 933–943.

Anderson, K. E., Paul, A. J., McCauley, E., Jackson, L. J., Post, J. R. & Nisbet, R. M. (2006), 'Instream Flow Needs in Streams and Rivers: the Importance of Understanding Ecological Dynamics', *Front. Ecol. Environ.* **4**, 309–318.

Aranson, I. S., Aranson, L., Kramer, L. & Weber, A. (1992), 'Stability Limits of Spirals and Traveling Waves in Nonequilibrium Media', *Phys. Rev. A* **46**, 2992–2995.

Aranson, I. S. & Kramer, L. (2002), 'The World of the Complex Ginzburg-Landau Equation', *Rev. Modern Phys.* **74**, 99–143.

Armstrong, R. A. & McGehee, R. (1980), 'Competitive Exclusion', *Am. Nat.* **115**, 151–170.

Beard, J. S. (1967), 'A Study of Patterns in some West Australian Heath and Mallee Communities', *Australian Journal of Botany* **15**, 131–139.

Belsky, A. J. (1994), 'Influences of Trees on Savanna Productivity: Tests of Shade, Nutrients and Tree-Grass Competition', *Ecology* **75**, 922–932.

Bernd, J. (1978), 'The Problem of Vegetation Stripes in Semi-Arid Africa', *Plant Research and Development* **8**, 37–50.

Bertness, M. D. & Grosholz, E. (1985), 'Population-Dynamics of the Ribbed Mussel *geukensi demissa* – the Costs and Benefits of an Aggregated Distribution', *Oecologia* **67**, 192–204.

Beyn, W.-J. & Lorenz, J. (1999), 'Stability of Travelling Waves: Dichotomies and Eigenvalue Conditions on Finite Intervals', *Numer. Funct. Anal. Opt.* **20**, 201–244.

Biancofiore, L., Gallaire, F. & Pasquetti, R. (2011), 'Influence of Confinement on a Two-Dimensional Wake', *J. Fluid Mech.* **688**, 297–320.

Brevdo, L. (1988), 'A Study of Absolute and Convective Instabilities with an Application to the Eady Model', *Geophys. Astrophys. Fluid Dyn.* **40**, 1–92.

Brevdo, L. (1995), 'Convectively Unstable Wave Packets in the Blasius Boundary Layer', *Z. Angew. Math. Mech.* **75**, 423–436.

Brevdo, L. & Bridges, T. J. (1996), 'Absolute and Convective Instabilities of Spatially Periodic Flows', *Phil. Trans. R. Soc. Lond. A* **354**, 1027–1064.

Brevdo, L. & Bridges, T. J. (1997), 'Absolute and Convective Instabilities of Temporally Oscillating Flows', *Z. Angew. Math. Phys.* **48**, 290–309.

Brevdo, L., Laure, P., Dias, F. & Bridges, T. J. (1999), 'Linear Pulse Structure and Signalling in a Film Flow on an Inclined Plane', *J. Fluid Mech.* **396**, 37–71.

Briggs, R. J. (1964), *Electron-Stream Interaction with Plasmas*, Cambridge, USA: MIT Press.

Chomaz, J. M. (2004), 'Transition to Turbulence in Open Flows: what Linear and Fully Nonlinear Local and Global Theories Tell us', *Eur. J. Mech. B* **23**, 385–399.

Chomaz, J. M. (2005), 'Global Instabilities in Spatially Developing Flows: non-Normality and Nonlinearity', *Ann. Rev. Fluid Mech.* **37**, 357–392.

Clos-Arceduc, M. (1956), 'Etudes sur Photographies Aériennes d'une Formation Végétale Sahélienne: la Brousse Tigrée', *Bull. Inst. Afr. noire. Sér A* **18**, 677–684.

Cooper, S. D., Diehl, S., Kratz, K. & Sarnelle, O. (1998), 'Implications of Scale for Patterns and Processes in Stream Ecology', *Austral. J. Ecol.* **23**, 27–40.

Dagbovie, A. S. & Sherratt, J. A. (2013), 'Absolute Stability and Dynamical Stabilisation in Predator-Prey Systems', *J. Math. Biol* . accepted. **doi 10.1007/s00285-013-0672-8**.

Dunbar, S. R. (1984), 'Travelling Wave Solutions of Diffusive Lotka-Volterra Equations: a Heteroclinic Connection in R^4', *Trans. Am. Math. Soc.* **268**, 557–594.

Dunbar, S. R. (1986), 'Traveling Waves in Diffusive Predator-Prey Equations – Periodic Orbits and Point-to-Periodic Heteroclinic Orbits', *SIAM J. Appl. Math.* **46**, 1057–1078.

Dyczkowski, J. & Yalden, D. W. (1998), 'An Estimate of The Impact of Predators on the British Field Vole *microtus agrestis* Population', *Mammal Rev.* **28**, 165–184.

Fausch, K. D., Torgersen, C. E., Baxter, C. V. & Li, H. W. (2002), 'Landscapes to Riverscapes: Bridging the Gap between Research and Conservation of Stream Fishes', *BioScience* **52**, 483–498.

Foster, D. R., King, G. A., Glaser, P. H. & Jr, H. E. W. (1983), 'Origin of String Patterns in Boreal Peatlands', *Nature* **306**, 256–258.

Fox, P. J. & Proctor, M. R. E. (1998), 'Effects of Distant Boundaries on Pattern Forming Instabilities', *Phys. Rev. E* **57**, 491–494.

Fraile, J. M. & Sabina, J. C. (1989), 'General Conditions for the Existence of a Critical Point–Periodic Wave Front Connection for Reaction-Diffusion Systems', *Nonlinear Analysis – Theory, Methods, Appl.* **13**, 767–786.

Garvie, M. R. (2007), 'Finite Difference Schemes for Reaction-Diffusion Equations Modeling Predator-Prey Interactions in MATLAB', *Bull. Math. Biol.* **69**, 931–956.

Gilad, E., von Hardenberg, J., Provenzale, A., Shachak, M. & Meron, E. (2007), 'A Mathematical Model of Plants as Ecosystem Engineers', *J. Theor. Biol.* **244**, 680–691.

Graham, I. M. & Lambin, X. (2002), 'The Impact of Weasel Predation on Cyclic Field-Vole Survival: the Specialist Predator Hypothesis Contradicted', *J. Anim. Ecol.* **71**, 946–956.

Greig-Smith, P. (1979), 'Patterns in Vegetation', *J. Ecol.* **67**, 755–779.

Grimm, V. & Wissel, C. (1997), 'Babel, or the Ecological Stability Discussions: an Inventory and Aanalysis of Terminology and a Guide for Avoiding Confusion', *Oecologia* **109**, 323–334.

Hellmann, J. J., Byers, J. E., Bierwagen, B. G. & Dukes, J. S. (2008), 'Five Potential Consequences of Climate Change for Invasive Species', *Cons. Biol.* **22**, 534–543.

Hiemstra, C. A., Liston, G. E. & Reiners, W. A. (2002), 'Snow Redistribution by Wind and Interactions with Vegetation at Upper Treeline in Medicine Bow Mountains, Wyoming, USA', *Arct. Antarct. Alp. Res.* **34**, 262–273.

Hiemstra, C. A., Liston, G. E. & Reiners, W. A. (2006), 'Observing, Modelling, and Validating Snow Redistribution by Wind in a Wyoming Upper Treeline Landscape', *Ecol. Modelling* **197**, 35–51.

Hilker, F. M. & Lewis, M. A. (2010), 'Predator-Prey Systems in Streams and Rivers', *Theor. Ecol.* **3**, 175–193.

HilleRisLambers, R., Rietkerk, M., van de Bosch, F., Prins, H. H. T. & de Kroon, H. (2001), 'Vegetation Pattern Formation in Semi-Arid Grazing Systems', *Ecology* **82**, 50–61.

Huerre, P. & Monkewitz, P. A. (1990), 'Local and Global Instabilities in Spatially Developing Flows', *Ann. Rev. Fluid Mech.* **22**, 473–537.

Huisman, J. & Weissing, F. J. (1999), 'Biodiversity of Plankton by Species Oscillations and Chaos', *Nature* **402**, 407–410.

King, C. M. (1989), *The Natural History of Weasels and Stoats*, Christoper Helm.

Klausmeier, C. A. (1999), 'Regular and Irregular Patterns in Semiarid Vegetation', *Science* **284**, 1826–1828.

Kopell, N. & Howard, L. N. (1973), 'Plane Wave Solutions to Reaction-Diffusion Equations', *Stud. Appl. Math.* **52**, 291–328.

Korpimäki, E. & Norrdahl, K. (1998), 'Experimental Reduction of Predators Reverses the Crash Phase of Small-Rodent Cycles', *Ecology* **79**, 2448–2455.

Korpimäki, E., Norrdahl, K., Klemola, T., Pettersen, T. & Stenseth, N. C. (2002), 'Dynamic Effects of Predators on Cyclic Voles: Field Experimentation and Model Extrapolation', *Proc. R. Soc. Lond. B* **269**, 991–997.

Lee, S.-H. (2012), 'Effects of Uniform Rotational Flow on Predator–Prey System', *Phys. A* **391**, 6008–6015.

Lefever, R. & Lejeune, O. (1997), 'On the Origin of Tiger Bush', *Bull. Math. Biol.* **59**, 263–294.

Lejeune, O., Tlidi, M. & Couteron, P. (2002), 'Localized Vegetation Patches: a Self-Organized Response to Resource Scarcity', *Phys. Rev. E* **66**, 010901.

Levine, J. M. (2003), 'A Patch Modeling Approach to the Community-Level Consequences of Directional Dispersal', *Ecology* **84**, 1215–1224.

Liu, Q.-X., Weerman, E. J., Herman, P. M. J., Olff, H. & van de Koppel, J. (2012), 'Alternative Mechanisms Alter the Emergent Properties of Self-Organization in Mussel Beds', *Proc. R. Soc. Lond. B* **279**, 2744–2753.

Lotka, A. J. (1925), *Elements of Physical Biology*, Williams and Wilkins, Baltimore.

Lutscher, F., Lewis, M. A. & McCauley, E. (2006), 'Effects of Heterogeneity on Spread and Persistence in Rivers', *Bull. Math. Biol.* **68**, 2129–2160.

MacFadyan, W. A. (1950*a*), 'Soil and Vegetation in British Somaliland', *Nature* **165**, 121.

MacFadyan, W. A. (1950*b*), 'Vegetation Patterns in Semi-Desert Plains of British Somaliland', *The Geographical Journal* **116**, 199–211.

Malchow, H. (2000), 'Motional Instabilities in Predator-Prey Systems', *J. Theor. Biol.* **204**, 639–647.

Malchow, H. & Petrovskii, S. V. (2002), 'Dynamical Stabilization of an Unstable Equilibrium in Chemical and Biological Systems', *Math. Comput. Model.* **36**, 307–319.

Malchow, H., Petrovskii, S. V. & Venturino, E. (2008), *Spatiotemporal Patterns in Ecology and Epidemiology*, Chapman & Hall/CRC, Boca Raton.

Matsumura, C., Yokoyama, Y. & Washitani, I. (2004), 'Invasion Status and Potential Ecological Impacts of an Invasive Alien Bumblebee, Bombus terrestris L. (Hymenoptera: Apidae) Naturalized in Southern Hokkaido, Japan', *Glob. Environ. Res.* **8**, 51–66.

May, R. M. & Mclean, A. R. (2007), *Theoretical Ecology: Principles and Applications*, Oxford University Press, Oxford.

McDonald, R. A. & Harris, S. (2002), 'Population Biology of Stoats Mustela erminea and Weasels Mustela nivalis on Game Estates in Great Britain', *J. Appl. Ecol.* **39**(5), 793–805.

Merchant, S. M. & Nagata, W. (2010), 'Wave Train Selection behind Invasion Fronts in Reaction-Diffusion Predator-Prey Models', *Phys. D* **239**, 1670–1680.

Merchant, S. M. & Nagata, W. (2011), 'Instabilities and Spatiotemporal Patterns behind Predator Invasions with Nonlocal Prey Competition', *Theor. Pop. Biol.* **80**, 289–297.

Morozov, A. Y., Petrovskii, S. V. & Li, B.-L. (2006), 'Spatiotemporal Complexity of the Patchy Invasion in a Predator-Prey System with the Allee Effect', *J. Theor. Biol.* **238**, 18–35.

Nauman, E. B. (2008), *Chemical Reactor Design, Optimization, and Scaleup (2nd ed.)*, Wiley, Hoboken, NJ, USA.

Norrdahl, K. & Korpimäki, E. (2002), 'Changes in Population Structure and Reproduction During a 3-yr Population Cycle of Voles', *OIKOS* **96**(2), 331–345.

Nozaki, K. & Bekki, N. (1983), 'Pattern Selection and Spatiotemporal Transition to Chaos in the Ginzburg-Landau Equation', *Phys. Rev. Lett.* **51**, 2171–2174.

Oli, M. K. (2003), 'Population Cycles of Small Rodents Are Caused by Specialist Predators: or Are They?', *Trends Ecol. Evol.* **18**, 105–107.

Owen, M. R. & Lewis, M. A. (2001), 'How Predation Can Slow, Stop or Reverse a Prey Invasion', *Bull. Math. Biol.* **63**, 655–684.

Perumpanani, A. J., Sherratt, J. A. & Maini, P. K. (1995), 'Phase Differences in Reaction-Diffusion-Advection Systems and Applications to Morphognesis', *IMA J. Appl. Math.* **55**, 19–33.

Petrovskii, S., Kawasaki, K., Takasu, F. & Shigesada, N. (2001), 'Diffusive Waves, Dynamical Stabilization and Spatio-Temporal Chaos in a Community of Three Competitive Species', *Japan J. Indust. Appl. Math.* **18**, 459–481.

Petrovskii, S., Li, B.-L. & Malchow, H. (2004), 'Transition to Spatiotemporal Chaos Can Resolve the Paradox of Enrichment', *Ecol. Complexity* **1**, 37–47.

Petrovskii, S. V. & Malchow, H. (2000), 'Critical Phenomena in Plankton Communities: KISS Model Revisited', *Nonlinear Analysis: Real World Appl.* **1**, 37–51.

Petrovskii, S. V., Vinogradov, M. E. & Morozov, A. Y. (1998), 'Spatial-Temporal Dynamics of a Localized Populational "Burst" in a Distributed Prey-Predator System', *Okeanologiya* **38**, 881–890.

Rademacher, J. D. M. (2006), 'Geometric Relations of Absolute and Essential Spectra of Wavetrains', *SIAM J. Appl. Dyn. Sys.* **5**, 634–649.

Rademacher, J. D. M., Sandstede, B. & Scheel, A. (2007), 'Computing Absolute and Essential Spectra Using Continuation', *Phys. D* **229**, 166–183.

Reynolds, J. J. H., Massey, F. P., Lambin, X., Reidinger, S., Sherratt, J. A., Smith, M. J., White, A. & Hartley, S. E. (2012), 'Delayed Induced Silica Defences in Grasses and their Potential for Destabilising Herbivore Population Dynamics', *Oecologia* **170**, 445–456.

Rietkerk, M., Boerlijst, M. C., van Langevelde, F., HilleRisLambers, R., van de Koppel, J., Prins, H. H. T. & de Roos, A. (2002), 'Self-Organization of Vegetation in Arid Ecosystems', *Am. Nat.* **160**, 524–530.

Rosenzweig, M. L. & Macarthur, R. H. (1963), 'Graphical Representation and Stability Conditions of Predator-Prey Interactions', *Am. Natur.* **97**, 209–223.

Rovinsky, A. B. & Menzinger, M. (1992), 'Chemical Instability Induced by a Differential Flow', *Phys. Rev. Lett.* **69**, 1193–1196.

Sandstede, B. (2002), 'Stability of Travelling Waves', *In B. Fiedler (Ed.) Handbook of Dynamical Systems II* pp. 983–1055. Amsterdam: North-Holland.

Sandstede, B. & Scheel, A. (2000*a*), 'Absolute and Convective Instabilities of Waves on Unbounded and Large Bounded Domains', *Phys. D* **145**, 233–277.

Sandstede, B. & Scheel, A. (2000*b*), 'Absolute Versus Convective Instability of Spiral Waves', *Phys. Rev. E* **62**, 7708–7714.

Scheuring, I., Károlyi, G., Péntek, A., Tel, T. & Toroczkai, Z. (2000), 'A Model for Resolving the Plankton Paradox: Coexistence in Open Flows', *Freshw. Biol.* **45**, 123–132.

Segel, L. A. & Jackson, J. L. (1972), 'Dissipative Structure: an Explanation and an Ecological Example', *J. Theor. Biol* **37**, 545–559.

Sherratt, J. A. (2001), 'Periodic Travelling Waves in Cyclic Predator-Prey Systems', *Ecol. Lett.* **4**, 30–37.

Sherratt, J. A. (2005), 'An Analysis of Vegetation Stripe Formation in Semi-Arid Landscapes', *J. Math. Biol.* **51**, 183–197.

Sherratt, J. A. (2010), 'Pattern Solutions of the Klausmeier Model for Banded Vegetation in Semi-Arid Environments I', *Nonlinearity* **23**, 2657–2675.

Sherratt, J. A. (2012*a*), 'Numerical Continuation Methods for Studying Periodic Travelling Wave (Wavetrain) Solutions of Partial Differential Equations', *Appl. Math. Computation* **218**, 4684–4694.

Sherratt, J. A. (2012*b*), 'Numerical Continuation of Boundaries in Parameter Space between Stable and Unstable Periodic Travelling Wave (Wavetrain) Solutions of Partial Differential Equations', *Adv. Comput. Math.* . in press.

Sherratt, J. A. (2013), 'History-Dependent Patterns of Whole Ecosystems', *Ecological Complexity* **14**, 8–20.

Sherratt, J. A., Dagbovie, A. S. & Hilker, F. M. (2013), 'A Mathematical Biologist's Guide to Absolute and Convective Instability', *J. Math. Biol* . submitted.

Sherratt, J. A., Eagan, B. T. & Lewis, M. A. (1997), 'Oscillations and Chaos behind Predator-Prey Invasion: Mathematical Artifact or Ecological Reality', *Phil. Trans. R. Soc. Lond. B* **352**, 21–38.

Sherratt, J. A., Lambin, X., Thomas, C. J. & Sherratt, T. N. (2002), 'Generation of Periodic Waves by Landscape Features in Cyclic Predator-Prey Systems', *Proc. R. Soc. Lond. B* **269**, 327–334.

Sherratt, J. A., Lewis, M. A. & Fowler, A. C. (1995), 'Ecological Chaos in the Wake of Invasion', *Proc. Natl. Acad. Sci. USA* **92**, 2524–2528.

Sherratt, J. A. & Lord, G. J. (2007), 'Nonlinear Dynamics and Pattern Bifurcations', *Theor. Pop. Biol.* **71**, 8–20.

Sherratt, J. A. & Smith, M. J. (2008), 'Periodic Travelling Waves in Cyclic Populations: Field Studies and Reaction-Diffusion Models', *J. R. Soc. Interface* **5**, 483–505.

Sherratt, J. A., Smith, M. J. & Rademacher, J. D. M. (2009), 'Locating the Transition from Periodic Oscillations to Spatiotemporal Chaos in the Wake of Invasion', *Phys. D* **106**, 10890–10895.

Smith, M. J., Rademacher, J. D. M. & Sherratt, J. A. (2009), 'Absolute Stability of Wavetrains Can Explain Spatiotemporal Dynamics in Reaction-Diffusion Systems of Lambda-Omega Type', *SIAM J. Appl. Dyn. Syst.* **8**, 1136–1159.

Smith, M. J. & Sherratt, J. A. (2009), 'Propagating Fronts in the Complex Ginzburg-Landau Equation Generate Fixed-Width Bands of Plane Waves', *Phys. Rev. E* **80**. (Art. No. 046209).

Smith, M. J., Sherratt, J. A. & Lambin, X. (2008), 'The Effects of Density-Dependent Dispersal on the Spatiotemporal Dynamics of Cyclic Populations', *J. Theor. Biol.* **254**, 264–274.

Suslov, S. A. (2001), 'Searching Convective/Absolute Instability Boundary for Flows with Fully Numerical Dispersion Relation', *Comput. Fluids* **142**, 322–325.

Suslov, S. A. (2006), 'Numerical Aspects of Searching Convective/Absolute Instability Transition', *J. Comp. Phys.* **212**, 188–217.

Suslov, S. A. (2009), 'Analysis of Instability Patterns in non-Boussinesq Mixed Convection Using a Direct Numerical Evaluation of Disturbance Integrals', *Comput. Fluids* **38**, 590–601.

Suslov, S. A. & Paolucci, S. (2004), 'Stability of non-Boussinesq Convection via the Complex Ginzburg-Landau Model', *Fluid Dyn. Res.* **35**, 159–203.

Tobias, S. M., Proctor, M. R. E. & Knobloch, E. (1998), 'Convective and Absolute Instabilities of Fluid Flows in Finite Geometries', *Phys. D* **113**, 43–72.

Tokarska-Guzik, B., Brock, J. H., Brundu, G., Child, L., Daehler, C. C. & Pysek, P. (2008), *Plant Invasions: Human Perception, Ecological Impacts and Management*, Backhuys, Leiden.

Tongway, D. J. & Ludwig, J. A. (1990), 'Vegetation and Soil Patterning in Semi-Arid Mulga Lands in Eastern Australia', *Australian Journal of Ecology* **15**, 23–34.

Tongway, D. J., Valentin, C. & Seghieri, J. (2001), *Banded Vegetation Patterning in Arid and Semiarid Environments*, Springer.

Turchin, P. (2003), *Complex Population Dynamics: a Theoretical/Empirical Synthesis*, Princeton University Press, Princeton.

Turchin, P. & Hanski, I. (1997), 'An Empirically Based Model for Lattitudinal Gradient in Vole Population Dynamics', *Am. Nat.* **149**, 842–874.

Valentin, C., d'Herbès, J. M. & Poesen, J. (1999), 'Soil and Water Components of Banded Vegetation Patterns', *Catena* **37**, 1–24.

van Saarloos, W. (2003), 'Front Propagation into Unstable States', *Phys. Rep.* **386**, 29–222.

Volterra, V. (1926), 'Variazioni e Fluttuazioni del Numero d'Individui in Specie Animali Conviventi', *Mem. Acad. Lincei.* **2**, 31–113. (Translation in an Appendix to Chapman RN (1931) J. Anim. Ecol. 409-448).

Wang, R. H., Liu, Q. X., Sun, G. Q., Jin, Z. & van de Koppel, J. (2009), 'Nonlinear Dynamic and Pattern Bifurcations in a Model for Spatial Patterns in Young Mussel Beds', *J. R. Soc. Interface* **6**, 705–718.

Wheeler, P. & Barkley, D. (2006), 'Computation of Spiral Spectra', *SIAM J. Dyn. Syst.* **5**, 157–177.

White, L. P. (1969), 'Vegetation Arcs in Jordan', *J. Ecol.* **57**, 461–464.

White, L. P. (1970), 'Brousses Tigrees Patterns in Southern Niger', *J. Ecol.* **58**, 549–553.

Worledge, D., Knobloch, E., Tobias, S. & Proctor, M. (1997), 'Dynamo Waves in Semi-Infinite and Finite Domains', *Proc. R. Soc. Lond. A* **453**, 119–143.

Worrall, G. A. (1960), 'Tree Patterns in the Sudan', *J. Soil Sci.* **11**, 63–67.